III-2

Material Sciences

BL1U

Gamma-Ray Induced Positron Annihilation Lifetime Spectroscopy of Undoped and Bi-Doped SrTiO$_3$ Ceramics

K. Kamoshida[1], M. Kitaura[1], M. Hagiwara[2], H. Masai[3], S. Watanabe[4] and Y. Taira[5,6]
[1]*Facalty of Science, Yamagata University, Yamagata 990-8560, Japan*
[2]*Department of Applied Chemistry, Keio University, Yokohama 223-8522, Japan*
[3]*Department of Materials and Chemistry, National Institute of Advanced Industrial Science and Technology (AIST), Ikeda 563-8577, Japan*
[4]*Innovative Technology Laboratories, AGC Inc., Yokohama 230-0045, Japan*
[5]*UVSOR Synchrotron Facility, Institute for Molecular Science, National Institutes of Natural Science, Okazaki 444-8585, Japan*
[6]*School of Physical Science, The Graduate University for Advanced Studies (SOKENDAI), Okazaki 444-8585, Japan*

Relaxors are dielectrics with substantial energy storage capacity. It is expected that these materials will contribute to the miniaturization and efficiency of diverse electrical systems. However, well-known lead-free ceramics exhibit challenges, including the generation of heat during voltage application, which can markedly reduce the capacitor's lifespan. To address this challenge, the focus has shifted to relaxor dielectrics such as (Sr,Bi)TiO$_3$ (SBT), which are obtained by Bi doping into SrTiO$_3$ (STO). This material has garnered significant attention due to its potential as a solution to the aforementioned issues [1]. The valence of the Bi atom occupying the A site (Sr site) is not equivalent to that of the Sr atom, suggesting the introduction of atomic vacancies to compensate for the charge of the Bi atom at the A site. In this study, we employed gamma-ray induced positron annihilation lifetime spectroscopy (GiPALS) and first-principles calculations based on density functional theory (DFT) to investigate whether atomic vacancies are introduced by Bi doping in STO.

Samples of STO and SBT were ceramics synthesized by the solid state reaction. The experimental details of the GiPALS analysis have been previously reported [2]. To identify the origin of atomic vacancies in SBT, positron annihilation lifetimes were determined by DFT calculation using the ABINIT code [3]. The GiPALS spectra of STO and SBT ceramics are shown in Fig. 1. The data were measured at room temperature. The GiPALS spectra of STO and SBT are characterized by a predominant exponential decay component. The positron annihilation lifetimes of STO and SBT were determined to be 187 ± 1 ps and 291 ± 1 ps, respectively. It is evident that the lifetime of the ceramics undergoes a substantial alteration upon the introduction of Bi doping. This substantial alteration in the lifetime of the ceramics suggests the introduction of atomic vacancies as a consequence of the Bi doping process. The calculated positron annihilation lifetime for the unit cell of STO (bulk lifetime) was 157 ps. The calculated bulk lifetime for STO was nearly equivalent to the experimental bulk lifetime of the STO single crystal (146 ± 2 ps). This outcome serves to substantiate the validity of the experimental approach employed in this study. Furthermore, the calculated lifetimes for the 2×2×2 supercells of STO containing cation vacancies at the A and Ti (B) sites were 277 ps ($q=-2$) and 195 ps ($q=-4$), respectively. It is noteworthy that these values exhibited slight variations depending on the valence of the supercell (q). In the STO ceramics, positrons can annihilate at either of dislocations or Ti vacancies at the B sites. The experimental lifetime for the SBT ceramics exhibited agreement with the calculated lifetime for the 2×2×2 supercells of STO containing a Sr vacancy at the A site. In the SBT ceramics, positrons most likely annihilate at Sr vacancies at the A sites. The analysis of the effect of Na and K codoping on vacancies at the A site is currently underway. This work was supported in part by JSPS Grants-in-Aid for Transformative Research Areas (A) Hyper-Ordered Structures Sciences (Nos. 23H04094, 23H04119, 20H05882).

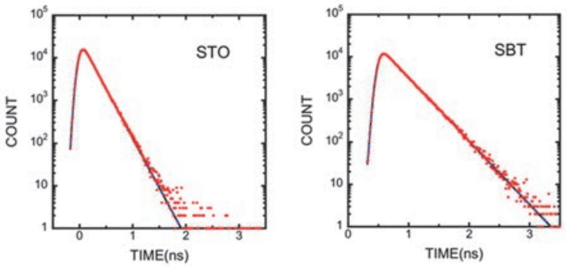

Fig. 1. GiPALS spectra of STO and SBT ceramics, measured at room temperature.

[1] D. Yuqin *et al*., Composites B **230** (2022) 109493.
[2] M. Kitaura *et al*., Opt. Mater.: X **14** (2022) 100156.
[3] X. Gonze *et al*., Comput. Phys. Commun. **248** (2020) 107042.

BL1U

Changes in Positron Annihilation Lifetimes for CeO_2 by Heat Treatment and Re-Adsorption of Oxygen

S. Dohshi[1], K. Maeda[1], Y. Taira[2] and T. Hirade[3]
[1]*Osaka Research Institute of Industrial Science and Technology*
2-7-1, Ayumino, Izumi, Osaka 594-1157, Japan
[2]*UVSOR Synchrotron Facility, Institute for Molecular Science, Okazaki 444-8585, Japan*
[3]*Japan Atomic Energy Agency, Ibaraki 319-1195, Japan*

In the previous study, the authors arranged a cerium oxide (CeO_2) catalyst within a quartz tube and performed gamma-ray induced positron annihilation lifetime spectroscopy (GiPALS) measurements at room temperature in air. The positron annihilation lifetimes of CeO_2 arranged within a quartz tube were nearly equivalent to those of CeO_2 measured without quartz tube. This result suggests that the positron annihilation lifetime measurements of CeO_2 can be performed, even though using quartz tube. Then, the GiPALS measurements were performed on CeO_2 that was arranged within a quartz tube and subjected to treat at 200 °C under argon (Ar) flow, resulting in changing the lifetime component attributed to the annihilation at CeO_2 surface. Additionally, the positron annihilation lifetime spectrum was observed to return to its original state when air containing water vapor was introduced, possibly due to the re-adsorption of oxygen and/or water molecules on the surface defect sites [1]. However, it was uncleared that which gas was re-adsorbed on the surface defect sites.

This study observed the changes in the positron annihilation lifetime spectra as the heating temperature was varied. Additionally, the changes in positron annihilation lifetime spectra were observed when only oxygen was re-adsorbed on CeO_2 treated at 200 °C under Ar flow.

The pellet sample with 20 mm in diameter and 10 mm in thickness were prepared using CeO_2 nanoparticles with a primary particle size of ca. 2 nm. In this experiment, the pellets were heated in a quartz tube at a rate of 10 °C/min using a jacket heater under Ar (purity: 99.999%) flow at pre-determined temperature (50 °C ~ 200 °C) and held for 2 h. After cooling under Ar flow, GiPALS measurements were performed. Finally, oxygen (purity: 99.999%) was flowed through at a rate of 200 mL/min for 1 h at room temperature, followed by another GiPALS measurement under oxygen flow.

We have set up a gamma-ray spectroscopy system at the laser-Compton scattering (LCS) beamline of BL1U at UVSOR-III [2], and measured the lifetime of the annihilation gamma-rays at room temperature using BaF_2 scintillation detector. We used the software Lifetime9 (LT9) to analyze the spectra.

The spectra were changed with the increase in the heating temperature. This is because the positron lifetime increases when heated under Ar flow. Adsorbed active oxygen species have been reported to desorb at temperatures above 150 °C. Consequently, the spectral change below 150 °C can be attributable to desorption of water molecules adsorbed on surface defect sites.

Figure 1 shows the positron annihilation lifetime spectra of CeO_2 at room temperature in air, treated at 200°C under Ar flow, and re-adsorbed oxygen. The positron annihilation lifetime becomes longer when CeO_2 was treated at 200 °C. This change was believed to result from the emergence of oxygen defects on the surface caused by the desorption of adsorption species such as active oxygen and water molecule, as above mentioned. Additionally, the positron annihilation lifetime spectrum was observed not to return to its original state when only oxygen was introduced. Considering the recovery of the spectrum to its original state upon the introduction of air containing water vapor, it can be assumed that there are multiple types of defect sites on CeO_2 surface. Details will be discussed in the future.

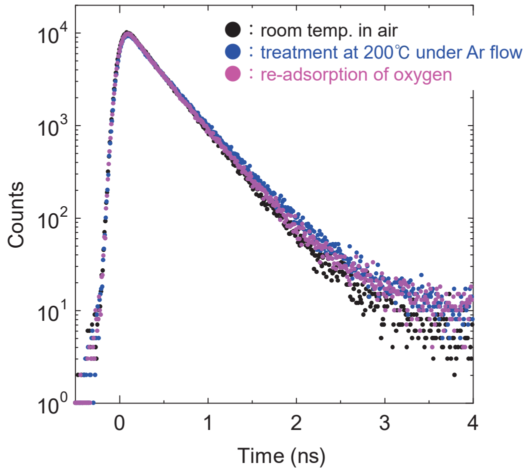

Fig. 1. Positron annihilation lifetime spectra of CeO_2 measured under different conditions.
(a) at room temperature in air, (b) after heating at 200 °C for 2h in Ar, (c) re-adsorption of oxygen.

[1] S. Dohshi *et al.*, UVSOR Activity Report **51** (2023) 63.
[2] Y. Taira *et al.*, Rev. Sci. Instrum. **84** (2013) 053305.

BL1U

Characterization of Defects in Ni Alloys Based on Gamma-ray-induced Positron Annihilation Spectroscopy

Z. Weixin[1,3], Y. Yuxuan[2,3], Y. Yigang[1] and Y. Taira[3]
[1]*Key Laboratory of Particle and Radiation Imaging (Ministry of Education) and Department of Engineering Physics, Tsinghua University, Beijing 100084, China*
[2]*School of Physics, Zhengzhou University, Science Avenue 100, Zhengzhou 450001, China*
[3]*UVSOR Synchrotron Facility, Institute for Molecular Science, Okazaki 444-8585, Japan*

Positron annihilation spectroscopy (PAS) serves as a powerful non-destructive probe for characterizing atomic-scale defects including vacancy and dislocation in bulk materials. In recent years, gamma-ray-induced positron annihilation spectroscopy (GiPAS) which can be used to study defects in crystals, metals, alloys, and polymers for thick samples (~cm) has developed rapidly [1]. This technology can be used to predict the fatigue and failure of the engineering materials by detecting the volumetric assay of defects at early stage.

The determination of the fatigue and failure level at the early stage before appearing obvious cracks of thick engineering materials is important to evaluate its service life. Inconel 718, a Ni-Fe-Cr austenite (γ) has attracted attention as its particular applications in a variety of applications like gas turbine blades, combustors. We systematically investigate defect evolution in industrial-grade Inconel 718 nickel-based superalloy subjected to incremental tensile deformation (0%, 0.2%, 1%, 2%, 5%, and 10%). GiPAS has been developed at UVSOR [2] and can be used to probe the detects of thick materials. The setup of positron annihilation lifetime spectroscopy (PALS) measurement is shown in Fig1.

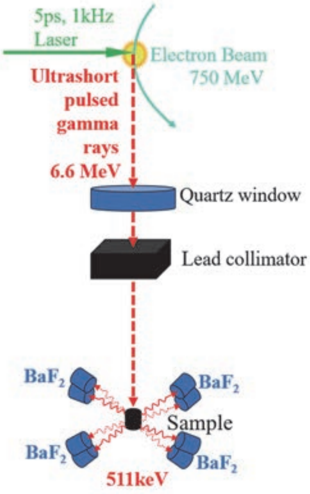

Fig. 1. Setup for PALS measurements.

We implemented PALS coupled with first-principles calculations based on density functional theory (DFT) to quantify defect characteristics. The experimental positron annihilation lifetimes (τ_1 and τ_2) and relative intensities (I_1 and I_2; I_1+ I_2=1) are analyzed using LT9 software. The results are shown in Fig2.

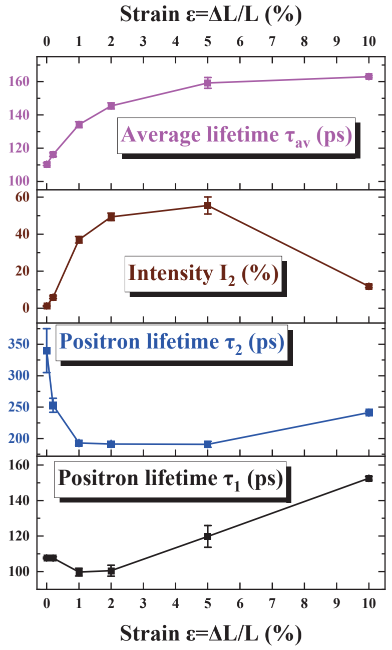

Fig. 2. Fitting results of the experimental positron lifetime spectra.

The calculated free-state positron lifetime of Ni alloy ($Ni_{19}Fe_6Cr_6Nb$) is approximately 106ps. As the positron lifetime τ_1 is larger than this value, it can be considered as a weighted sum of the free-state positron lifetime and the positron lifetime at the dislocation defects. The positron lifetime τ_2 has a range of 190-400ps, which corresponds to the positron lifetime at the vacancy-type defects according to the calculated results. The average positron lifetime tend to increase with increasing tensile strain and indicates that the densities of dislocation and vacancy defects in the sample increase with increasing tensile strain. When the tensile strain reached to 10%, the intensity I_2 has an obvious change which may mean that the defect structure in the sample has changed significantly.

[1] F. A. Selim *et al.*, Nucl. Instr. Meth. Phys. A **495** (2002) 154.
[2] Y. Taira *et al.*, Rev. Sci. Instrum. **84** (2013) 053305.

BL2A

Mo L_{III}-edge XANES Study of Formation of Catalytically Active Mo_2C Species on H-MFI Zeolites for Methane Aromatization

K. Kuramochi[1], Y. Mita[2], A. Kosuge[2] and H. Aritani[2]
[1]*Advanced Science Research Laboratory, Saitama Institute of Technology, Fukaya 369-0293, Japan*
[2]*Faculty of Engineering, Saitama Institute of Technology, Fukaya 369-0293, Japan*

Molybdenum-modified H-MFI zeolite (Mo/H-MFI) is a typical GTL (Gas To Liquid) catalyst for natural gas transformation. High catalytic activity over the Mo/H-MFI is shown for methane conversion to benzene although definite deactivation due to coke deposition has been a serious problem for durable MTB reactivity. It has been revealed that the reactions at high pressure (0.15 - 0.20 MPa) and the addition of H_2 to the CH_4 reactant were each effective in suppressing catalyst deactivation. On these reaction conditions, deactivation process over the catalysts is one of the important points. A cause of the deactivation is based on coke deposition on strong acid sites over H-MFI and structural deactivation on carbonized MoC_x species. Thus, clarification of Mo sites with high and durable activity for methane dehydrogenation is one of the most important subjects. In the present study, Mo L_{III}-edge XANES is applied to characterize the active Mo carbide species on Mo/H-MFI. In the present study, time course of the formation of active Mo_2C species on H-MFI has been investigated.

Mo(5wt%)/H-MFI (Si/Al_2 ratios in H-MFI supports are 23 and 50) catalysts were prepared by impregnation of H-MFI in $MoO_2(acac)_2$-$CHCl_3$ solution, and followed by drying overnight and calcination at 773 K. The methane aromatization reactivity was evaluated at 1023 K in a steady-state reaction by using CH_4(20%)-H_2(2%)-Ar(base) reactant as described in a previous report[1]. Mo L_{III}-edge XANES spectra were obtained in BL2A of UVSOR-IMS in a total-electron yield mode using InSb double-crystal monochromator. REX-2000 (Rigaku) software was used for normalization of each XANES spectra.

It has been summarized that the catalytic MTB activity over Mo/H-MFI with Si/Al_2=50 shows high activity at high pressure (0.15-0.20 MPa), and deactivation rate over reaction time is extremely small. In contract, Mo/H-MFI with Si/Al_2=23 exhibited high activity with significant deactivation over time[2]. For these catalysts, time course of the formation of Mo species during the reaction was investigated as follows. The L_{III}-edge XANES spectra over the Mo/H-MFI catalysts on time course of the MTB reaction in 0.15 MPa are shown in Fig. 1. In both catalysts before reaction, the spectra are almost similar to that of MoO_2, indicating the formation of Mo^{4+} by pre-reduction treatment with CO(2%)-Ar. For Mo/H-MFI in Si/Al_2=23, the XANES spectrum after the reaction for 30 minutes was very similar to that of α-type Mo carbide (α-MoC_{1-x}) with cubic structure, indicating that the Mo species were carbonized reductively at the early stage of the reaction. The XANES edge energy of the active Mo species shifted to the lower energy side with the progression of reaction time, suggesting that reduction by carbonization had further progressed. For Mo/H-MFI in Si/Al_2=50, the XANES spectrum after the reaction for 30 minutes was very similar to that of β-type Mo_2C with orthorhombic structure. It indicates the formation of easily reduced Mo sites to form more deeply carbonized species than that of Mo/H-MFI in Si/Al_2=23. Since the β-Mo_2C active species hardly changed with the progression of reaction time, it is suggested that they exist as stable carbide species. The result is likely to relate to a suppression effect of deactivation.

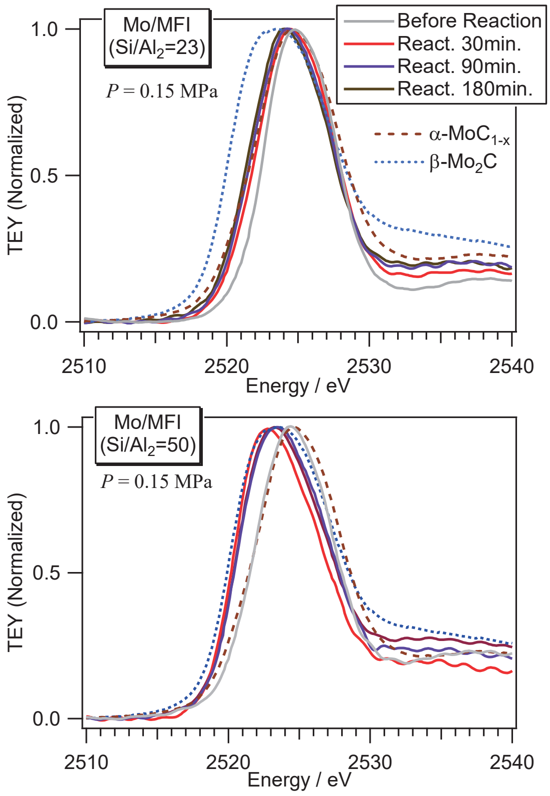

Fig. 1. Mo L_{III}-edge XANES spectra of Mo/H-MFI catalysts in Si/Al2=23 (top) and 50 (bottom) after the MTB reaction at 1023 K.

[1] H. Aritani *et al.*, J. Environm. Sci. **21** (2009) 736.
[2] K. Kuramochi *et al.*, UVSOR Activity Report **51** (2023) 69.

BL2A

Local Structure Investigation of Zn Dopant in Ga_2O_3

S. Yoshioka[1], K. Yasuda[1], C. Hsiao[2], C Hsu[2], W. Olovsson[2], J. Brick[2],
C. Hemmingsson[2] and G. Pozina[2]
[1]*Department of Applied Quantum Physics and Nuclear Engineering, Kyushu University,*
Fukuoka 819-0395, Japan
[2]*Department of Physics, Chemistry, and Biology, Linköping University, Linköping 58183, Sweden*

Gallium oxide (Ga_2O_3) is a promising ultrawide bandgap semiconductor for high-voltage and high-power applications. Monoclinic β-phase of Ga_2O_3, which has tetrahedral and octahedral gallium sites, is unintentionally *n*-type doped, and a good control of electron carrier concentrations in the range of 10^{16}–10^{19} cm^{-3} or even higher can be achieved using intentional doping by Si, Sn, Ge and Nb. However, the electrical conductivity of *p*-type in β-Ga_2O_3 is difficult to be realized. First-principles calculations showed that Zn can be a suitable acceptor forming two shallow levels at 0.05 eV and 0.07 eV above the valence band in β-Ga_2O_3 when Zn substitutes Ga in tetrahedral and octahedral coordination, respectively. We utilize halide vapor phase epitaxy growth to synthesize epitaxial layers of β-phase Ga_2O_3 doped with Zn, which can serve as a suitable acceptor. To determine the location of Zn ions within the β-Ga_2O_3 lattice, we employed X-ray absorption near edge structure (XANES) in conjunction with first principles density functional theory (DFT) calculations.

The Zn concentration of thin films, named as ZGO-L and ZGO-H, were 1.7×10^{19} and 2.5×10^{20} ions/cm^3, respectively. XANES measurements of the Zn L_3-edge and Ga L_3-edge were performed on the BL2A beamline of UVSOR Okazaki, Japan, using the partial fluorescence yield method (PFY). A $Be_3Al_2Si_6O_{18}$ (beryl) double-crystal monochromator gives the Zn L_3-edge and the Ga L_3-edge in the energy regions 1000 – 1070 eV and 1100 – 1170 eV, respectively. The samples were set with their surface perpendicular to the incident X-ray beam. Fluorescence X-rays of Zn L_α and Ga L_α were collected using an energy dispersible silicon drift detector (SDD).

The XRD pattern of the Zn doped samples appear to be similar to that of the undoped Ga_2O_3 samples. However, the information obtained from the XRD measurements was insufficient to conclude the exact position of the Zn atoms in the monoclinic Ga_2O_3 lattice. Moreover, it was also not clear whether Zn can build clusters or if it can include small numbers of ZnO or $ZnGa_2O_4$.

XANES spectra with the Zn L_3-edge (1020 eV) were shown in Fig. 1 for the Zn-doped Ga_2O_3 thin film sample and a reference ZnO powder sample. The intensity of each spectrum was normalized to a value of 1 at 1050 eV after the removal of the background intensity. The spectral signal-to-noise ratios of the thin films were slightly low because of the dilute concentration of zinc, however, fine structures such as peaks *A* to *G* were detected. In terms of such identical peaks, the spectrum shape of ZGO is clearly different from that of standard sample ZnO with a wurtzite type structure. The theoretical investigation using first principles calculation indicated that Zn ions occupied at cationic positions at the tetrahedral coordinated sites [1].

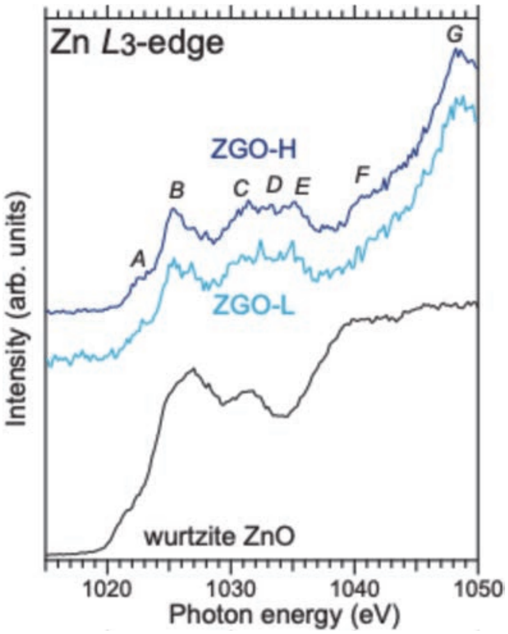

Fig. 1. Zn L_3-edge XANES spectra of the Zn-doped Ga_2O_3 thin films, together with the spectrum of wurtzite ZnO powder as a reference.

[1] S. Yoshioka *et al.*, J. Phys. Chem. C. **128** (2024) 18879.

BL2A

sXAS Study of the Fe-NiS OER Catalyst

Z. WANG[1], Y. ZHANG[1] and J. LEI[1]
[1]*City University of Hong Kong, Kowlong, Hong Kong*

Iron-doped nickel sulfide (Fe–NiS) catalysts are widely studied for the oxygen evolution reaction (OER) because adding Fe into NiS significantly enhances both activity and stability compared to pure NiS. Nickel sulfides possess high electrical conductivity and accessible redox chemistry but tend to reconstruct under anodic potentials: Ni^{2+} centers are oxidized to higher-valence states, and sulfide ligands transform into oxy- or sulfate species. Introducing Fe further adjusts the Ni–S electronic environment, accelerates redox kinetics, and helps suppress corrosion by promoting in situ formation of protective iron–oxygen clusters.

Soft X-ray absorption spectroscopy (sXAS) at the Ni L_3 and S K edges is particularly well suited to tracking these reconstruction events. At the Ni L_3 edge, 2p→3d transitions reveal changes in nickel oxidation state and local coordination—indicators of active Ni^{3+} (and Ni^{4+}) species forming under OER bias. At the S K edge, 1s→3p transitions distinguish sulfide (S^{2-}), intermediate oxy-sulfur species (e.g., sulfite), and final sulfate (SO_4^{2-}) states. Comparing spectra before and after OER clearly shows how the Ni–S framework evolves: the sulfide network converts into an oxyhydroxide-like shell enriched in Ni^{3+}/Ni^{4+} and surface sulfates, which directly influence catalytic kinetics and durability.

Understanding these electronic and chemical transformations is crucial for rational catalyst design. Ni^{3+} species on the surface are recognized as the true active sites for OER, while conversion of sulfur ligands to sulfate creates a passivating layer that repels corrosive ions (e.g., Cl^- in seawater), thereby improving long-term performance. Operando sXAS thus provides a microscopic picture of how Fe–NiS catalysts dynamically self-organize into their most active and stable configurations during water oxidation. These linsights guide strategies such as optimizing Fe/Ni ratios, controlling sulfide crystallinity, and adjusting electrolyte composition to develop highly efficient and durable OER catalyst

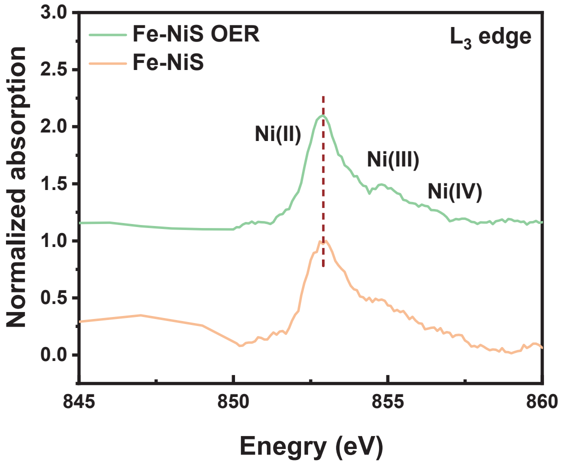

Fig. 1. Ni L-edge sXAS of Fe-NiS catalyst.

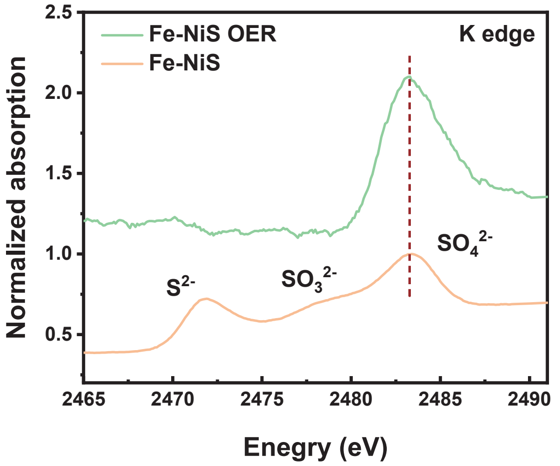

Fig. 2. S K-edge sXAS of Fe-NiS catalyst.

[1] Q. Dai *et al*., Nano Res. **17** (2024) 6820.
[2] X. Luo *et al*., Nat. Commun. **15** (2024) 8293.
[3] F. Jalilehvand, Chem. Soc. Rev. **35** (2006) 1256.

BL3U

Surface Effect on the Layer Structure in the Chiral SmC Variant Phase Delicate Balance of Ferroelectricity and Antiferroelectricity by Resonant Soft X-ray Scattering (RSoXS) at UVSOR

Y. Takanishi[1], F. Araoka[2] and H. Iwayama[3]
[1]*Department of Physics, Kyoto Prefectural University of Medicine,1-5, Shimogamohangi-cho,*
Sakyo, Kyoto 606-0823, Japan
[2]*RIKEN Center for Emergent Matter Science, Hirosawa 2-1, Wako, Saitama 351-0198, Japan*
[3]*UVSOR Synchrotron Facility, Institute for Molecular Science, Okazaki 444-8585, Japan*

The ferroelectricity and antiferroelectricity have been found in the tilted chiral smectic phases, called SmC* and SmC$_A$*, respectively. By competition of SmC* and SmC$_A$*, several phases with narrow temperature range were often found, called subphases. Subphases have are defined as the relative ratio of anticlinic and synclinic ordering, q_T. The structures of subphases becomes decisive using resonant X-ray scattering (RXS), and one of authors (YT) discovered new subphases with 6-, 7-, 8- and 10-layer periodicities[1,2].

In a certain chiral binary system, it was found that clear phase transition between subphases seems not to be seen[2]. The composed compounds do not have a specific atom, so that resonant soft x-ray scattering (RSoXS) has been applied to this study, and we directly observed the structure of continuous change between SmC* and SmC$_A$* using wide angle RSoXS.

The experiment was performed at BL3U of UVSOR. Used sample is a mixture of MC881 and MC452, as shown in Fig. 1. Figure 1(c) shows the phase diagram around the critical mixing ratios. In this study, two types of sample cells were prepared; a planar sub-micron thick sandwich cell whose substrates are 100 nm-thick Si_3N_4 membranes, and the liquid-crystal-filled grid mesh for electron transmission microscopy. The scattering was detected by CCD (ANDOR DO940P-BN). Incident X-ray beam was tuned between 270~300 eV, and carbon K-edge energy was 284.5 eV in the mixture.

RSoXS intensity profiles of the mixture of 55.7wt% MC452 at 24°C in the sandwich cell and the mesh are shown in Figs. 2(a) and (b), respectively. In Fig.2(a), a strong sharp peak was observed at Q ~ 1.1 nm^{-1} suggesting to the bilayer structure, while a splitted strong peak at Q ~ 0.55 nm^{-1} corresponding to the 4-layer periodicity was observed in Fig. 2 (b). (Peak splitting is caused by the helical structure.) This difference is considered to be caused by the surface effect. The gap of membrane sandwich cell was very thin. Hence the strong surface effect appears and molecular orientation is limited to the substrate surface plane. On the other hand, in the mesh cell, the surface effect is weak. As a result, the molecular orientation has the degree of freedom in the azimuthal angle as a bulk state. The difference in structure between these two cells is believed to be due to the surface effects mentioned above, and the small energy difference between the ferroelectric and antiferroelectric orders.

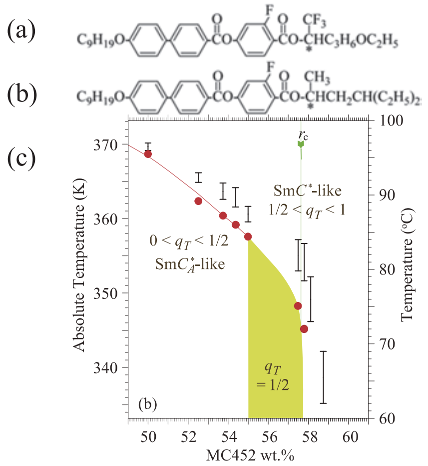

Fig. 1. Chemical structures of (a)MC452 and (b) MC881, and (c)the phase diagram referred from [3].

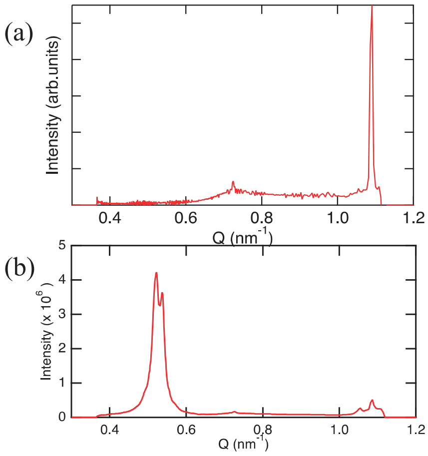

Fig. 2. RSoXS intensity profiles of the sandwich cell (a) and the grid mesh (b) of the mixture of 55.7wt% MC452 at 24°C.

[1] Y. Takanishi *et al.*, Phys. Rev. E **87** (2013) 050503 (R).
[2] Z. Feng *et al.*, Phys. Rev. E **96** (2017) 012701.
[3] Z. Feng *et al.*, Phys. Rev. E **102** (2020) 012703.

BL3B

Non-Proportional Response between Scintillation Light Yield and Energy of the Incident Gamma Rays

S. Kurosawa[1,2,3], Y. Urano[2,4], C. Fujiwara[2,4] and A. Yamaji[1,2]
[1]*New Industry Creation Hatchery Center (NICHe), Tohoku University, Sendai 980-8579, Japan*
[2]*Institute for Materials Research (IMR), Tohoku University, Sendai 984-8577, Japan*
[3]*Institute of Laser Engineering, The University of Osaka, Suita, Osaka 565-0871, Japan*
[4]*Graduate School of Engineering, Tohoku University, Sendai 980-0845, Japan*

Boron neutron capture therapy (BNCT) is one of the treatments to selectively destroy cancer cells using a nuclear reaction between ^{10}B and neutrons. Although evaluation of the treatment effect in real-time is required for patient safety, the monitoring system has not been realized. The use of prompt gamma rays (478 keV) emitted by the ^{10}B(n,α)^{7}Li reaction during BNCT therapy has been proposed as this monitoring system[1], and the 478-keV gamma-ray signal should be discriminated from the background (BG) events including 511-keV gamma rays from positron and electron annihilation. Thus, scintillators are required to have an energy resolution better than 4 % (FWHM) at 511 keV.

Tl-doped $Cs_3Cu_2I_5$ (Tl:CCI) scintillator has a high light output of over 90,000 photons/MeV and a high energy resolution of 3.3% at 662 keV (FWHM), which corresponds to 3.7% at 511 keV (FWHM) [2]. Moreover, the hygroscopic nature of this material is ignorable, as even typical iodide crystals have. Thus, this material is expected to be suitable for gamma-ray detection of the BNCT clearly, if the energy resolution is improved.

Here, energy resolution is related to light yield and non-proportionality between scintillation light yield and energy of the incident gamma rays. Tl:CCI has a non-proportional response (NPR) of over 3%, where NPR is defined in [3]. Recently, NPR and energy resolution for Sr^{2+}-co-doping Tl^{+}-doped NaI have been reported to be improved [3]. Therefore, we grew Tl^{+} and Sr^{2+} co-doped CCI (Tl,Sr:CCI) crystals and evaluated their luminescence and scintillation properties.

Tl,Sr:CCI, Sr:CCI, Tl:CCI and pure CCI crystals were grown by the vertical Bridgman-Stockburger method in our laboratory, and we verified the single crystal phase and composition using several X-ray devices. Also, we have measured several optical properties such as emission and excitation wavelength, light output and NPR. The results showed Sr-dopant effect was also observed for Tl,Sr:CCI; NPR and energy resolution were improved compared to Tl:CCI

In UVSOR, we investigated several properties, especially the role of the Sr. The temperature dependence of photoluminescence excitation and emission spectra from 10 to 350 K were evaluated at UVSOR BL3B beam line.

Here, we measured excitation and emission two-dimensinal map at each temperature, and over 150K the emission and excitation wavelengths were slightly shifted for the both samples. This result suggested CCI has different emission mechanisms in the lower and higher temperature regions.

Figure 1 shows the temperature dependence of emission intensities for pure CCI and Sr:CCI, and the both data were fitted by the Arrhenius equation blow 150 K. The fitting results showed the activation energy was shifted by Sr-co-doping. This result suggested Sr^{2+} or indirect effect by the Sr^{2+} co-doping affects some trap site which is related to the non-proportionality and energy resolution.

We also measured the thermoluminescence grow curve in the BL3B beam line for the Sr-doped and Sr-free CCI. Although the results are preliminary ones, the differences are not observed clearly. These results indicated the de-excited electrons from such trap sites to ground state are relaxed by non-radiative process, or these trap sites can be located at deep level, which means de-trapping energy is expected to be over room temperature.

To analyze the details, we grew different concentration of Sr to doped with Tl:CCI and also Ca-co-dopant effect is investigated.

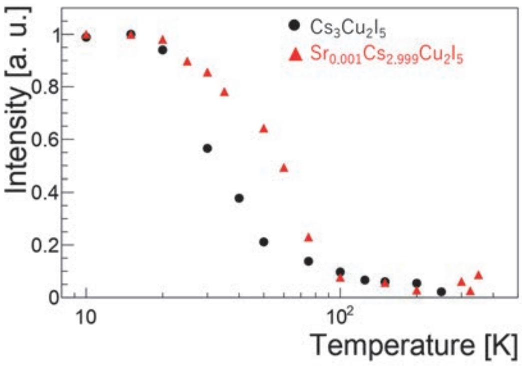

Fig. 1. Emission intensity as a function of temperature, where the intensities are normalized to 1 at 10 K.

[1] D.M. Minsky *et al.*, Appl. Radiat. Isot. **67** (2009) 179.

[2] L. Stand *et al.*, Instrum. Methods Phys. Res. A **991** (2021)164963.

[3] K. Yang *et al.,* J. Appl. Phys. **118** (2015) 213106.

BL3B

VUV Excitation Property of NIR Phosphor Eu:$CaSc_2O_4$

S. Kodama[1], T. Saito[1], I. Yanase[1] and H. Takeda[1]
[1]*Graduate school of Science and Engineering, Saitama University,*
255 Shimo-Okubo, Sakura-ku, Saitama 339-8570, Japan

Red or NIR emitting phosphors are widely used in white light-emitting diodes (LEDs) and as sensor materials such as scintillators or dosimeters. Most of the red or NIR phosphor was activated by the transition metals (particularly Cr^{3+} or Mn^{2+}) or rare earth metals exhibiting 4f-4f electron transition emission (particularly Pr^{3+}, Nd^{3+} or Yb^{3+}). Conventional red or NIR luminescence centers have several limitations, for instance, the luminescence decay is slow, and the range of excitation wavelength is narrow.

Recently, some phosphors activated by Eu^{2+} were reported to exhibited fast red or NIR emission. For example, the emission wavelengths of Eu:CaO and Eu:$Ca_3Sc_2Si_3O_{12}$ were 650 nm and 850 nm, respectively, with the faster luminescence decay than 1 μs [1,2]. Eu^{2+}-doped calcium-based materials are getting a attention as next-generational fast red or NIR phosphors. In this report, the VUV excitation property of noble NIR phosphor Eu:$CaSc_2O_4$ was investigated for the first time.

Eu:$CaSc_2O_4$ was synthesized via the high-temperature solid phase reaction from $CaCO_3$ (99.99%), Sc_2O_3 (99.99%) and Eu_2O_3 (99.99%). The starting powders are mixed in an agate mortar. The mixed powders were calcined at 1500 °C for 5 h in air. After calculating, the powders were annealed in a reducing atmosphere (N_2+H_2 gas) at 1000 °C for 5 h, and Eu^{2+}:$CaSc_2O_4$ was finally obtained [3].

The VUV-VIS-NIR photoluminescence excitation and emission spectra were measured in BL3B. The measurement temperature was 300 K. In order to cut the Eu^{3+} emission, the short-wavelength-filter (700 nm) was used in the measurement.

The photoluminescence excitation and emission spectra of Eu:$CaSc_2O_4$ is depicted in Fig. 1. The sample was excited using monochromatic photons ranging from 100 to 700 nm, and the photoluminescence emission spectra were recorded within the 550–1050 nm range. This measurement identified the Eu^{2+} emission wavelength of Eu:$CaSc_2O_4$ as 750 nm, situated in the red-NIR region. N_2+H_2 annealing at 1000 °C for 5 h should be insufficient to reduce Eu^{3+} completely into Eu^{2+}, and the Eu^{3+} 4f-4f emission was strongly observed in the same time.

The photoluminescence excitation spectra of Eu:$CaSc_2O_4$ were notably broad, spanning from 120 to 700 nm, indicating that Eu:$CaSc_2O_4$ can be excited by the entire range of VUV and visible photons. For practical applications, the excitation source for Eu:$CaSc_2O_4$ should be compatible with UV LEDs, blue LEDs, or green laser diode systems (LDSs).

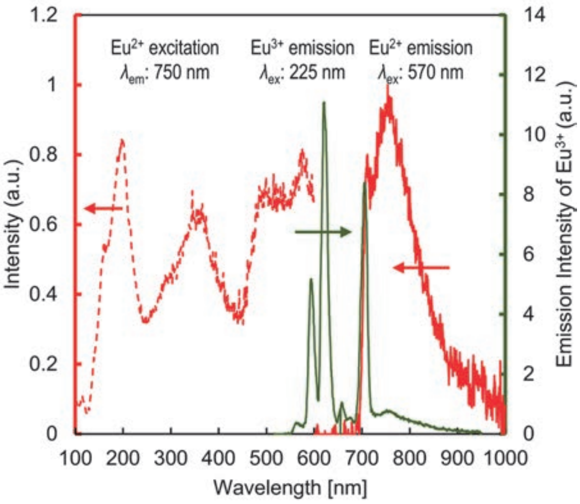

Fig. 1. Photoluminescence excitation and emission spectra of Eu:$CaSc_2O_4$.

[1] Q. Zhao *et al.*, J. Lumin. **253** (2023) 119457.
[2] I. V. Berezovskaya *et al.*, Chem. Phys. Lett. **585** (2013) 11.
[3] S. Kodama *et al.*, J. Soc. Inorg. Mater. Jpn *accepted.*

BL3B

Energy Transfer from I$^-$ Centers to Ce^{3+} Centers in Co-Doped NaCl: I$^-$, Ce^{3+} Crystals

R. Oda[1] and T. Kawai[1]

[1]*Graduate School of Science, Osaka Metropolitan University, Sakai 599-8531, Japan*

Alkali halide crystals have the wide band-gap up to the vacuum ultraviolet energy region and are a suitable candidate host for doping of impurity ions. We have studied energy transfer between two kinds of impurity ions doped in alkali halide crystals from the measurements of their optical properties [1-3]. In this study, we focused on Ce^{3+} ions as acceptor ions and investigated the energy transfer from I$^-$ Centers to Ce^{3+} Centers in co-doped NaCl:I$^-$, Ce^{3+} crystals.

The Ce^{3+} ions in crystals exhibit the luminescence due to the radiative transition from the lowest 5d excited level to the split 4f ground levels. The 5d -> 4f radiative transition in the Ce^{3+} ions is a dipole-allowed one with a typical decay time of about 20 ns [4]. The fast decay profiles allow us to measure a rise time due to energy transfer to the acceptor ions under single-bunch operation of UVSOR.

Figure 1 shows the luminescence and absorption spectra of co-doped NaCl:I$^-$, Ce^{3+} crystals at 10 K. The intense absorption and luminescence bands due to the I$^-$ centers are observed at 6.9 eV and 5.7 eV, respectively. The luminescence band at 5.7 eV comes from one-center-type relaxed excitons, which consist of a hole localized on an iodine anion and a bound electron, that is to say, special type of bound excitons [5]. Two luminescence peaks due to the Ce^{3+} centers were observed at 3.37 eV and 3.64 eV.

Figure 2 shows decay profiles of the Ce^{3+} luminescence under the excitation on the I$^-$ absorption band at various temperatures. Below 100 K, the Ce^{3+} luminescence exhibits the double exponential decay profiles, which have no rise time. Above 200 K, on the other hand, a rise time of a few tens of nanoseconds was observed in the decay profile of the Ce^{3+} luminescence. The rise time decreases with increasing temperature. It is difficult to believe that the slow rise time of a few tens of nanoseconds is attribute to energy transfer by the Förster-Dexter mechanism or the luminescence-reabsorption mechanism. In our previous paper [2], we have proposed the energy transfer processes through the migration of the V_K center generated from the excited I$^-$ centers in NaCl crystals. The idea is supported by the slow rise time of a few tens of nanoseconds in the decay profile of the Ce^{3+} luminescence. The temperature dependence of the rise time indicates that the migration of the V_K center occurs by thermally activated hopping.

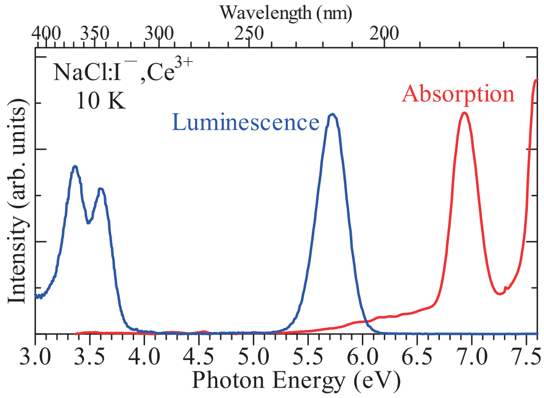

Fig. 1. Luminescence (blue) and absorption (red) spectra in co-doped NaCl:I$^-$, Ce^{3+} single crystals.

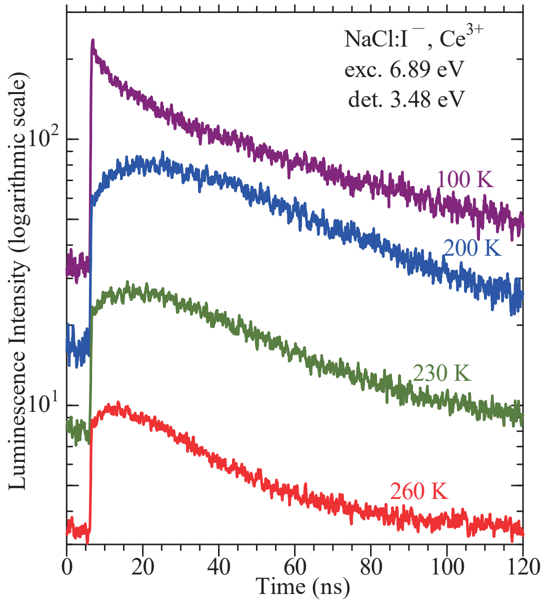

Fig. 2. Decay profiles of the Ce^{3+} luminescence under the excitation on the I$^-$ absorption band at various temperatures.

[1] A. Iguchi, T. Kawai and K. Mizoguchi, Phys. Status Solidi C **13** (2015) 85.

[2] O. Yagi, T. Kawai and K. Mizoguchi, J. Lumin. **226** (2020) 117359.

[3] R. Oda and T. Kawai, UVSOR Activity Report **51** (2024) 80.

[4] Y. Yokota *et al.*, Radiat. Meas. **45** (2010) 472.

[5] I. Akimoto, M. Shimozato and K. Kan'no, Phys. Status Solidi C **6** (2009) 342.

BL3B

Investigation of Charge Transfer Energies in Eu^{3+}-Doped Layered Mixed-Anion Phosphor by VUV Spectroscopy

H. Miyata[1] and J. Ueda[1]
[1]*Japan Advanced Institute of Science and Technology, Nomi 923-1292, Japan*

Persistent phosphors are luminescent materials that emit light for a long duration after the excitation source is turned off. They are widely used in many applications such as luminous paints in the dark for hazard signboards and road markers and luminescent markers for in vivo imaging. Persistent luminescence originates from the temporary trapping of the electrons or holes, generated with light absorption, by crystalline defects. The trapped electrons or holes are thermally released and transferred back to the luminescent center.

So far, aluminate and silicate compounds such as $SrAl_2O_4$:Eu^{2+}-Dy^{3+} [1] and $Sr_2MgSi_2O_7$:Eu^{2+}-Dy^{3+} have been widely used as practical persistent phosphors. In contrast, oxides including other oxoanion (CO_3^{2-}, NO_3^- and etc.) and non-oxides are still an unexplored material group for persistent phosphors and have the potential to show excellent persistent luminescent properties. Existing persistent phosphors have mostly shown blue and green luminescence. Therefore, there is a need to develop high-performance red persistent phosphors. Eu^{3+} is a promising candidate as a red emitting central ion. In addition, long afterglow properties have been reported for Eu^{3+}-doped phosphors in Y_2O_2S:Eu^{3+}-Ti-Mg.

In Eu^{3+}-doped persistent phosphors, the (de)trapping carriers are holes. Thus, the holes migrate in the valence band (VB) after charge transfer excitation and are trapped by crystalline defects and metal ions.[2] Therefore, understanding charge transfer (CT) behavior in Eu^{3+}-doped phosphors is essential for the development of persistent phosphors. In this study, we focus on Eu^{3+}-doped $La_2O_2CO_3$ reported by Masui and Imanaka [3]. Here, we prepared another polymorph of Eu^{3+}-doped $La_2O_2CO_3$ and discussed its charge transfer behavior from VUV PLE spectra.

Photoluminescence excitation (PLE) spectra of Eu^{3+} doped $La_2O_2CO_3$ at 10 K are shown in Fig. 1. PLE spectra were measured with monitoring Eu^{3+} $^5D_0$–$^7F_0$ emission. In the PLE spectra, two broad PLE bands are observed around 175 nm and 192 nm. The PLE band at 192 nm is attributed to the CT band of Eu^{3+}, and the PLE peak at 175 nm is attributed to the host-exciton formation. The E_g is calculated to be 6.98 eV using the obtained E_{ex} (192 nm). The CT bands were well-fitted by two Gaussian functions. Since $La_2O_2CO_3$ is a mixed anion compound, charge transfers derived from the two anions O^{2-} and CO_3^{2-} are possible. The CT energy (E_{CT}) of single anion compounds La_2O_3:Eu were reported to be 4.27 eV [4], and $Eu_2(CO_3)_3$ was estimated to be 5.30 eV from the PLE spectrum. Based on the obtained E_{CT}, a stacked vacuum referred binding energy (VRBE) diagram are prepared as shown in Fig. 2. According to the VRBE diagram, the low-energy CT band is attributed to O^{2-} and the high-energy CT band to CO_3^{2-}. By mixing with carbonate anion, the oxide can lower the valence band energy. Based on the valence band engineering by oxoanion doping, the hole-detrapping persistent phosphors will be developed in the future.

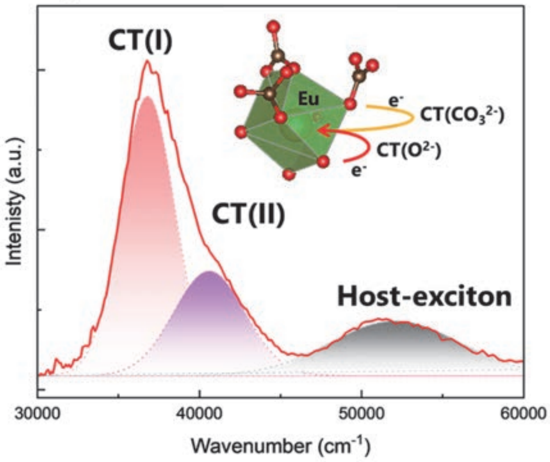

Fig. 1. PLE spectra of $La_2O_2CO_3$:Eu and crystal structure of $La_2O_2CO_3$ around La site.

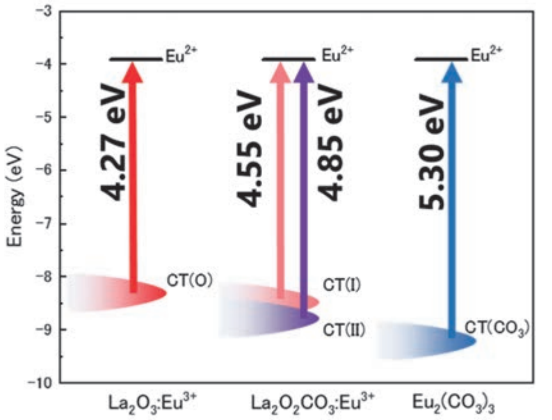

Fig. 2. Energy diagram of $Eu3^+$ charge transfer state and valence band top of La_2O_3, $La_2O_2CO_3$, $Eu_2(CO_3)_2$.

[1] T. Matsuzawa *et al.*, J. Electrochem. Soc. **143** (1996) 2670.
[2] J. Ueda, Bull. Chem. Soc. Japan **94** 2 (2021) 2807.
[3] K. Koyabu, N. Imanaka, *et al.*, J. Alloys Compd. **408–412** (2006) 867.
[4] Linkang Yu *et al.*, J. Lumin. **229** (2021) 117663.

BL3B

Effect of Ag-Doped Phosphate Glass for Radiophotoluminescence Dosimeter

J.Y. Cho[1], E.J. Choi[1], D.W. Jeong[1], N.D. Ton[1] and H.J. Kim[1]
[1]*Department of Physics, Kyungpook National University, Daegu 41566, Republic of Korea*

The release of large quantities of radioactive material during nuclear disasters such as Fukushima and Chernobyl has highlighted the critical importance of accurate radiation dosimetry. Reliable dose measurement is essential for ensuring radiation safety, assessing long-term health risks, and implementing appropriate protective measures. Traditional dosimeters such as Metal-Oxide-Semiconductor Field-Effect Transistor (MOSFET) dosimeters and thermoluminescence dosimeters (TLDs) are widely used due to their sensitivity and reusability. However, TLDs suffer from significant drawbacks, including high-temperature readouts, signal fading over time, and limited reproducibility. These limitations emphasize the need for alternative dosimetry technologies with improved performance and reliability. Radiophotoluminescence (RPL) glass dosimeters have emerged as a promising solution, offering excellent signal stability, dose linearity, and long-term reproducibility. In particular, the commercial GD-450 dosimeter, based on silver-doped phosphate glass, has demonstrated robust performance in both personal and environmental radiation monitoring.

Building on the strengths of existing RPL technologies, this study focuses on the development of enhanced RPL glass dosimeters through compositional engineering. Specifically, silver-doped phosphate glasses were synthesized using a variety of glass-modifying oxides to tailor their structural and luminescent properties. Glass modifiers play a crucial role in adjusting physical and optical characteristics by introducing non-bridging oxygens that alter the glass network. Drawing from previous research, including studies by Miyamoto *et al*. and Yoshida *et al*. [1, 2], which clarified the emission mechanisms and improved the thermal stability of silver-doped glasses, we aimed to further optimize RPL performance. By comparing the newly developed glasses with the commercial GD-450, this study investigates improvements in sensitivity and dose linearity, with the ultimate goal of advancing RPL dosimetry technologies for broader and more demanding applications.

The PLAN glasses were fabricated two way using conventional melting quenching method at atmospheric environment and induction melting quenching method at nitrogen enviroment in following composition: ($75.6P_2O_5$-$18.2Li_2$-$2.6Al_2O_3$-$2.6NaBr$-$1.0Ag_3PO_4$, PLAN). Fabricated glasses evaluated their photoluminescence (PL) at room temperature using BL3B beam line.

Fig. 1. PLAN:Ag glasses.

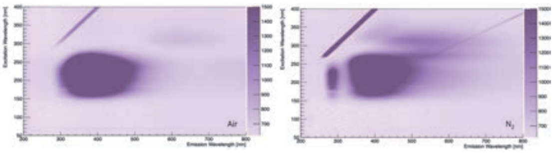

Fig. 2. The excitation and emission 2D scanning spectra.

Figure 1 shows fabricated glasses, and photoluminescence excitation and emission (2D scanning) spectra for these samples were displayed in Fig. 2. In the emission spectra, the emission around excitation wavelength between 150-275 nm is host emission of PLAN glasses and 300-350 nm is RPL emission. However, the RPL emission from nitrogen environment fabricated glasses slightly blue shift is observed. Also, emission from 275-300 nm is observed only nitrogen fabricated glasses.

This results indicated environment during fabrication is important to enhanced its luminescence and transparency.

[1] M. Yoshida *et al*., Radiat. Meas. **45** (2010) 890.
[2] Y. Miyamoto *et al*., Radiat. Meas. **45** (2010) 546.

BL4U

Correlation Between Electronic Structures and Supercapacitive Performance of NiCo/Pencil Lead Studied by X-ray Spectro-Microscopy

C. J. Yang[1,2], T. C. Huang[3], H. W. Chang[3], T. Araki[4], T. Ohigashi[4,5],
D. H. Wei[2] and C. L. Dong[1]
[1]*Department of Physics, Tamkang University, Tamsui 25137, Taiwan*
[2]*Graduate Institute of Manufacturing Technology, National Taipei University of Technology, Taipei 10608, Taiwan*
[3]*Department of Chemical Engineering, National United University, Miaoli 360302, Taiwan*
[4]*UVSOR Synchrotron Facility, Institute for Molecular Science, Okazaki 444-8585, Japan*
[5]*Photon Factory, High Energy Accelerator Research Organization, Tukuba 305-0801, Japan*

As the issue of energy shortage becomes increasingly serious, electrochemical energy storage is emerging as a highly active research area. Compared with other energy storage devices, supercapacitors have higher charge and discharge cycle life and better stability, while also enabling rapid charging and discharging reactions. The electrodes made of nanostructured nickel-cobalt oxides are not only facile to synthesize, but also offer the advantages such as low cost, high specific capacitances, low resistance, and environmental friendliness [1]. Carbon materials are also widely used as electrode materials due to their porous structure and high specific surface area, which could facilitate the electrothermal reactions and help improve overall performance [2]. In this study, NiCo-oxide nanostructures were prepared on pencil lead. The pencil lead was first activated using HNO_3 to form the activated pencil graphite electrode (APGE), and then treated hydrothermally with varying ratios of $Ni(NO_3)_2 \cdot 6H_2O$ and $Co(NO_3)_2 \cdot 6H_2O$ underwent hydrothermal treatment to obtain the nickel-cobalt oxides with different electrochemical activities.

The Scanning Transmission X-ray Microscopy (STXM) was used to investigate the electronic structure at the interface of different regions in the samples, which were prepared at different charge and discharge states based on Cyclic Voltammetry (CV). Among the samples with varying weight ratios, 1.6NiCo-20cy showed better electrochemical properties and charge storage capacity than the others. Therefore, this sample was subjected for *ex-situ* STXM to gain a deeper understanding of the electrochemical reaction mechanism.

Figure 1 displays the optical density images and corresponding stack-mapped STXM images for the O K-edge for the as-prepared 1.6NiCo-20cy sample (Fig. 1(a)), as well as those following full charging (Fig. 1(b)) and full discharging (Fig. 1(c)). Notably, two predominant regions, A and B, bisected at 535 eV are observed. In the region A, at around 532.8 eV is attributed to π^* transitions, which are strongly associated with the chemical environment of the oxygen bonds, and resulted from C=O and/or O-C–O π^* transitions. The region B mainly correspond to the σ^* transitions, attributed to a mixed O-H, C-O, or C=O states. A significant variation in the π^* state is clearly observed, indicating its critical role in charge storage performance.

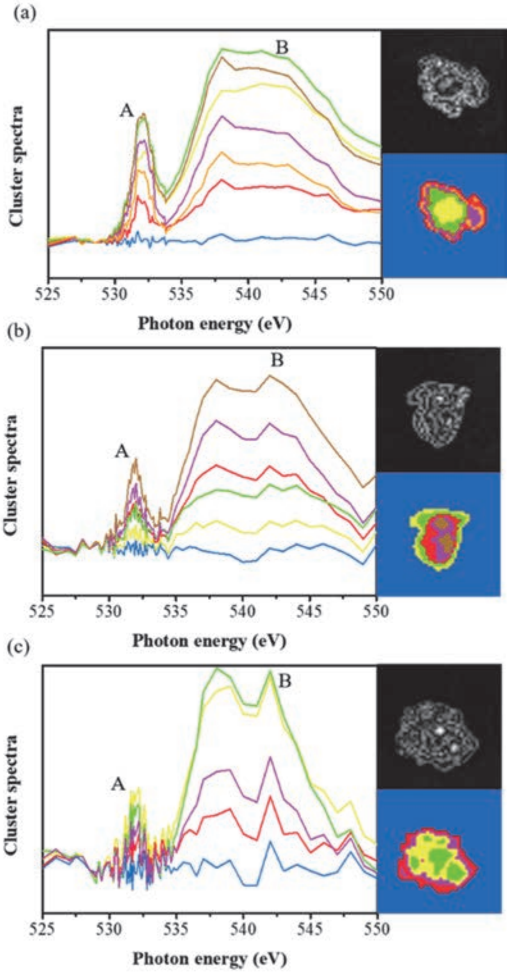

Fig. 1. Optical density images, stack-mapped STXM images, and the corresponding O K-edge XAS of (a) 1.6NiCo-20cy-Pristine, (b) fully charged-1.6NiCo-20cy and (c) fully discharged-1.6NiCo-20cy, focused at different sites of interest.

[1] T. Wang *et al.*, Nat. Commun. **14** (2023) 4607.
[2] M. Kuang *et al.*, Adv. Funct. Mater. **28** (2018) 1804886.

BL4U

Operando Nano-Scaled Identification to Carbon Dioxide and Water Gas Adsorption Coupling to Fe_3O_4 and Reduced Graphene Oxide

J. S. D. Rodriguez[1,2], H. Z. Lu[1], H. Yuzawa[3],
T. Araki[3] and C. H. Chuang[1]
[1]*Department of Physics, Tamkang University, Tamsui, New Taipei City 251301, Taiwan*
[2]*Institute of Chemistry, Leiden University, Leiden 2300 RA, The Netherlands*
[3]*Institute for Molecular Science, Okazaki 444-8585, Japan*

Graphene oxide (GO)-based membranes have shown excellent CO_2 gas separation performance due to the enlargement of the interlayer distance and chemical reactivity that provide a wiggle room on physical selectivity and chemical reactivity. On the other hand, Fe_3O_4 nanoparticles (NPs), aside from their apparent high surface area innate to their structure, have good reactivity towards CO_2 chemisorption due to their electron-donating nature. Hence, intercalating Fe_3O_4 NPs into GO membranes provides not only a straightforward combination but also a strategic method to enhance several factors: modulation of interlayer distance, increase in chemical reactivity to CO_2, and improvement of mechanical and thermal stability.

Our study aims to investigate the synergistic effects of Fe_3O_4 NP with GO in a membrane configuration, in particular the chemical change near the oxygen functional groups, via chemical mapping by scanning transmission X-ray microscopy (STXM) at C K-edge, O K-edge, and Fe L-edges. To identify the regions of interest, we select the high density/low density/absence of Fe_3O_4 NPs using the STXM obtained at the Fe 707.6 eV image, by the Fe-dependent optical density (OD) contrast. In Fig. 1 (d)-(g), the area selections in four samples marked by broken lines with labels "1", "2", and "3", correspond to areas with high density, low density, and absence of Fe_3O_4 NPs, respectively. In this report, we will limit the discussion to the assessment of the high-density areas only, where the interaction between the Fe_3O_4 NPs and GO flakes is assumed to be at the greatest extent in four samples.

The oxygen functional groups (C-OH at 286.5 eV and C=O of COOH at 288.5 eV) are commonly found in DC GO-Fe_3O_4 with/without CO_2 in Fig. 1(c), assigned based on our previous pure DC GO[1]. Regarding F_3O_4 NP contribution, the high increases of C=O of COOH/C-OH at 289.7 eV and C-O of COOH/O-C(O)-O state at 290.1 eV are notable in Fig. 1(c) and our paper before[1]. The electrochemically-reduced GO (EC-rGO), when evaluated without CO_2, reveals a typical C=C bond at 285.2 eV and hexagonal C-C bond at 292.6 eV. Additionally, there has an emergence of C-OH bond at 286. 2 eV and C=O of COOH. However, the C-O-C bond at 287.4 eV is absent specifically in EC rGO[1] due to the involvement of additional Fe_3O_4 NPs. Adding CO_2 purging into the mixing solution, the apparent increases in C-OH, C-O-C, COOH, and O-C(O)-O state are observed in EC rGO-Fe_3O_4, hinting at strong oxidation between the GO flakes and the purged CO_2/further HCO_3 gases dissolved in the solution.

No significant change is observed between DC GO-Fe_3O_4 with and without CO_2, confirming that only Fe_3O_4 NPs has no function for carbon capture and storage. A notable CO_2 storage is achieved in EC GO-Fe_3O_4 w/ CO_2 compared to that w/o CO_2, in terms of EC-involved enhancement.

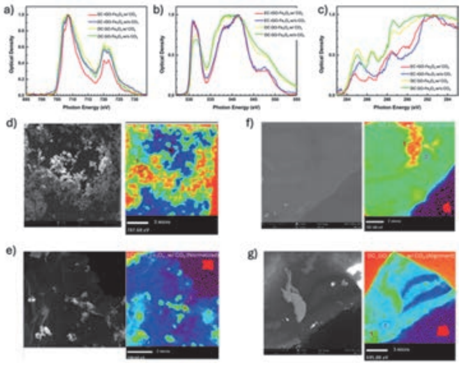

Fig. 1. (a) Fe L-edge, (b) O K-edge, and (c) C K-edge XAS spectra of EC rGO and DC GO, with and without CO_2 purging, all incorporated with Fe_3O_4 NPs. Corresponding STXM images outlining the Fe_3O_4 high-density areas of EC-rGO-Fe_3O_4 (d) w/o CO_2 and (e) w/ CO_2, and DC-GO-Fe_3O_4 (f) w/o and (g) w/ CO_2.

In the O *K*-edge (Fig. 1(b)), all samples show one π state (C=O) around 530-533.0 eV and σ state (C=O and O 2*p*-Fe 3*d*) around 537-545.0 eV, especially noted in the two DC GO-Fe_3O_4. Besides, the Fe_3O_4 characteres[2], typical of double Fe-t_{2g} and Fe-e_g states at 531.0 and 532.0 eV, are emerged in the first π peak. Through the EC method, the increase of reduced metallic states of Fe (i.e., Fe^0 and Fe^{2+}) and clear Fe 4s and 4p states become apparent at 531.0 and 545. 0 eV, respectively[2]. Compared to the only DC and EC rGO result[1], the oxygen absorption signal is dominant by the role of Fe_3O_4 NPs. No big difference is found between CO_2 purge or not. Figure 1(a) shows the Fe absorption spectra at the L_3 edge (~709.0 eV) and the L_2 edge (~722.0 eV), where they are split with the multiple crystal field and spin-orbit coupling. Two DC GO-Fe_3O_4 reveal the increasing shoulder at 707.5 eV, revealing the slight modulation of Fe_3O_4 NP after the EC method and CO_2 purge.

In summary, we exhibit the measurement of Fe_3O_4/GO composites in capturing CO_2 and the possible configurations when comparing EC rGO from DC solution, where the EC-rGO-Fe_3O_4 has shown the highest potential to capture CO_2.

[1] J. S. D. Rodriguez *et al.,* Carbon **185** (2021) 410.
[2] P.F. Teh *et al.*, J. Phys. Chem. *C* **117** (2013) 24213.

BL4U

STXM Analysis of Cathode Materials for Lithium-Ion Battery

E. Hosono[1,2], D. Asakura[1,2] and H. Yuzawa[3]
[1]*Research Institute for Energy Efficient Technologies, National Institute of Advanced Industrial Science (AIST), AIST Tsukuba Central 5, 1-1-1 Higashi, Tsukuba, Ibaraki 305-8565, Japan*
[2]*Global Zero Emission Research Center, AIST, AIST Tsukuba West, 16-1 Onogawa, Tsukuba, Ibaraki 305-8569, Japan*
[3]*UVSOR Synchrotron Facility, Institute for Molecular Science, Okazaki, Aichi 444-8585, Japan*

Toward the realization of a sustainable low-carbon society, development of clean energy devices is actively underway. Secondary batteries, which can directly store renewable energy such as solar and wind power as electricity, are attracting significant attention. Lithium-ion batteries (LIBs) with high energy density are used in electric vehicles. Moreover, they are promising for large-scale stationary storage batteries. As such expanding the practical use of LIBs, it is essential to not only improve the energy density but also ensure high safety. Therefore, establishment of highly safe operation and elucidation of degradation mechanisms are of particular importance.

Among various analytical methods of LIBs, we have focused on synchrotron soft X-ray spectroscopy and conducted detailed analyses of the 3*d* transition metals and oxygen, which are the main elements of the cathode materials. Furthermore, we have also focused on microspectroscopy, which provides local spatial information and detail spatial distribution of target species. Thus, we have reported on synchrotron soft X-ray micro-electron spectroscopy using 3DnanoESCA [1-3] and synchrotron soft X-ray Scanning Transmission X-ray Microscopy (STXM) using UVSOR BL4U [4, 5].

In this study, we have applied the STXM to LIB cathode electrode sheet with active material ($LiNi_{0.5}Co_{0.2}Mn_{0.3}O_2$). The thin sample for STXM was prepared by Focused Ion Beam-Scanning Electron Microscope (FIB-SEM).

Figure 1 shows an image of a STXM sample; the LIB electrode sheets typically consist of active material, carbon as a conductive additive, and a binder. Additionally, it is known that a solid electrolyte interphase (SEI) forms on the surface of the active material in LIBs. It is anticipated that the degradation state differs between the interior and surface of the active material. In other words, the electronic/chemical states should not be uniform in each particle of the active material. Therefore, it is expected that STXM-based microspectroscopy will provide valuable knowledge.

Figure 2 shows Mn L_3-edge absorption spectrum in a region of interest for a cathode active material ($LiNi_{0.5}Co_{0.2}Mn_{0.3}O_2$). We have obtained enough quality of spectrum from this sample. We will conduct detailed analysis including mapping, and proceed toward elucidating the battery degradation mechanism.

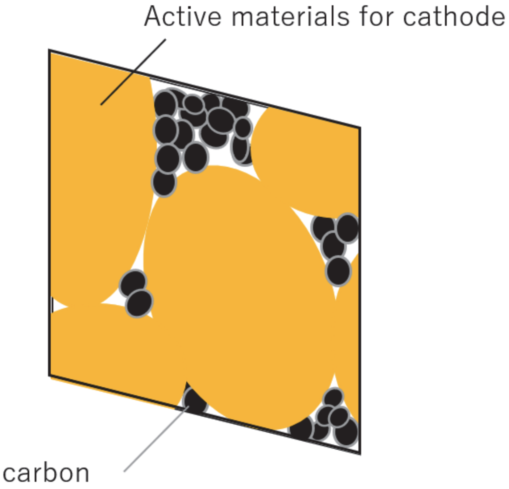

Fig. 1. Image of FIB thin section of LIB cathode electrode sheet with active material ($LiNi_{0.5}Co_{0.2}Mn_{0.3}O_2$) in STXM measurement. The structure of material is confidential until paper is published.

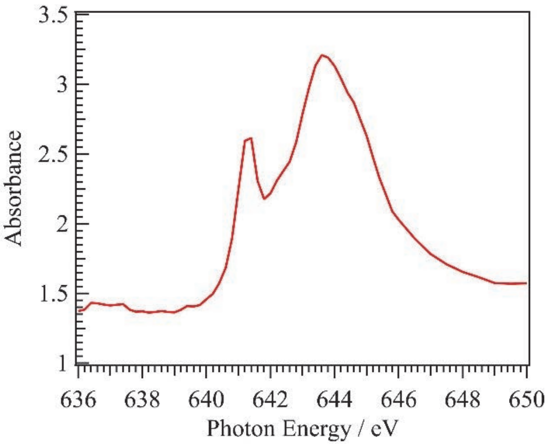

Fig. 2. Mn L_3-edge spectrum extracted from region of interest in FIB thin section of LIB cathode electrode sheet with active material ($LiNi_{0.5}Co_{0.2}Mn_{0.3}O_2$).

[1] K. Akada *et al*., Sci. Rep. **9** (2019) 12452.
[2] K. Akada *et al*., J. Electron Spectrsc. Relat. Phenom. **233** (2019) 64.
[3] W.X. Zhang *et al*., CrystEngComm. **25** (2023) 183.
[4] W.X. Zhang *et al*., Sci. Rep. **13** (2023) 4639.
[5] W.X. Zhang *et al*., J. Electron Spectrsc. Relat. Phenom. **266** (2023) 147338.

BL4U

Study of Localized Chemical State of Isoprene Rubber by STXM under Tensile-Stressed Condition

T. Ohigashi[1,2], F. Kaneko[3], H. Yuzawa[4] and H. Kishimoto[3]
[1]*Institute of Material Structure Science, High Energy Accelerator Research Organization, Tsukuba 305-0801, Japan*
[2]*Materials Structure Sciences, The Graduate University for Advanced Studies (SOKENDAI), Tsukuba 305-0801, Japan*
[3]*Sumitomo Rubber Industries Ltd., Kobe 651-0072, Japan*
[4]*UVSOR Synchrotron Facility, Institute for Molecular Science, Okazaki 444-8585, Japan*

In recent years, the Sustainable Development Goals (SDGs) have emerged as a framework guiding societal practices included in daily life. Among the various targets, the reduction of mass consumption represents a particularly critical challenge. Rubber, as a vital industrial material, is increasing its demand, especially driven by the expansion of the automobile society. In order to mitigate its consumption, it is necessary to establish a comprehensive Life Cycle Assessment (LCA) framework for rubber production, alongside the development of advanced rubber materials exhibiting enhanced functionalities, such as improved resistance to wear and mechanical failure.

A deeper understanding of the damage mechanisms in rubber materials is crucial for improving their properties. Damage in tire rubbers generally arises from a combination of chemical and mechanical factors. Recently, Mashita et al. investigated the mechanical degradation of rubber using four-dimensional X-ray tomography, revealing the creation of microvoids within deformed rubber pillars [1]. As a complementary approach aimed at elucidating the chemical aspects of mechanical damage, we have employed Scanning Transmission X-ray Microscopy (STXM). STXM enables the analysis of localized chemical states with a spatial resolution around 30 nm. Furthermore, STXM offers a relatively long working distance of ~300 µm, facilitating specialized experimental designs through the fabrication of customized sample cells. In the previous study, we developed a tensile-stress sample cell compatible with STXM and conducted *in-situ* measurements on rubber specimens [2].

An ultra-thin section (200 nm thick) of isoprene rubber was used as a sample and was attached on a tensile-stress sample grid. With changing tensile stress, 2-dimensioinal X-ray absorption spectroscopy (XAS) spectra around C K-edge (280~300 eV) were measured with 2 ms dwell time and 150 nm scanning step. Figure 1 shows the optical density images of the sample without (a, b) and with tensile stress (c, d) at 282 eV. In the tensile stress condition, the sample was stretched as 220% width for horizontal direction. Figure 1(b) and 1(d) were acquired from the same sample but at near different places to avoid radiation damage. Some bright spots in the images are considered as carbon black particles. XAS spectra under these conditions are shown in Fig. 2. Height of the spectra with tensile stress is ~52% of one without tensile stress because the sample was thinned by stretching. The main spectral change is ratio between intensity at π* (285.3 eV) and σ* (292.2 eV). The ratio (π*/σ*) changes from 0.97 to 1.12. This change is currently under discussion including formation of microvoids on the sample.

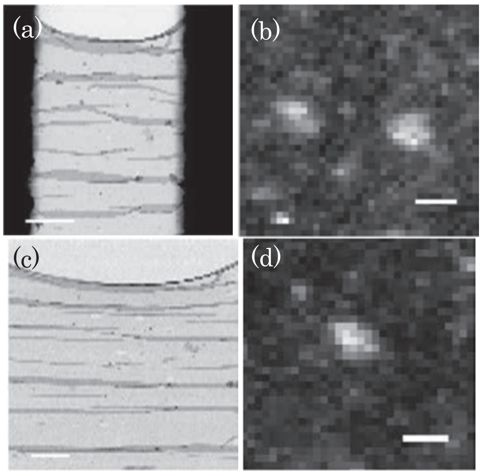

Fig. 1. Optical density images of the isoprene rubber (a, b) without and (c, d) with tensile stress at 282 eV. Scale bars are (a, c) 100 µm and (b,d) 1 µm, respectively.

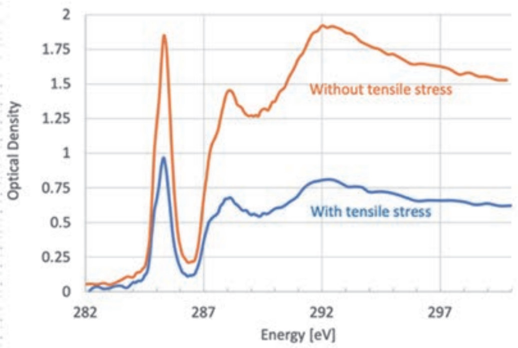

Fig. 2. C K-edge XAS spectra of the isoprene rubber without /with tensile stress.

[1] R. Mashita *et al.*, Sci. Rep. **13** (2023) 5805.
[2] T. Ohigashi *et al.*, UVSOR Activity Report **51** (2023) 84.

BL4U

Heterostructure of WO_3/V_2O_5 for Electrochromic and Energy Storage: A View by Spectro-Microscopy

K. T. Arul[1], P. C. Wang[2,1], T. Araki[3], T. Ohigashi[3,4],
D. H. Wei[2] and C. L. Dong[1]
[1]*Department of Physics, Tamkang University, Tamsui 25137, Taiwan*
[2]*Graduate Institute of Manufacturing Technology, National Taipei University of Technology, Taipei 10608, Taiwan*
[3]*UVSOR Synchrotron Facility, Institute for Molecular Science, Okazaki 444-8585, Japan*
[4]*Photon Factory, High Energy Accelerator Research Organization, Tukuba 305-0801, Japan*

To address high energy consumption and related energy issues, such as low energy and power densities and stability, a combination of electrochromism and energy storage has been explored to support both energy saving and charge storage, leading to the development of electrochromic supercapacitor (ECS) devices. ECS technology can control thermal radiation, and mitigate the need for artificial lighting in buildings, enhance energy efficiency, and even power electrical systems. These devices have been applied in energy harvesting, liquid crystal displays, wearable electronic devices, etc., [1]. Several metal oxides and their nanostructures, heterostructures, and composites have been extensively studied as ECS materials [2]. Among them, vanadium and tungsten oxides are particularly promising owing to their multi-oxidation states, high electronic conductivity, redox activity, structural stability, and high optical contrast.

The fundamental understanding of the electrochromic energy storage mechanism in the heterostructure is essential. In this study, the bifunctional WO_3/V_2O_5 thin films (~150-200 nm) were prepared using the sol-gel method. The XRD analysis revealed the presence of the (001) and (020) planes, indicating the crystalline phases of V_2O_5 and WO_3, respectively. The ultraviolet-visible spectroscopy revealed that the thin film exhibited the optical switching contrast of 17.4% between bleached and colored states, with a coloration efficiency of 10.78 cm^2/C. Moreover, the specific capacitance of WO_3/V_2O_5 was 8 F/g, which is higher than that of the individual V_2O_5 and WO_3 films, demonstrating its potential as a bifunctional material for smart film and charge storage. In this work, scanning transmission X-ray microscopy (STXM) is employed to investigate the active regions and/or elements responsible for the electrochromic energy storage performance.

Figure 1 shows the optical density and corresponding stack-mapped STXM images for the V L- and O K-edge XAS of the samples. The V L-edge originates from the V 2p-to-3d unoccupied state [3]. In the WO_3/V_2O_5 heterostructure, the intensity of the V L_3-edge peak is slightly higher at surface of the heterostructure. The O K-edge XAS, which arises from O 1s-to-2p transitions hybridized with V 3d and W 5d states, was also measured. The peaks a_1 and a_4 correspond to, respectively, the O 1s-to-2p states hybridized with W 5d-t_{2g} and 5d-e_g states. The peaks a_2 and a_3 are attributed to the O 1s-to-2p states hybridized with V 3d-t_{2g} and 3d-e_g states, respectively. The spectral evolutions indicate a higher concentration of oxygen vacancies at the surface than in the core, particularly around W sites, providing more active sites for electrochromic energy storage.

In contrast, the V L- and O K-edge XAS-STXM of WO_3/V_2O_5 heterostructure after cyclic voltammetry (CV) treatment shown in Fig.1b, revealed a stronger interaction between V and W through oxygen 2p states. Notably, the charge states of both V and W are more reduced at the surface of the particle compared to the core region, suggesting that both V and W in the heterostructure are electrochemistry active. The stability of such a defective heterostructure, the durability of these active sites, and whether both active sites are jointly (or separately) responsible for the electrochromic and charge storage functionalities remain to be explored.

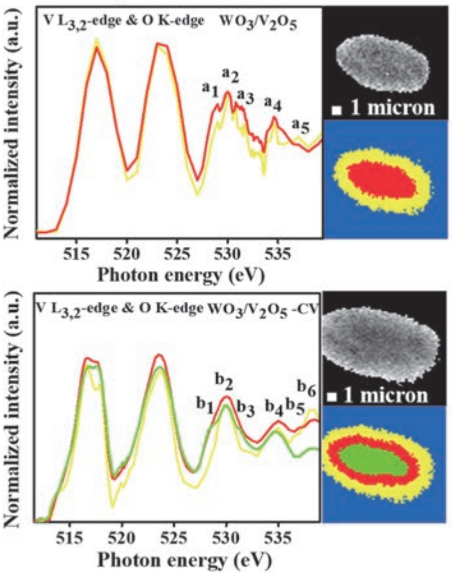

Fig. 1. Optical density and stack-mapped STXM images, and the corresponding V $L_{3,2}$- and O K-edge XAS of (a) WO_3/V_2O_5 and (b) WO_3/V_2O_5-CV.

[1] D. K. Pathak *et al.*, Mater. Horiz. **9** (2022) 2949.
[2] S. Zhang *et al.*, Energy Environ. Sci. **11** (2018) 2884,
[3] Q. Lu *et al.*, Adv. Funct. Mater. **28** (2018) 1803024.

BL4B

Soft X-ray Absorption Study of Semiconductor Photocatalysts Excited with Steady UV Light

Y. H. Chew[1], H. Onishi[1,2], N. Ichikuni[3] and T. Yoshida[4]
[1]*School of Science, Kobe University, Kobe 657-8501, Japan*
[2]*Division of Advanced Molecular Science, Institute for Molecular Science, Okazaki 444-8585, Japan*
[3]*Graduate School of Engineering, Chiba University, Chiba 263-8522, Japan*
[4]*Graduate School of Engineering, Nagoya University, Nagoya 464-8603, Japan*

Materials conversion on semiconductor photocatalysts has been intensively studied worldwide. Downhill reactions, in which the Gibbs free energy decreases during the conversion of reactants to products, have been successfully integrated into our society [1]. Artificial photosynthesis, a category of uphill reactions involving the oxidation of water, is being developed for societal implementation in the near future [2]. In addition, fundamental studies are being conducted to uncover new scientific discoveries related to light-driven, efficient materials conversion.

Here, in collaboration with Prof. Hiroshi Iwayama of UVSOR, we apply soft X-ray absorption to the characterization of semiconductor photocatalysts under UV light irradiation for band-gap excitation. A series of metal oxide photocatalysts including sodium tantalate ($NaTaO_3$), strontium titanate ($SrTiO_3$), titanium oxide (TiO_2), tin oxide (SnO_2), and zinc oxide (ZnO) were investigated in a beam time in FY2024.

The photocatalyst particles were formed into disks of 7 mm diameter. The disks were placed in a vacuum chamber, irradiated with incident X-rays, and the fluorescent X-rays were detected with a silicon drift detector (SDD). The detector was capped with a 150 nm thick aluminum film (LUXEL, TF110) to minimize the contribution of stray UV light to the detector response (Fig. 1). The capping device is deposited at UVSOR. Users are encouraged to use the device when operating the SDD under UV or visible light irradiation.

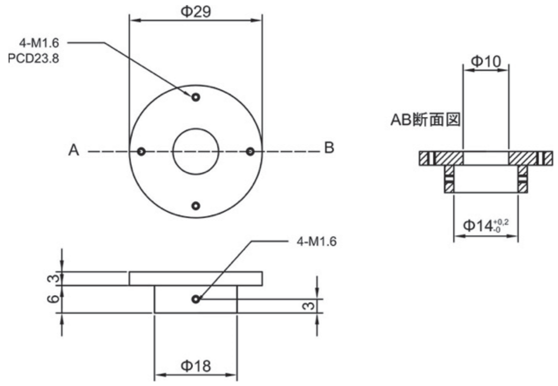

Fig. 1. A devise capping the SDD with the aluminum filter for fluorescence yield detection of oxygen K edge absorption spectrum under UV-light irradiation.

Figure 2 shows a set of fluorescence yield spectra at the oxygen K-edge observed on a $NaTaO_3$ photocatalyst doped with Sr^{2+} cations, in the presence and absence of UV light provided by a Hg–Xe lamp (200 W).

In the oxygen K-edge, electron transition from O1s to O2p orbitals of $NaTaO_3$ particles was detected. The O2p orbitals are hybridized with Ta5d orbitals to form the conduction band in perovskite-structured $NaTaO_3$. The hybridized O2p orbitals are thus split into t_{2g} and e_g levels, one at 532.6 eV and the other at 537.7 eV, according to the ligand field in TaO_6 octahedra.

The t_{2g} and e_g bands shifted to the low energy side under UV irradiation. The shifted bands induced differentiated forms in the difference spectrum. A possible reason for the band shifts is the conduction band partially filled with electrons excited across the band gap, where the oxidation state of some Ta cations decreased from 5+ to 4+.

The X-ray absorption of electronically excited metal oxides has been studied using ultrashort light pulses [3]. Here, we showed that the absorption spectrum was also sensitive to steady light irradiation. This study was supported by JSPS KAKENHI (grant number 22H00344).

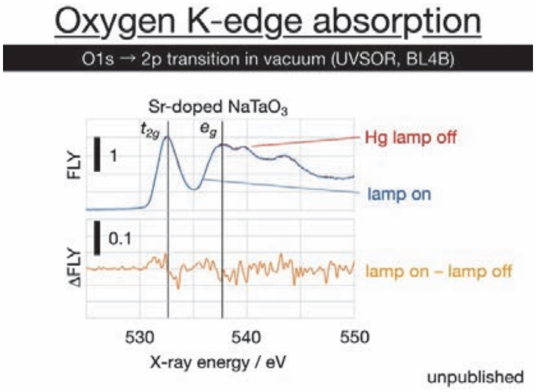

Fig. 2. Oxygen K edge absorption spectrum of a $NaTaO_3$ photocatalyst doped with Sr^{2+} cations in the absence (red spectrum) and presence (blue spectrum) of UV irradiation. The difference spectrum induced by the irradiation is shown in orange color at the bottom.

[1] A. Fujishima *et al.*, J. Photochem. Photobio. C **1** (2000) 1.
[2] H. Onishi, ChemSusChem **12** (2019) 1825.
[3] Y. Uemura *et al.*, J. Phys. Chem. Lett. **13** (2022) 4207.

BL4B

Oxygen K-Edge XAS Study of $Eu_2Zr_2O_7$

S. Yoshioka[1], E. Kobayashi[2] and K. Oudaira[3]
[1]*Department of Applied Quantum Physics and Nuclear Engineering, Kyushu University, Fukuoka 819-0395, Japan*
[2]*Kyushu Synchrotron Light Research Center, Saga 841-0005, Japan*
[3]*Graduate school of Advanced Integration Science, Chiba University, Chiba 263-8522, Japan*

Rare earth zirconates ($Re_2Zr_2O_7$) such as $Eu_2Zr_2O_7$ and $Gd_2Zr_2O_7$ exhibit attractive potential as functional materials for thermal barrier coatings and nuclear fuel inert matrixes. $Re_2Zr_2O_7$ displays two types of crystal structures depending on the ionic radius ratio between Re and Zr. There are the pyrochlore structure and the oxygen deficient fluorite structure, with the former being considered a cation and oxygen vacancy ordered form of the latter. The transformation between pyrochlore and defective fluorite structures can be described as cationic disordering. Regrading the local coordination on the disordering, Re ions partly move from eight-coordinated site (CN8) to a six-coordinated site (CN6), whereas Zr ions partly move from CN6 to CN8. The structure changes related to the cationic disorder of pyrochlore under swift heavy ion (SHI) irradiation have been reported using diffraction techniques and transmission electron microscopy observations. X-ray absorption near edge structure (XANES) spectroscopy is a powerful method for structure characterization, providing information on local atomic coordination and electronic structures. Moreover, XANES offers a significant advantage for the elemental selectivity of the multi-cation compounds such as pyrochlore. In this study, we investigated oxygen local structure change in $Eu_2Zr_2O_7$ induced by SHI using X-ray absorption spectra (XAS).

Polycrystalline Eu_2Zr_2O samples were synthesized via a solid-state reaction. Stoichiometric amounts of Eu_2O_3 and ZrO_2 oxides were intimately mixed and pressed into disc at 100 MPa. Finally, the discs were sintered under air at 1500 °C using an electric furnace.

The sintered Eu_2Zr_2O sample was confirmed to have pyrochlore structure by X-ray diffraction (XRD). SHI irradiation experiments with 200 MeV Xe ions at fluences ranging from 5×10^{11} up to 1×10^{13} cm^{-2} were performed at the H1 beamline of the tandem ion accelerator facility in the Japan Atomic Energy Agency (JAEA)-Tokai.

O K-edge XANES measurements were performed on the BL4B beamline of UVSOR Okazaki, Japan, using the partial fluorescence yield (PFY) method. A varied-line-spacing plane gratings monochromator provided the O K-edge in the energy regions 520–560 eV. The samples were positioned with their surface perpendicular to the incident X-ray beam. Fluorescence X-rays of O K_α was collected using an energy dispersible silicon drift detector (SDD).

The O K-edge XANES spectra (at 525 eV) are shown in Fig. 1 for the Eu_2Zr_2O powder sample and reference bixbyite Eu_2O_3 and monoclinic ZrO_2 powder samples. The intensity of each spectrum was normalized to a value of 1 at 555 eV after the removal of the background intensity.

The spectrum shape of $Eu_2Zr_2O_7$ is clearly different from those of standard samples Eu_2O_3 and ZrO_2. The peaks A – C in the spectrum of Eu_2O_3 were assigned to transitions from the O 1s orbitals to unoccupied bands derived from the Eu 5d-π, 6p, 5d-σ orbitals, respectively [1].

Detailed analysis on the local environment of O in $Eu_2Zr_2O_7$ is in progress, employing a combined approach of XANES and first principles band structure calculations.

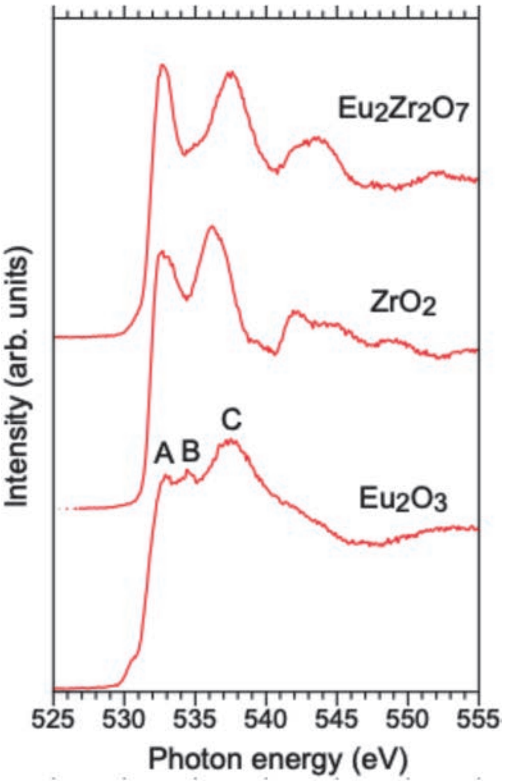

Fig. 1. O K-edge XANES spectra of pyrochlore Eu_2Zr_2O, including references spectra from bixbyite Eu_2O_3 and monoclinic ZrO_2 powder for comparison.

[1] A. B. Altman, *et al.*, Dalton Trans. **45** (2016) 9948.

BL5U

Micro-ARPES Study of the Electronic Structure in Kagome Superconductor $LaRh_3B_2$

T. Kato[1], K. Nakayama[2], T. Osumi[2], S. Souma[1,3], A. Honma[2], K. Tanaka[4,5],
T. Takahashi[2] and T. Sato[1,2,3,6,7]
[1]*Advanced Institute for Materials Research (WPI-AIMR), Tohoku University, Sendai 980-8577, Japan*
[2]*Department of Physics, Tohoku University, Sendai 980-8578, Japan*
[3]*Center for Science and Innovation in Spintronics (CSIS), Tohoku University, Sendai 980-8577, Japan*
[4]*UVSOR Synchrotron Facility, Institute for Molecular Science, Okazaki 444-8585, Japan*
[5]*School of Physical Sciences, The Graduate University for Advanced Studies (SOKENDAI), Okazaki 444-8585, Japan*
[6]*International Center for Synchrotron Radiation Innov1ation Smart (SRIS), Tohoku University, Sendai 980-8577, Japan*
[7]*Mathematical Science Center for Co-creative Society (MathCCS), Tohoku University, Sendai 980-8578, Japan*

Ternary rare-earth compounds RT_3X_2 (where R denotes a rare-earth element, T a transition metal, and X typically B, Si, or Ga) are an extensively studied class of intermetallic materials. This family has been attracted attention over the years primarily due to its rich and intriguing physical properties, including various types of magnetic ordering and superconductivity, depending on the specific elemental composition. More recently, stimulated by significant advances in the study of geometrically intriguing kagome lattices, there has been a marked revival of interest in RT_3X_2 compounds, as they feature an ideal kagome lattice formed by the T atoms. The kagome lattice, composed of corner sharing triangles, is known for its potential to host exotic electronic states, such as dispersionless flat bands, linearly dispersing Dirac points analogous to those in graphene, saddle-point van Hove singularity, and topologically non-trivial characters. There is growing interest in elucidating the relationship between the kagome lattice-derived electronic band structures and the physical properties of RT_3X_2 [1]. Nevertheless, despite this renewed focus, the application of experimental techniques capable of directly probing intrinsic electronic states, such as angle-resolved photoemission spectroscopy (ARPES), remains limited for RT_3X_2 [2].

In this work, we have focused on $LaRh_3B_2$, a rare material displaying superconductivity within the RT_3X_2 series. We performed detailed studies of its electronic structure utilizing high-resolution angle-resolved photoemission spectroscopy (ARPES). The experiments were conducted with micro-focused synchrotron radiation beam at beamline BL5U at UVSOR. Clean surfaces necessary for ARPES were obtained by cleaving the crystals *in-situ* in an ultrahigh vacuum better than 1×10^{-10} Torr.

Figure 1 shows representative ARPES data for $LaRh_3B_2$, displaying the second derivative intensity plot measured along the Γ-M high-symmetry line in the hexagonal Brillouin zone (inset) in the normal state (T = 40 K). Our data show multiple hole-like band dispersions centered near the Γ point, whose highest branch approaches the Fermi level (E_F), in agreement with previous work [2]. Our measurements also revealed a hole-like band topped 0.3 eV below E_F at the M point. Through comparing the observed band dispersions with those calculated by density functional theory as well as conducting photon energy dependent ARPES measurements, we found that some of the observed bands are attributed to two-dimensional electronic states at the surface. To clarify the origin of the surface states, we have carried out slab calculations, and found their intriguing electronic and structural properties.

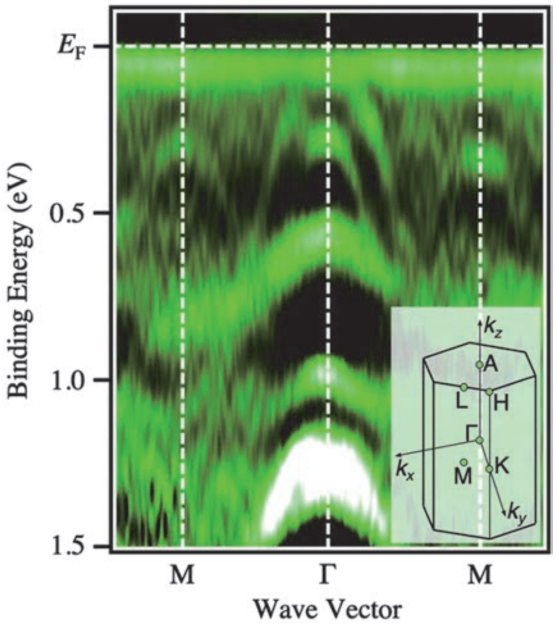

Fig. 1. Plot of second-derivative ARPES intensity measured in the normal state along the ΓM high-symmetry line in $LaRh_3B_2$.

[1] S. Chaudhary *et al.*, Phys. Rev. B **107** (2023) 085103.
[2] Y. Iida *et al.*, Physica B **351** (2004) 271.

BL5U

Band Structure of Monolayer Germanene Grown on Ag Revealed by ARPES

T. Terasawa[1,2], S.Suzuki[1], D. Katsube[3], S. Tanaka[4] and K. Tanaka[5]
[1]Advanced Science Research Center, Japan Atomic Energy Agency, Tokai 319-1195, Japan
[2]Institute of Industrial Science, The University of Tokyo, Meguro 153-8505, Japan
[3]Japan Fine Ceramics Center, Nagoya 456-8587, Japan
[4]SANKEN, The Institute of Scientific and Industrial Research, The University of Osaka, Ibaraki 567-0047, Japan
[5]UVSOR Synchrotron Facility, Institute for Molecular Science, Okazaki 444-8585, Japan

Germanene is a monolayer material composed of Ge atoms arranged in a honeycomb lattice. Owing to the spin–orbit interaction in Ge, germanene adopts a buckled atomic configuration. As a result, it is predicted to exhibit a Dirac cone like that of graphene with a high Fermi velocity while also possessing a band gap of 23.9 meV [1]. These characteristics have spurred interest in germanene as a next-generation semiconductor material.

We have developed a novel synthesis method to produce high-quality germanene, as reported by J. Yuhara *et al.* [2]. When an Ag thin film is deposited on a Ge(111) substrate and subsequently heated, Ge atoms diffuse from the substrate to the Ag film surface. Upon cooling, a monolayer germanene forms on the Ag film surface. This segregated germanene exhibits larger domain sizes and long periodic structures. Moreover, the formation of germanene was confirmed by the characteristic Raman peaks unique to germanene [3]. The availability of high-quality germanene can facilitate angle-resolved photoemission spectroscopy (ARPES) measurements. Our ARPES measurements conducted at UVSOR BL5U in 2023 successfully observed germanene-derived bands that are distinct from those of bulk Ag or Ag–Ge alloys [4]. In this work, we aim to further refine these observations by elucidating the band structure of germanene, specifically determining whether the observed bands exhibit a cone-like or saddle-like nature. This distinction is crucial, as in the case of silicene, the saddle-like structure induced by the Ag substrate was often misinterpreted as the π-bands of silicene [5].

Figure 1(a) shows the ARPES intensity map along the Γ-K_{Ge}-M_{Ag} line (kx direction) of germanene grown on an Ag(111) thin film, obtained using 40 eV light. Here, K_{Ge} and M_{Ag} correspond to the K and M points in the Brillouin zone of germanene and Ag(111)-(1×1) surface, respectively. In addition to the prominent Ag 5sp band, a Λ-shaped structure is observed, as indicated by the red broken lines. Figure 1(b) shows the ARPES intensity map for energy (E)-ky plane at kx = 0.9 $Å^{-1}$, corresponding to a white broken line in Fig. 1(a), where the ky direction is perpendicular to the kx direction. The band around -1.5 eV, which corresponds to the Λ-shaped band in Fig. 1(a), exhibits an almost flat but slightly concave-down feature, suggesting that it is not a saddle point but rather a cone-like structure. Therefore, we attributed this band not to the Ag bands but to the π-band of germanene. The difference in the band gradients along kx and ky directions is likely due to the hybridization with Ag.

In summary, we synthesized germanene on the Ag(111) surface by Ge segregation and investigated its electronic structure using ARPES. Our results provide the first indication of a π-band in germanene segregated on Ag(111), as revealed by ARPES intensity maps in both the E-kx and E-ky planes.

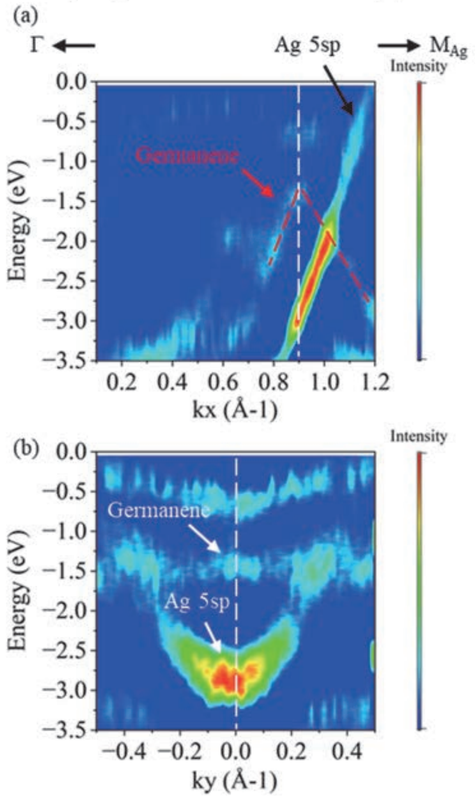

Fig. 1. (a, b) ARPES intensity plots along kx and ky lines. The plots are the second derivative of the raw data to highlight the band features.

[1] C. C. Liu *et al.*, Phys. Rev. B **84** (2011) 195430.
[2] J. Yuhara *et al.*, ACS Nano **12** (2018) 11632.
[3] S. Suzuki *et al.*, Adv. Funct. Mater. **31** (2021) 2007038.
[4] T. Terasawa *et al.*, UVSOR Activity Report **51** (2023) 97.
[5] S. K. Mahatha *et al.*, Phys. Rev. B **89** (2014) 201416.

BL5U

Spin-Polarized Band Mapping in Bi_2Sb_3 Surface States

J. Okabayashi[1] and K. Tanaka[2]
[1]*Research Center for Spectrochemistry, The University of Tokyo, Bunkyo-ku, Tokyo 113-0033, Japan*
[2]*UVSOR Synchrotron Facility, Institute for Molecular Science, Okazaki 444-8585, Japan*

Spintronics is a rapidly emerging field of science and technology that will most likely have a significant impact on the future of all aspects of electronics. Understanding magnetism of surfaces, interfaces, and nanostructures is greatly important for realizing the spintronics which aims to control and use the function of spin as well as the charge of electrons. Spin- and angle-resolved photoemission spectroscopy (spin-resolved ARPES) is one of the most powerful experimental techniques to investigate the magnetic properties of such materials, where one can know the "complete" information of the electronic states of materials, that is, energy, momentum, and spin direction. Recent development of high energy and angle-resolved photoelectron analyzer as well as the contemporary light sources makes it possible for the photoemission spectroscopy to investigate not only band structures but also many body interactions of electrons in solids. However, appending the spin resolution to photoemission spectroscopy is quite difficult because of an extremely low efficiency (10^{-4}) of Mott-type spin detections.

Recently, very low-energy electron diffraction (VLEED-type) spin detector with 100 times higher efficiency than that of conventional Mott-type has been developed and spin-resolved ARPES has been started to be realized [1-3]. So far, most of the spin-resolved ARPES systems are using the single-channel detector and efficiency is still a problem. We have developed high-efficient spin-resolved ARPES system with multi-channel detection (we call "image-spin" detection) to achieve the 100 times better efficiency and the 10 times better momentum resolution than the current spin-resolved ARPES system, which can be a breakthrough in this research field.

Figure 1 displays the ARPES and spin-resolved ARPES images of the topological surface states in Bi_2Sb_3 after cleaving the sample *in-situ* to obtain clean surface. Linearly crossing surface bands at the Dirac points are observed in ARPES, and spin-resolved states for both up and down spin states are distinctly identified with high resolution.

According to rough estimates, the efficiency of spin-resolved ARPES is 100 times greater than that of the single-channel detection systems currently in use worldwide. The imaging detection of spin-resolved mapping can be accomplished using spin manipulation techniques to separate the photoelectrons into up and down spins before their injection into the VLEED target. A new "spin manipulator" can alter the spin direction of the passing electrons in any orientation using adjustable electric and magnetic fields. The installation of the spin manipulator and the optimization of the spin target deposition conditions have significantly enhanced the spin-resolved images, allowing us to achieve spin-resolved images with momentum resolution comparable to that of conventional ARPES.

We are currently fine-tuning the lens parameters of the spin manipulator to capture spin information in the remaining three axial directions. This technique expands the research field by enabling efficient detection of spin-resolved band structures using spin-resolved ARPES.

[1] C. Bigi *et al.*, J. Synchrotron Rad. **24**, (2017) 750.
[2] T. Okuda, J. Phys.: Condens. Matter **29** (2017) 483001.
[3] F. Ji *et al.,* Phys. Rev. Lett. **116** (2016) 177601.

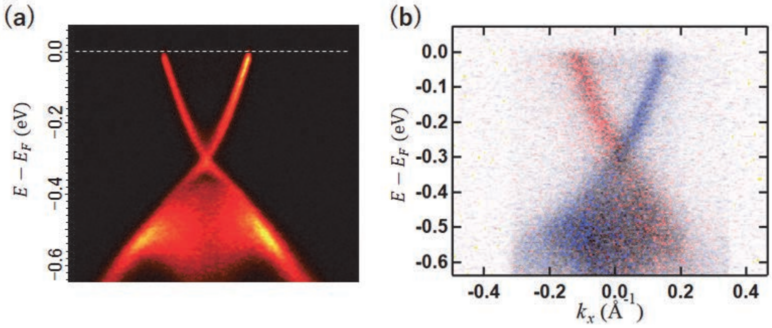

Fig. 1. Band dispersion mapping of Bi_2Se_3 taken at 55 eV photon energy. (a) ARPES and (b) Spin-resolved ARPES.

BL5U

Essential Ingredients for Pseudogap of Electron-Doped Cuprates Studied by Angle-Resolved Photoemission Spectroscopy

M. Miyamoto[1], M. Horio[1], K. Morioya[2], A. Takahashi[3], K. Tanaka[4], Y. Koike[3],
T. Adachi[2] and I. Matsuda[1]
[1]*Institute for Solid State Physics, the University of Tokyo, Kashiwa, Chiba 277-8581, Japan*
[2]*Department of Engineering and Applied Sciences, Sophia University, Tokyo 102-8554, Japan*
[3]*Department of Applied Physics, Tohoku University, Sendai 980-85879, Japan*
[4]*UVSOR Synchrotron Facility, Institute for Molecular Science, Okazaki 444-8585, Japan*

It has been widely accepted that, in addition to carrier doping, post-growth reduction annealing process is necessary to induce superconductivity in electron-doped cuprates $R_{2-x}Ce_xCuO_4$ (R: rare earth) with the so-called T'-type structure [1,2]. Neutron-scattering studies suggested that annealing removes excess impurity oxygen atoms at the apical site [3-5]. Stronger annealing, which implies further removal of apical oxygens, enhances the transition temperature T_c [6]. Horio *et al*. found that efficient annealing strongly suppresses the pseudogap, which is believed to compete with superconductivity [7]. The superconducting properties of the T'-type cuprates thus strongly depend on the degree of annealing.

On the other hand, recent studies have stressed the importance of electron doping caused by annealing. Angle-resolved photoemission spectroscopy (ARPES) studies revealed the increase of electron concentration by reduction annealing due to the creation of oxygen deficiencies in the regular sites [7-9]. Song *et al*. [10] reported that the pseudogap depends only on the electron doping level after sufficient reduction annealing. Therefore, the key factor of the pseudogap and superconductivity in electron-doped cuprates remains elusive.

To separate the effects of annealing and electron doping on the electronic structure, we previously carried out ARPES measurements on the as-grown samples of the electron-doped cuprate $Pr_{1.22}La_{0.7}Ce_{0.08}CuO_4$ and doped electrons by K adsorption on the sample surface, which should not influence the crystal structure. As a result, we found the signature of pseuedogap suppression by K adsorption [11]. In this proposal, we performed more detailed investigation into the influence of K adsorption, and also measured $Pr_{1.20}La_{0.7}Ce_{0.10}CuO_4$ annealed sample for comparison, which was annealed with an improved method called dynamic annealing [9,12,13].

ARPES measurements were performed for the as-grown $Pr_{1.22}La_{0.7}Ce_{0.08}CuO_4$ and the annealed $Pr_{1.20}La_{0.7}Ce_{0.10}CuO_4$ samples at BL5U at T = 20 K. By dosing K for the as-grown $Pr_{1.22}La_{0.7}Ce_{0.08}CuO_4$, the Fermi surface transformed from disconnected square shape [Fig. 1(a)] to continuous circular shape [Fig. 1(b)], which indicates pseudogap closing. The energy distribution curves (EDCs) at the node [Fig. 1(c)] and at the hot spot [Fig. 1(d)] show pseudogap suppression after K dosing. The increase in the electron concentration by K dosing estimated from Fermi surface area was approximately 0.12 per Cu site, which shows good reproducibility with previous measurements [11]. We further compared the results with that of the annealed $Pr_{1.20}La_{0.7}Ce_{0.10}CuO_4$ sample and evaluated the influence of apical oxygen removal by reduction annealing.

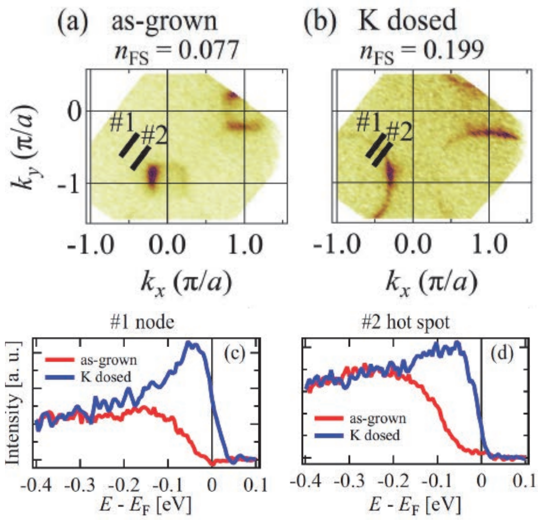

Fig. 1. Fermi surface maps for the as-grown $Pr_{1.22}La_{0.7}Ce_{0.08}CuO_4$ sample (a) before and (b) after K dosing. EDCs at the (c) node and (d) hot spot for each surface condition.

[1] Y. Tokura *et al*., Nature **337** (1989) 345.
[2] H. Takagi *et al*., Phys. Rev. Lett. **62** (1989) 1197.
[3] P. Radaelli *et al*., Phys. Rev. B **49** (1994) 15322.
[4] A. Schultz *et al*., Phys. Rev. B **53** (1996) 5157.
[5] M. Fujita *et al*. J. Phys. Soc. Jpn. **90** (2021) 105002.
[6] J. Kim *et al*., Physica C **209** (1993) 381.
[7] M. Horio *et al*., Nat, Commun. **7** (2016) 10567.
[8] M. Horio *et al*., Phys. Rev. B **98** (2018) 020505.
[9] C. Lin *et al*., Phys. Rev. Research **3** (2021) 013180.
[10] D. Song *et al*., Phys. Rev. Lett. **118** (2017) 137001.
[11] M. Miyamoto *et al*., UVSOR Activity Report **51** (2023) 98.
[12] Y.-L. Wang *et al*., Phys. Rev. B **100** (2009) 094513.
[13] Y. Lee *et al*., J. Phys. Soc. Jpn. **93** (2024) 054701.

BL5U

Resonant ARPES Study for Thermoelectric Property of Layered Ce-Based Compounds

D. Goto[1], K. Kuga[1], M. Matsunami[1,2,3] and T. Takeuchi[1,2,3]
[1]*Toyota Technological Institute, Nagoya 468-8511, Japan*
[2]*Research Center for Smart Energy Technology, Toyota Technological Institute, Nagoya 468-8511, Japan*
[3]*MIRAI, Japan Science and Technology Agency, Tokyo 102-0076, Japan*

The thermoelectric devices, which can convert heat and electricity using Seebeck and Peltier effects, have been considered as one of the most promising choices for energy saving technologies. However, such a thermoelectric generation has not been widely applied due to its low energy conversion efficiency. For evaluating a performance of thermoelectric materials directly related to conversion efficiency, the power factor $PF = S^2/\rho$ where S and ρ are Seebeck coefficient and electrical resistivity, respectively, is frequently used [1]. It is therefore necessary to search for materials possessing large PF by addressing the trade-off relationship between low ρ and large $|S|$.

It is known that in intermetallic compounds called heavy fermion systems, the low ρ and large $|S|$ coexist. This can be caused by the characteristic electronic structure formed by the hybridization between conduction (c) and f electrons. However, in heavy fermion systems, there is a serious problem concerning the sign of S, which cannot be determined solely in terms of the energy dependence of the electron density of states as in most simple metals. Therefore, the energy dependence of the relaxation time and group velocity of quasiparticles, both of which are ignored in many cases [1], should be taken into account.

The main purpose of this research is to establish a methodology for experimentally evaluating the energy dependence of the relaxation time and group velocity of quasiparticles in the vicinity of the Fermi level (E_F) using ARPES. In this study, we focus on the typical heavy fermion systems CeTIn$_5$ (T = Co, Rh, Ir) with a layered crystal structure, which show relatively high large thermoelectric performance at low temperature. In the case of Ce-based compounds, the main part of c-f hybridization bands locates just above E_F in contrast to Yb-based cases. Therefore, for clearly observing the c-f hybridization bands and analyzing them in detail, the photoemission signal Ce 4f electrons should be enhanced by using resonance condition.

Single crystals of CeTIn$_5$ (T = Co, Rh, Ir) were prepared by the In-flux method. Clean sample surfaces were obtained by *in-situ* cleaving. The ARPES measurements were performed at BL5U. The photon energies of 115 eV and 121 eV were selected as the off-resonance and on-resonance condition for Ce 4d-4f edge, respectively. The resonance energy, as generally used in previous studies [2], was also confirmed by our constant initial state (CIS) measurements.

Figure 1 shows the obtained ARPES image of CeCoIn$_5$ (001) surface at 9 K measured with the photon energy of 115 eV (off-) and 121 eV (on-resonance), respectively. The highly dispersive bands due to mainly Co 3d electrons are clearly observed and basically similar between on- and off-resonance condition [2]. The impact of nearly localized Ce 4f electrons is observed at around E_F and 0.25 eV due to spin-orbit splitting, as clearly confirmed in the angle-integrated spectra. From the linewidth of the band dispersion near E_F, the energy dependent analysis for the relaxation time and group velocity of quasiparticles for CeCoIn$_5$ can be determined, and is now in progress.

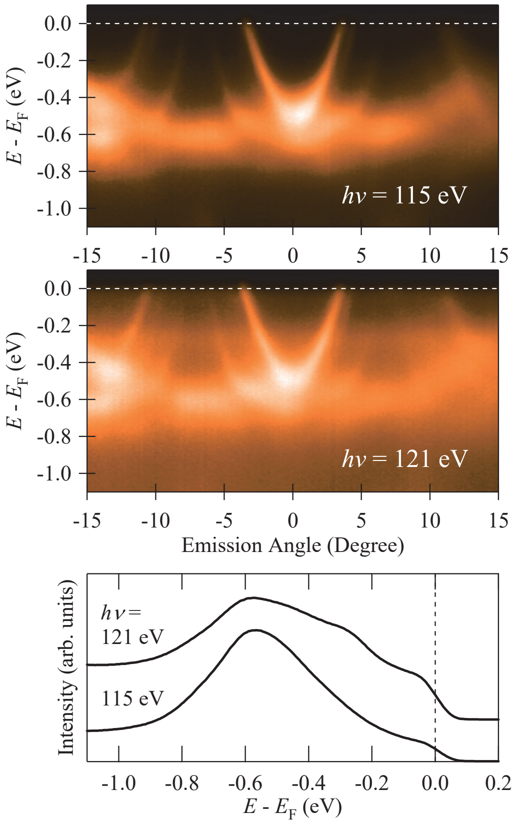

Fig. 1. ARPES image of CeCoIn$_5$ at 9 K measured with photon energies of 115 eV (top) and 121 eV (middle). The bottom figure shows the angle-integrated spectra.

[1] T. Takeuchi, J. Thermoelectrics Soc. Jpn. **9** (2012) 1.
[2] Q.Y. Chen *et al.*, Phys. Rev. B **96** (2017) 045107.

BL5U

Angle-Resolved Photoemission Study of Olivine-Type $LiMnPO_4$ Bulk Single Crystal

T. Ito[1,2], Y. Hatae[1], M. Nakatake[3], S. Takakura[2], K. Tanaka[4,5],
Y. Fujiwara[6], T. Taishi[6] and Y. Iriyama[1]
[1]*Graduate School of Engineering, Nagoya University, Nagoya 464-8603, Japan*
[2]*Synchrotron radiation Research center, Nagoya University, Nagoya 464-8603, Japan*
[3]*Aichi Synchrotron Radiation Center, Seto 489-0965, Japan*
[4]*UVSOR Facility, Institute for Molecular Science, Okazaki 444-8585, Japan*
[5]*The Graduate University for Advanced Studies, Okazaki 444-8585, Japan*
[6]*Faculty of Engineering, Shinshu University, Nagano 380-8553, Japan*

With the recent expansion of the use of lithium-ion secondary batteries, development of all-solid-state batteries using lithium-ion conductive inorganic solid electrolytes has been progressing to realize further safety, high energy density, and high output, etc. On the other hand, the valence-band electronic structure, which is essential to understand the relation between lithium-ion and electron conductivity in solid-state energy storage materials, has not been well elucidated yet, though the chemical analysis using operand X-ray photoemission has intensively been applied on the system [1,2]. To clarify the effect of lithium on the electronic structure of cathode material, we have performed angle-resolved photoemission spectroscopy (ARPES) measurements on olivine-type $LiMnPO_4$ [3], which has expected to be potential cathode material with quasi-one-dimensional Li^+ conducting path along the b axis.

ARPES measurements were performed at the UVSOR-III BL5U. Inter-plane ARPES data were acquired at the normal emission angle (θ = 0°) with using hν = 40 - 64 eV at room temperature. To minimize charging effect, we have evaporated K onto the side of sample before cleaving. Single crystals were cleaved in situ along (100) plane.

Figure 1(b) shows photon-energy dependent ARPES spectra of $LiMnPO_4$. For comparison, the density of states (DOS) of $LiMnPO_4$ calculated using density functional theory (DFT) is displayed in Fig. 1(a). From Fig.1(b), we have found that the ARPES peaks show broad dispersive features near the valence band maximum (VBM) around 4 eV and at the band bottom around 10 eV, corresponding to *hν*=62 eV and 50 eV, respectively. It should be noted that K 3p core level around 18.3 eV has not been observed at the cleaved surface, which is suggestive of negligible contribution of evaporated K at the measured spectra.

To show the dispersive features clearly, inter-plane ARPES image along ΓX line of $LiMnPO_4$ is indicated in Fig. 2(a), comparing with DFT calculation (Fig. 2(b)). From the observed symmetry around VBM, the inner potential V_0 is estimated to be 5 eV. Though the complicated dispersive features of Mn 3d-O 2sp hybridized bands have only roughly been observed on the present ARPES results, we expect there are apparent consistency between DFT and ARPES in terms of band gap size (~ 4 eV) and VB width (~ 8 eV). These results suggest the potential utility of ARPES for investigating the electronic structure of cathode material for lithium-ion battery.

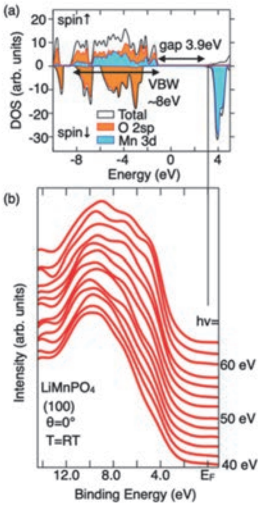

Fig. 1. (a) Density of states of $LiMnPO_4$ [3]. (b) Inter-plane ARPES spectra (θ = 0°) of $LiMnPO_4$.

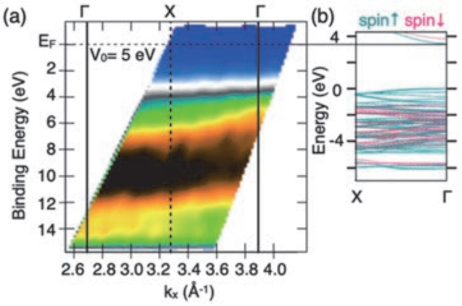

Fig. 2. (a) ARPES image along ΓX line of $LiMnPO_4$. (b) DFT calculations of $LiMnPO_4$ [4].

[1] K. Hikima *et al.*, Commn. Chem. **5** (2022) 52.
[2] K. N. Wood *et al.*, Nature Commun. **9** (2018) 2490.
[3] M. Sgroi *et al.*, Batteries **3** (2017) 11.
[4] The Materials Project. *Materials Data on LiMnPO4 by Materials Project.* United States: N. p., 2020. Web. doi:10.17188/1193777.

BL5U

High-Resolution ARPES of Heavily Overdoped Bi2201 for Evaluation of Coupling Parameters

Y. Miyai[1], S. Ideta[1,2], T. Kurosawa[3], M. Oda[4], M. Arita[2], K. Tanaka[5] and K. Shimada[1,2]
[1]*Graduate School of Advanced Science and Engineering, Hiroshima University,*
Higashi-Hiroshima 739-0046, Japan.
[2]*Hiroshima Research Institute for Synchrotron Radiation Science (HiSOR), Hiroshima University,*
Higashi-Hiroshima 739-0046, Japan
[3]*Faculty of Science and Engineering, Muroran Institute of Technology, Muroran 050-8585, Japan*
[4]*Department of Physics, Hokkaido University, Sapporo 060-0809, Japan*
[5]*UVSOR Synchrotron Radiation Facility, Institute for Molecular Science, Okazaki 444-8585, Japan*

High transition-temperature (T_c) cuprate superconductors have attracted much interest since their discovery. While there have been extensive studies, there exist unsettled physical phenomena such as bad metal, density waves, magnetic fluctuations, and nematic phases [1-4]. These states are emergent from the competing charge, spin and lattice degrees of freedoms. To understand the origin of the physical properties of cuprates, it is desirable to disentangle these competing interactions and quantify each contribution. To this end, here we focus on the Bi-based high-T_c cuprate, $(\mathrm{Bi,Pb})_2\mathrm{Sr}_2\mathrm{CuO}_{6+\delta}$ (Bi2201). The Fermi surface of Bi2201 is relatively simple because there exists a single CuO_2 layer in the unit cell. In this study, we start from the overdoped region, where the electronic state is expected to behave as the Fermi Liquid [3]. However, recently, Kurashima *et al.* found a ferromagnetic fluctuation close to the vanishing T_c region, and the ground state properties in this region should be investigated [3]. Previously Meevasana *et al.* have done angle-resolved photoemission spectroscopy (ARPES) and examined the self-energy due to the electron-electron and electron-phonon interactions especially for the heavily overdoped Bi2201 with no superconducting transition [5]. However, each contribution from the electron-phonon (or electron-boson) and electron-electron interactions as a function of hole concentration is still not clearly determined. Our purpose is, therefore, to systematically clarify the evolution of these interactions as a function of hole concentrations.

To quantitatively evaluate the electron-boson interaction and the electron-electron interaction, we have focused on the Bi-based high-T_c cuprate, Pb-Bi2201 and performed high-resolution ARPES at BL5U. The low T_c (~6 K) allows us to evaluate the normal self-energy at low temperature by suppressing the thermal broadening. In addition, the Pb doping suppresses the structural modulations of the BiO layer and hence the superstructure reflections in the ARPES spectra, and therefore, the overdoped sample is expected to behave like metals enable us to extract normal self-energy. We clearly observed a parabolic quasiparticle dispersion in the nodal direction [7]. By applying tight-binding (TB) model, and we found that the evaluated real part of the self-energy crosses the zero point around $\omega \sim -0.6$ eV, where the imaginary part of the self-energy takes the minimum. The self-energy part responsible for the high-energy anomaly (HEA) is almost temperature independent and the coupling parameter is $\lambda_{\mathrm{HEA}} \sim 1$ at 300 K, indicating strongly correlated nature of the strange metal state. We have also measured fine details near the Fermi level using the μ-Laser ARPES machine and have observed a clear kink structure around -90 meV. From this experiment, we found that, the self-energy part responsible for the low-energy kink (LEK) near the Fermi level shows significant temperature dependence: it is $\lambda_{\mathrm{LEK}} \sim 0.1$ at 300 K but enhances steeply below ~150 K up to $\lambda_{\mathrm{LEK}} \sim 0.8$, leading to the total coupling strength of $\lambda_{\mathrm{tot}} = \lambda_{\mathrm{HEA}} + \lambda_{\mathrm{LEK}} = 1.8$ at 20 K.

In this study, we evaluated the self-energy due to the electron-phonon and electron-electron interactions using the two band TB model. Comparing the theoretical results, the high-energy anomaly is considered to originate from local excitations that are characterized by spin fluctuation or charge fluctuation. Our results clearly indicate distinct energy scales in the self-energy, providing insight into the strange metal state as well as the temperature-dependent interactions of many-body interactions. The details of this study have been published in Ref. [6].

[1] P. Choubey *et al.*, PNAS, **117** (2020) 14805.
[2] Y.Y. Peng *et al.*, Nature Materials **17** (2018) 697.
[3] K. Kurashima *et al.*, Physical Review Letters **121** (2018) 057002.
[4] N. Auvray *et al.*, Nature Communications **10** (2019) 5209.
[5] W. Meevasana *et al.*, Physical Review B **75** (2007) 0174506.
[6] Y. Miyai *et al.*, Phys. Rev. Research **7** (2025) L012039.

BL5U

Electronic Structure Modulation in the CDW Phase of Kagome Superconductor AV_3Sb_5 Studied by ARPES

K. Nakayama[1], S. Suzuki[1], T. Kato[2], Y. Li[3,4,5], Z. Wang[3,4,5], S. Souma[2,6], K. Tanaka[7,8],
T. Takahashi[1], Y. Yao[3,4] and T. Sato[1,2,6,9,10]
[1]*Department of Physics, Graduate School of Science, Tohoku University, Sendai 980-8578, Japan*
[2]*Advanced Institute for Materials Research (WPI-AIMR), Tohoku University, Sendai 980-8577, Japan*
[3]*Centre for Quantum Physics, Key Laboratory of Advanced Optoelectronic Quantum Architecture and Measurement (MOE), School of Physics, Beijing Institute of Technology, Beijing 100081, P. R. China*
[4]*Beijing Key Lab of Nanophotonics and Ultrafine Optoelectronic Systems, Beijing Institute of Technology, Beijing 100081, P. R. China*
[5]*Material Science Center, Yangtze Delta Region Academy of Beijing Institute of Technology, Jiaxing 314011, P. R. China*
[6]*Center for Science and Innovation in Spintronics (CSIS), Tohoku University, Sendai 980-8577, Japan*
[7]*UVSOR Synchrotron Facility, Institute for Molecular Science, Okazaki 444-8585, Japan*
[8]*School of Physical Sciences, The Graduate University for Advanced Studies (SOKENDAI), Okazaki 444-8585, Japan*
[9]*International Center for Synchrotron Radiation Innovation Smart (SRIS), Tohoku University, Sendai 980-8577, Japan*
[10]*Mathematical Science Center for Co-creative Society (MathCCS), Tohoku University, Sendai 980-8578, Japan*

The kagome lattice provides a rich platform for the exploration of unconventional quantum phenomena, including Weyl semimetals, chiral density-wave orders, fractional charges, and exotic superconductivity. These arise from the interplay of electron correlation effects with unique electronic band features like flat bands, Dirac cones, and van Hove singularities. The recently discovered materials AV_3Sb_5 (A: an alkali metal), characterized by vanadium atoms forming an ideal two-dimensional kagome network, offer a valuable opportunity to explore novel physics within the kagome lattice structure [1].

AV_3Sb_5 exhibits the charge-density wave (CDW) state defined by three-dimensional lattice distortions with a periodicity of 2 × 2 × 2 or 2 × 2 × 4, depending on the A element. The CDW transition temperature, T_{CDW}, varies according to the alkali metal, ranging from 78 K to 103 K. Within this CDW phase, AV_3Sb_5 materials often display a breaking of not only translational symmetry but also rotational symmetry. The latter phenomenon suggests the emergence of nematic states, which have occasionally been identified in strongly correlated electron systems, such as cuprates and iron-based superconductors. To verify this nematicity and elucidate its origin, a detailed investigation of the electronic band structure is essential.

In this study, we have performed high-resolution angle-resolved photoemission spectroscopy (ARPES) measurements of a series of AV_3Sb_5 (A = K, Rb, and Cs). High-resolution ARPES measurements were performed at BL5U with linearly polarized photons of 90-150 eV.

Figure 1 shows a representative band dispersion measured in the CDW state of KV_3Sb_5. Compared to the normal state, we observed doubling of some energy bands, which indicates CDW-induced electronic reconstruction [2,3]. We performed first-principles band calculations to understand the observed band doubling and found it originates from the formation of staggrred three-dimensional CDW order. This CDW state naturally breaks rotational symmetry, resulting in nematic-like responses. To amplify the nematic-like response, we developed uniaxial strain device compatible with ARPES, and studied impact of uniaxial strain on the electronic structure.

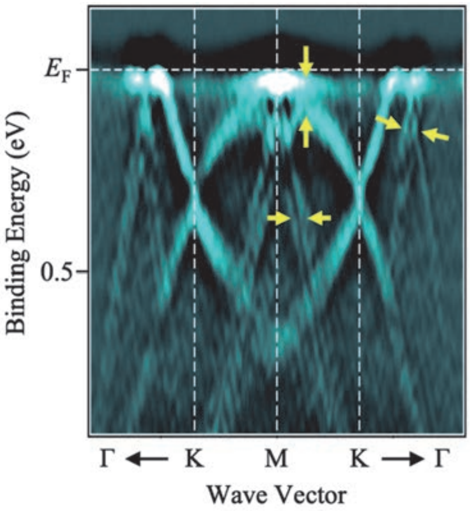

Fig. 1. Second-derivative ARPES intensity plot measured in the CDW state in KV_3Sb_5.

[1] Y. Zhong, J.-X. Yin and K. Nakayama, J. Phys. Soc. Jpn. **93** (2024) 111001.
[2] K. Nakayama *et al.*, Phys. Rev. B **104** (2021) L161112.
[3] T. Kato *et al.*, Commun. Mater. **3** (2022) 30.

BL5U

Explorations of Bandgap-Tuned Excitonic Insulator Materials by Angle-Resolved Photoemission Spectroscopy

K. Fukutani[1,2], R. Nakazawa[1], S. Makita[1], K. Tanaka[1,2] and S. Kera[1,2,3]
[1]*Institute for Molecular Science, Okazaki 444-8585, Japan*
[2]*School of Physical Sciences, The Graduate University for Advanced Studies, Okazaki 444-8585, Japan*
[3]*Graduate School of Science and Engineering, Chiba University, Chiba 263-8522, Japan*

An exciton, a bound pair of an electron and a hole, is one of the most fundamental quasiparticles in condensed matters, which forms as a result of external excitations, such as light irradiations, and plays a pivotal role not only in various electronic devices, including photovoltaic cells and light-emitting diodes, but also in biological processes like photosynthesis.

On the other hand, it is interesting to point out that in the most naïve picture, the negatively charged electrons and positively charged holes would naturally attract each other, and one may expect their bound state (excitons) to be stable in the ground state of matters. Of course, this view is, generally speaking, incorrect in that excitons would *not* form spontaneously in most materials. This is, roughly speaking, due to the effect of electrostatic screening arising from the sea of charged particles, which needs to be properly accounted for when the many-body ground state is to be determined. As it turns out, for most materials, the effect of screening is strong enough to make the binding of electrons and holes energetically more expensive than when they remain separated.

Extending along the line of thought mentioned above, an interesting question can be proposed; that is, what if we tune the bandgap of materials so as to decrease the density of carriers (i.e., source of screening) across the limit where the simple electron- hole Coulomb attraction can overcome the "barriers" of carrier screening? This question is pondered by N. F. Mott, W. Kohn, D. Jerome and others, and have led to the theoretical prediction of what is called an *excitonic insulator* (EI) [1], in which the simple Coulomb attraction between the electrons and holes manifests itself as they form a condensate of excitons in the many-body ground state.

While the charge neutrality of excitons and the lack of distinct macroscopic behaviors like superfluidity had made it difficult for the experimental probes to unambiguously detect the EI phase, various prominent candidate materials exist, such as Ta_2NiSe_5 and $TiSe_2$. In particular, $TiSe_2$ has been proposed as an EI material nearly two decades ago [2] and have been extensively investigated by various experimental probes. Nonetheless, due to the presence of both the exciton and the phonon degrees of freedom, which are closely interlinked near the quantum criticality, its true nature is still under disputes and a general consensus has not been reached.

Thus, we once again trace back to the original question of how the bulk carrier density (closely linked to the magnitude of bandgap) affects the competition between the electron-hole Coulomb attraction and the carrier screening. In our experiments, we have performed the photon-energy- and polarization-dependent angle-resolved photoemission spectroscopy (ARPES) on $Ti(Se_{1-x}Te_x)_2$, to observe the evolution of their 3D band structures. As shown in Fig. 1, the negative bandgap is clearly enhanced as the Te-doping x increases from 0 to 0.5 and at the same time, the charge density wave, believed to be accompanied by the EI transition, is confirmed to be suppressed down to T = 5 K. Further investigations on various Te-doping concentrations are expected to provide important insights into one of the fundamental questions in many-body condensed matter physics.

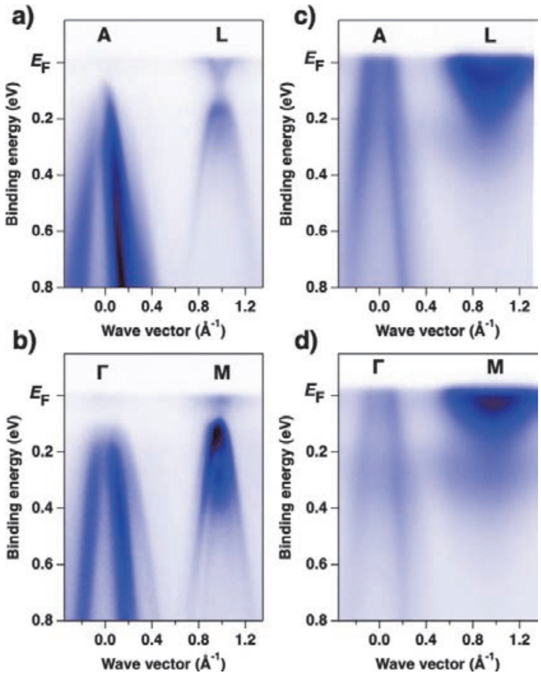

Fig. 1. ARPES intensity plots for $TiSe_2$ (x = 0) taken at (a) $h\nu$ = 44 eV, (b) $h\nu$ = 58 eV and TiSeTe (x = 0.5) taken at (c) $h\nu$ = 44 eV, (d) $h\nu$ = 58 eV near the indicated high-symmetry lines of bulk Brillouin zones at T = 10 K.

[1] D. Jerome *et al*., Phys. Rev. **158** (1967) 462 etc.
[2] H. Cercellier *et al*., Phys. Rev. Lett. **99** (2007) 146403 etc.

BL5U

Relation between Electronic Structure and Thermopower in $YbCu_2Si_2$

D. Goto[1], S. Uchida[1], M. Matsunami[1,2,3] and T. Takeuchi[1,2,3]
[1]*Toyota Technological Institute, Nagoya 468-8511, Japan*
[2]*Research Center for Smart Energy Technology, Toyota Technological Institute, Nagoya 468-8511, Japan*
[3]*MIRAI, Japan Science and Technology Agency, Tokyo 102-0076, Japan*

Thermoelectric technology, which is capable of converting temperature differentials directly into electrical energy, can maximize the efficient use of existing energy sources. However, thermoelectric generation has not been widely applied in our society due to its energy conversion inefficiency. As evaluation criteria for the efficiency, the dimensionless figure of merit $ZT = S^2T/\rho\kappa$ or the power factor $PF = S^2/\rho$ where S, ρ, and κ are the Seebeck coefficient, electrical resistivity, and thermal conductivity, respectively, of constituent materials, are well known. It is necessary to search for materials possessing large ZT or PF.

It is known that in heavy fermion systems, the low ρ and large $|S|$ coexist, resulting in a large PF. This can be caused by the characteristic electronic structure formed by the hybridization between conduction and f electrons. However, there is a serious problem concerning the sign of S, which cannot be determined solely in terms of the energy dependence of the electron density of states as in most simple metals. Therefore, the energy dependence of the relaxation time of quasiparticles, both which are the terms in Mott formula and are neglected in many cases, should be taken into account.

The main purpose of this research is to establish a methodology for experimentally evaluating the energy dependence of the relaxation time of quasiparticles in the vicinity of the Fermi level (E_F) using angle-resolved photoemission spectroscopy (ARPES). In this study, we focus on the typical heavy fermion system $YbCu_2Si_2$, which is known to show relatively high large $|S|$ [1].

Single crystals of $YbCu_2Si_2$ were prepared by the Sn-flux method. The elements, Yb (3N) Cu (4N), Si (5N), and Sn (3N), with an off-stoichiometric ratio of Yb : Cu : Si : Sn = 1 : 15 : 2 : 50 were inserted in an alumina crucible and sealed in a quartz tube. The quartz tube was heated to 1050 °C, maintained at this temperature for two days, and cooled to 600 °C at the rate of 2 °C/h, taking about 12 days in total. The excess flux was removed using a centrifuge outside the furnace. Synchrotron ARPES measurements were carried out at the undulator beamline BL5U of UVSOR facility in the Institute for Molecular Science, using photon energies of 40 eV - 121 eV and a hemispherical electron analyzer, MBS-A1. The total energy resolution was set to 21 meV for a photon energy of 40 eV. The clean (001) surface of single crystals was obtained by *in-situ* cleaving under ultra-high vacuum condition. The Fermi level was determined by measuring a polycrystalline gold film in electrical contact with the samples.

The inset of Fig. 1 shows the Brillouin zone of $YbCu_2Si_2$. In the present study, the ARPES image is measured along the directions from Γ to X or from Z to X in the neighboring Brillouin zone corresponding to the $\bar{\Gamma}$-$\bar{X}$ direction in the surface Brillouin zone. Figure 1 shows the Fermi surface measured with a photon energy of 40 eV. According to the band calculation (LDA + U) [1], $YbCu_2Si_2$ has at least two Fermi surfaces, in which one is due to quasi two-dimensional (33th) electron band centered at X point focused in the present study and the other is due to three-dimensional (32th) hole band around Z point. By analyzing these bands, we will further investigate the relation between the electronic structure and Seebeck coefficient in $YbCu_2Si_2$.

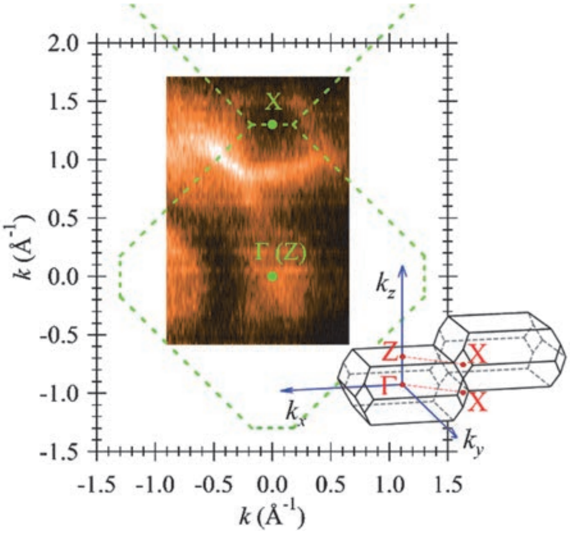

Fig. 1. (a) ARPES image of $YbCu_2Si_2$ along $\bar{\Gamma}$-$\bar{X}$ direction at 9 K measured with the photon energy of 121 eV.

[1] N.D. Dung *et al.*, J. Phys. Soc. Jpn. **78** (2009) 084711.
[2] M. Matsunami *et al.*, Phys. Rev. B **87** (2013) 165141.

BL5U

Electronic Structure Study on Novel Spin-Split Collinear Antiferromagnets

Z. Lin[1], X. Liang[1] and J. Ma[1]
[1]*Department of Physics, City University of Hong Kong, Kowloon, Hong Kong, China*

Magnetism, a foundational domain in condensed matter physics, conventionally classifies magnetic materials into two primary phases: ferromagnets and antiferromagnets (although unconventional forms like ferrimagnetism and chiralmagnetism are also recognized). Ferromagnets exhibit macroscopic magnetization in spatial space and spin splitting in reciprocal momentum space.

Conversely, typical antiferromagnets show no net macroscopic magnetization in spatial space and no spin splitting in reciprocal momentum space when time reversal symmetry combined with inversion or translation operation is preserved [1–3]. Recent theoretical investigations have identified special collinear antiferromagnetic materials with substantial spin-split band structures but no net macroscopic magnetization. This has led to the proposal of altermagnetism, a special antiferromagnetic phase that appropriately describes such materials. In contrast to conventional antiferromagnets, which have spin sublattices linked to one another through straightforward translation operations, altermagnetism involves linking sublattices with opposite spins using rotation operations. Applying the same rotational angle in momentum space causes a spin flip between up and down. As outcome of this phenomenon, even-order wave symmetries of the spin pattern appear, such as the d-, g-, and i-waves. Recently, it has even been suggested that altermagnetism can extend to include non-collinear spins and multiple local-structure variations.

In this study, we focus on d-wave altermagnet candidate RuO_2 and g-wave altermagnet candidate CrSb. We have carried out high-resolution spin angle-resolved photoemission spectroscopy (ARPES) measurements of RuO_2 and CrSb by using MBS-A1 spectrometer and customized VLEED spin detector at BL5U.

Figure 1 and 2 shows the spin ARPES result of this beamtime. Figure 1 shows that RuO_2's spin texture is symmetric about the Γ point, which conflicts with the presented result [4]. The result in Fig.1 indicates that the spin texture of RuO_2 is not from space-inversion symmetry breaking. Figure 2 shows the possible spin splitting band structure of CrSb.

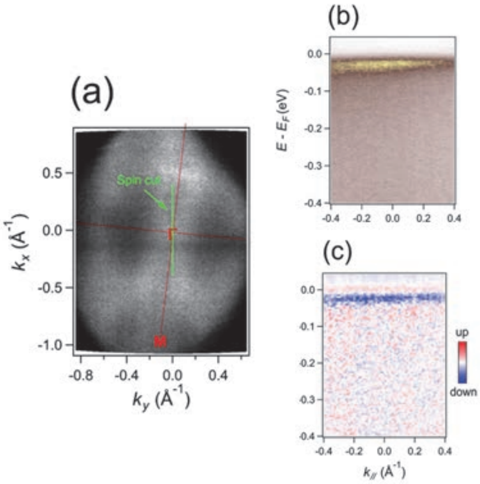

Fig. 1. (a), Fermi Surface of RuO_2. (b), The ARPES band structure of the green line in Fig. 1(a). (c), The spin resolved data of the same path band structure as (b).

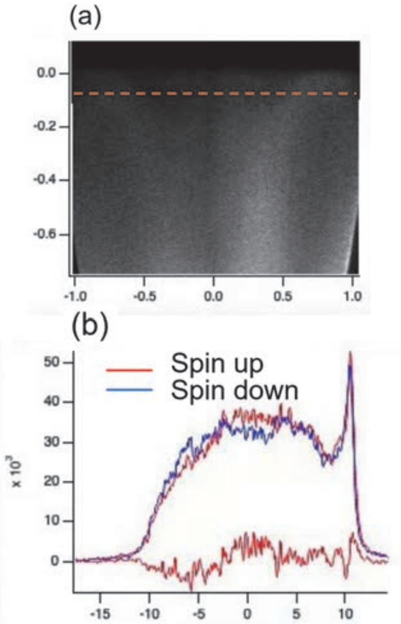

Fig. 2. (a), a high-symmetric path's band structure of CrSb. (b), The spin resolved MDC of the orange line of figure 2(a).

[1] L. Néel, Science **174** (1971) 985.
[2] L. Šmejkal, J. Sinova, and T. Jungwirth, Phys. Rev. X **12** (2022) 031042.
[3] L. Šmejkal, J. Sinova, and T. Jungwirth, Phys. Rev. X **12** (2022) 040501.
[4] J. Liu *et al*., Phys. Rev. Lett. **133** (2024) 176401.

BL5U

Photoemission Study about the Fermi Arc in Type-II Weyl Semimetal NbIrTe$_4$

S. Cho[1] and D. Shen[2]

[1]Department of Physics Education, Sunchon National University, Suncheon57922, Republic of Korea

[2]National Synchrotron Radiation Laboratory, University of Science and Technology of China, Hefei 230026, China

The unique features of topological Weyl semimetals (TWSs) arise primarily from their unusual band structure around the Weyl nodes and the topologically non-trivial surface state as Fermi arc, which connect each pair of Weyl nodes [1]. Moreover, TWSs have a family so-called type-II TWSs, where the Weyl nodes are highly anisotropic and tilted, breaking the Lorentz symmetry [2]. The Weyl nodes of type-II TWSs appear as contact points between electron and hole pocket in the bulk band structure, which result in the presence of the boundaries between these pockets. One of the promising candidates for type-II TWSs is WTe$_2$, which has the orthorhombic crystal structure with space group $Pmn2_1$ and the bulk system of WTe$_2$ exhibits the non-saturating magnetoresistance [2].

Recently, NbIrTe$_4$ and TaIrTe$_4$, which crystallize in the non-centrosymmetric orthorhombic space group $Pmn2_1$ (No. 31), have been suggested as possible type-II TWSs. The previous calculation result of NbIrTe$_4$ revealed a closed Fermi arc loop that connects two distinct pairs of Weyl nodes from the top and bottom surfaces in the type-II TWSs [3]. Given the symmetry of TaIrTe$_4$ (presence of time-reversal symmetry but with broken inversion symmetry) and the Berry curvature originating from its type-II Weyl nodes, TaIrTe$_4$ can expect to exhibit a large and room-temperature nonlinear Hall effect [4]. Moreover, the recent scanning tunneling microscopy results of TaIrTe$_4$ show a superconducting gap below a critical temperature 1.54 K [5]. The behavior of the normalized upper critical field and the stability of the superconductivity against the ferromagnetism suggest the unconventional superconductivity with the p-wave pairing. The results of the scanning tunneling spectroscopy and angular-dependent transport measurements show that the superconductivity is the quasi-1D and occurs in the surface states [5].

Here, we investigate the spin structure of the Fermi arc associated with the type-II Weyl nodes in NbIrTe$_4$. Given the lack of inversion symmetry, NbIrTe$_4$ is predicted to host four type-II Weyl nodes. In previous band calculation, one of these type-II Weyl points was found to show an intersection of tilted cone which lies on the Fermi energy at $E - E_F = 0.131$ eV. The electronic structure of NbIrTe$_4$ shows the different surface state at two different surface terminations (top and bottom surface in Fig. 1a), leading to distinct Fermi arc loop configuration. This is because the Fermi arc loop connects different pairs of the Weyl nodes depending on the surface termination.

Figure 1 (b) and (c) show the Fermi surface and the band structure at $k_y = 0$ (red dotted line in Fig. 1b) taken from the bottom surface termination. The Fermi arc exists near the Γ-point, consistent with the previous band calculation results in Ref. [3]. We try to measure the spin structure of the Fermi arc in Fig. 1 (d). Figure 1 (d) shows the spin-resolved momentum distribution curves (MDC) and spin polarization of the Fermi arc at EB = -0.01 eV. We found that the spin polarization taken from the left and right momentum points show opposite direction of s_y with red and blue assigned for spin-down and spin-up respectively. We hope our results on the spin-resolved MDC may provide valuable insights into the characteristics of type-II Weyl nodes.

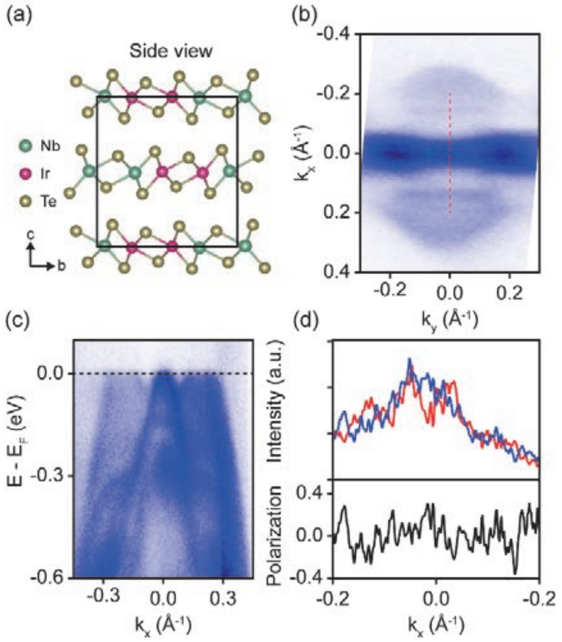

Fig. 1. (a) Crystal structure of NrIrTe$_4$ (b) The Fermi surface obtained from the bottom surface termination. (c) The band structure at the red line in b. (d) spin-resolved MDC along the s_y direction and the spin polarization at $E_B = -0.01$ eV.

[1] A. Bansil, H. Lin, and T. Das, Rev. Mod. Phys. **88** (2016) 021004.
[2] A. A. Soluyanov *et al.*, Nature **527** (2015) 495.
[3] S. A. Ekahana *et al.*, Phys. Rev. B **102** (2020) 085126.
[4] D. Kumar *et al.*, Nat. Nanotechnol. **16** (2021) 421.
[5] Y. Xing *et al.*, Natl. Sci. Rev. **7** (2020) 579.

BL6U

Accurate 2D-Momentum-Microscopy-Data Distortion Correction Method for Characterization of Valence Band Spin Polarization

F. Matsui[1,2], Y. Sato[1,2], K. Hagiwara[1], S. Tanaka[3] and S. Suga[3]
[1]UVSOR Synchrotron Facility, Institute for Molecular Science, Okazaki 444-8585, Japan
[2]The Graduate University for Advanced Studies (SOKENDAI), Okazaki 444-8585, Japan
[3]SANKEN, The University of Osaka, Ibaraki 567-0047, Japan

Combining a two-dimensional (2D) spin filter with a photoelectron momentum microscope (PMM) allows multi-channel detection of spin polarization data in 2D momentum and real spaces. An established method for spin polarization analysis is to measure the difference between two patterns taken at the different scattering energies corresponding to the opposite spin-dependent reflectivity [1]. On the other hand, the PMM installed at BL6U in UVSOR [2] is equipped with a spin rotator that flips the direction of the in-plane spin component by ±90°. In addition to the conventional method of taking the scattering energy dependence, the spin rotator makes it possible to detect the spin polarization pattern using a single-scattering-energy condition [3]. The spin rotator can alternate between positive and negative spin polarization detection in times less than one second, opening the door to the efficient accumulation of multi-dimensional (*kz* dispersion, position scan, time evolution, photon polarization, etc.) spin-polarized spectral data. The drawback is that the spin components rotate by ±90° due to Larmor precession in the spin rotator, and the 2D projection distributions also rotate by ±45° due to the Lorentz force simultaneously. To obtain a differential pattern of the 2D distribution of positive and negative spins, the coordinates of the two ±45° rotated patterns must be precisely rotated back to their original orientation to eliminate aberration and distortion.

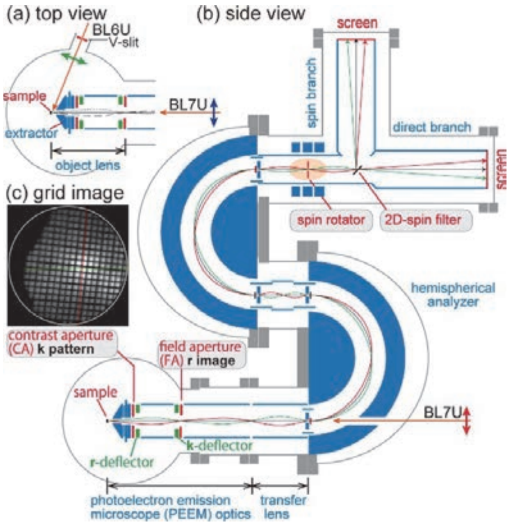

Fig. 1. (a) Top and (b) side views of the photoelectron momentum microscope. (c) The grid inserted at the location of the CA imaged by the direct branch screen.

The PMM at BL6U consists of a six-axes sample stage, PEEM optics, two concentric hemispherical analyzers, a spin rotator, a 2D spin filter, and 2D projection-type detectors in direct and spin-resolved branches as shown in Fig. 1(a) and (b). Instead of a contrast aperture and a field aperture, square grids that can be inserted in the diffraction and back focal planes, respectively, are used to correct distortions of the 2D pattern on the final detection screen. Figure 1(c) shows the image of such a grid on a direct branch screen inserted at the contrast aperture position. Note that the grid is intentionally rotated approximately 5° counter-clockwise to be offset from the pixel array of the CMOS detector.

Figure 2(a) and (b) show images of the CA grid using the ±45° rotation modes of the spin rotator by the direct branch. The latter image is rotated -90° with respect to the former. Figures 2(c) and (d) show the images after numerical correction of coordinate rotation and distortion. As shown in Fig. 2(e) and (f), the horizontal and vertical intensity profiles of the two images (blue: +45°, red: -45° rotation mode) match exactly. Since the spin rotator only affects the photoelectron trajectory after they leave the second hemispherical analyzer, the positional relationship between the valence band pattern and the grid image is not affected. Based on this correction procedure, two spin polarized images are aligned exactly the same coordinates and the spin-polarized valence band dispersion and Fermi surface data are analyzed [3].

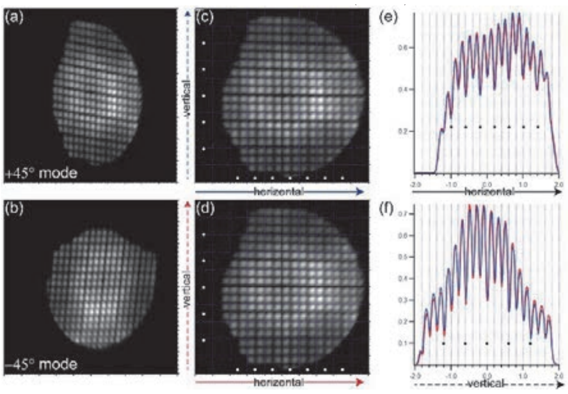

Fig. 2. (a, b) Raw and (c, d) coordinate-corrected grid images of the spin rotator ±45° modes. (e, f) Intensity profiles along the horizontal and vertical directions.

[1] C. Tusche *et al.*, Ultramicroscopy **159** (2015) 520.
[2] F. Matsui *et al.*, J. Phys. Soc. Jpn. **59** (2020) 067001.
[3] F. Matsui *et al.*, submitted (2025).

BL6U

Steady Development of the SP-PMM at UVSOR BL6U with Reliable Data Acquisition and Very High Efficiency

S. Suga[1]

[1]*SANKEN, Osaka University, Mihogaoka, Ibaraki, Osaka 567-0047, Japan*

In order to overcome various and serious difficulty of the single channel spin-resolved-ARPES (SP-ARPES) detection by use of a single hemispherical electron energy analyzer, much more reliable and orders of magnitude higher detection efficiency spin-resolved Photoelectron Momentum Microscope (SP-PMM) with double hemispherical electron energy analyzers (DHDAs) and PEEM type objective lens as well as two dimensional spin detector (SP-PMM) was introduced to UVSOR in 2022.

Two dimensional(2D) real space $E_B(x, y)$ is first measured with changing the sample position and the high quality homogeneous (x, y) regions (even down to 10μm) are selected. Then objective lens mode is switched to the $E_B(k_x, k_y)$ mode and their 2D patterns beyond the 1st Brillouin zone of most materials are recorded at various E_B with 2D detector without sample movement (Fig.1). Even in the case of multidomain cleaved surfaces, PEEM can select a certain particular domain region with the size larger than ~10μm. Then $E_B(k_x, k_y)$ series are integrated as functions of hν. The spatial resolution is decided by the PEEM aperture as good as 50nm. Temperature dependent PMM is feasible down to 10 K now in UVSOR BL6U. The measurements have so far been performed on variety of samples [1-3]. Since the selection rule must be taken into account for understanding several experimental results, we also realized the feasibility of the normal incidence excitation from the branched line of BL7U as shown partly in Publications.

For the spin measurement, Ir(001) clean surface has been so far utilized. This spin filter was used at around 30 eV photoelectron collision with the Ir of the life time of less than 1 day, by use of the spin rotator. Since the tuning of the collision energy down to 10eV became feasible recently after solving an instrumental problem, we will soon start the Au monolayer covered Ir spin filter in few months. Its life time is already checked to be several months. Then we will perform most experiments by this performance-upgraded SP-PMM on the materials under various hot discussions.

So far we have measured the samples with the clean surface prepared either 1) by ion sputtering and annealing or 2) cleaved by peeling off tapes. The 3) pin post pressed cleavage was also employed for wide variety of samples. In addition, the knife-edge cleavage is required for hard materials. So I designed 4) a cleavage crystal recovering box with the knife edge on it. Further the 5) flexibly adjustable knife edge cleavage system is planned to be added in the near future for much more sample cleavage.

In addition, I am preparing an operation manual to use the complex SP-PMM in UVSOR in English, since the demand from the foreign users are expected to increase dramatically in 2025 after the perfect performance of the Au/Ir(001) spin filter, and the use of flexible cleavage system.

Since the normal incidence synchrotron radiation use is very limited, I hope to introduce switchable low energy laser with variable light polarization to be set in the normal incidence configuration. If the pulsed laser is set pump-probe SP-PMM may become feasible.

The collaboration have been so far performed with the research members Prof. F. Matsui, Prof. S. Kera, Dr. Y. Sato, Dr. R. Sagehashi, Dr. K. Hagiwara in UVSOR, IMS & Prof. S. Tanaka, SANKEN, Osaka Univ. I hope to contribute to future works for the next 20 years.

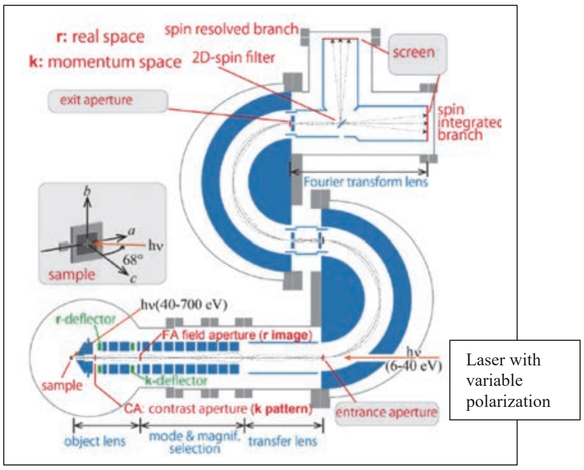

Laser with variable polarization

Target is to realize the best resolutions in x, y, k_x, k_y, k_z, Spin (Psx, Psy, Psz) from VUV to Hard X-ray region. Operand measurements are also planned. Spin rotator is in work.

Related-Publication

[1] F. Matsui, K. Hagiwara, E. Nakamura, T. Yano, H. Matsuda, Y. Okano, S. Kera, E. Hashimoto, S. Koh, K. Ueno, T. Kobayashi, E. Iwamoto, K. Sakamoto, S. Tanaka and S. Suga Rev. Sci. Instrum. **94** (2023) 083701.

[2] F. Matsui, K. Hagiwara, Y. Sato, E. Nakamura, R. Sagehashi, S. Kera and S. Suga, Synchrotron Rad. News, **37** (2024).

[3] Y. Higuchi, R. Itaya, H. Saito, T. Toichi, T. Kobayashi, M. Tomita, S. Terakawa, K. Suzuki, K. Kuroda, T. Kotani, F. Matsui, S. Suga, H. Sato, K. Sato and K. Sakamoto, Vacuum, **233** (2025) 113944.

BL6U

Three-Dimensional Fermi Surface Measurement of the Au Crystal Via the Photon-Energy-Dependent Angle-Resolved Photoelectron Spectroscopy Using the Photoelectron Momentum Microscope

S. Tanaka[1], S. Suga[1], K. Hagiwara[2], Y. Sato[2] and F. Matsui[2]
[1]*SANKEN, The University of Osaka, Mihogaoka 8-1, Ibaraki 567-0047, Japan*
[2]*UVSOR Synchrotron Facility, Institute for Molecular Science, Okazaki 444-8585, Japan*

The Fermi surface is a fundamental concept in solid-state physics, representing the boundary in momentum space that separates occupied from unoccupied electronic states. While much progress has been made in understanding the 2D Fermi surface by the angle-resolved photoelectron spectroscopy (ARPES) for materials like thin films or surfaces, obtaining the full 3D Fermi surface has remained a significant challenge, due in part to the complexity of the experimental techniques involved and the immense volume of data required to map the surface in three dimensions.

The dual-beamline photoelectron momentum microscope (PMM) developed at UVSOR is a powerful tool not only for comprehensively characterizing orbital contributions in the electronic structure, but also for determining the Fermi surface, thanks to its high efficiency and extensive momentum-space detection range [1,2]. In recent years, we have been developing methods for 3D Fermi surface determination, both experimentally and through computer-based analyses.

Figure 1 presents the photoelectron intensity maps obtained with the measurements using the PMM for the Au(111) surface, which correspond to the Fermi surface in various planes within the reciprocal lattice space of the Au crystal. Panel (a) shows the k_x–k_y plane at the indicated k_z values, while panels (b) and (c) depict k_y–k_z and k_x-k_z planes at k_x=0 and k_y=0, respectively. The k_z values were estimated using the free-electron final-state model, as

$$k_z = \sqrt{\frac{2m_e}{\hbar^2}\left(E_k \cos^2\theta + V_0\right)}$$

where E_k and θ are the kinetic energy and the polar emission angle of the photoelectron, respectively. We assumed the inner potential V_0 is 10.5 eV. Photon energies ranging from 45 eV to 100 eV were employed. Because the Au crystal has three-fold symmetry along the <111> axis, all the intensity distributions in Figs. 1 are the results of averaging over three images; the original distribution and those rotated by 120° and 240°; in order to improve statistics and to suppress the effects of photon polarization. It should be noted that generating the 3D volume data (whose cross sections are shown in Figs. 1) from a series of photon-energy–dependent ARPES measurements required the development of specialized data conversion programs using the cutting-edge AI technique.

In Fig. 1(a), small circles with a radius of approximately 0.17 Å⁻¹ around the origin are visible at all k_z values. Additionally, regular hexagons of uniform size, each with an approximate radius of 1 Å⁻¹, are clearly visible in the k_z range of 4.87–4.35 Å⁻¹. As these features do not depend on k_z in terms of their shapes (though their intensity may vary with photon energy), we attribute them to the Au(111) surface states. Other features, which change with k_z, should be attributed to photoelectrons emitted from the bulk 3D-Fermi surface. We are currently developing detailed comparisons between the experimental results and density functional theory (DFT) calculations performed using Quantum Espresso package (version 7.2). While some experimentally observed features are well reproduced by the theoretical calculations, significant discrepancies remain at this stage. Further investigation will be required to refine the methodology for revealing the 3D Fermi surface by exploiting photon-energy–dependent measurements, including the adoption of a more accurate final-state model beyond the free-electron approximation that has been recently proposed [3].

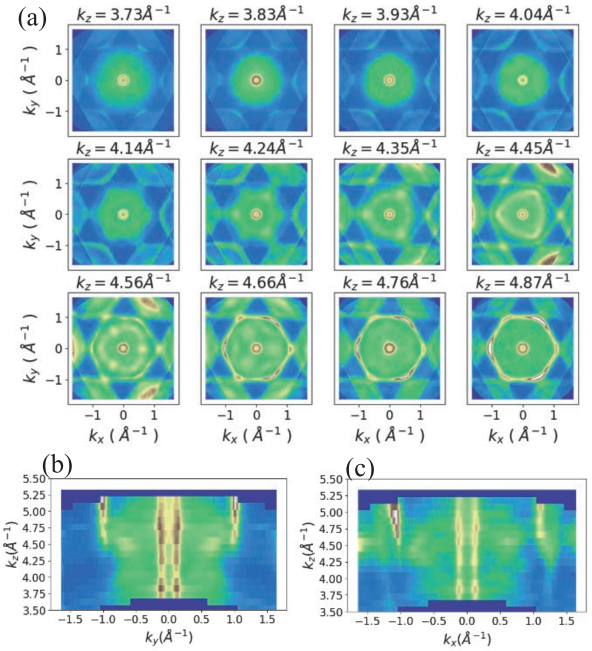

Fig. 1. Photoelectron intensity maps at the Fermi level of Au(111) for various planes in the reciprocal lattice space.

[1] F. Matsui *et al.*, Rev. Sci. Instrum. **94** (2023) 083701.

[2] K. Hagiwara *et al.*, J. Synchrotron Radi. **31** (2024) 540.

[3] V. N. Strocov *et al.*, Nat Commun. **14** (2023) 4827.

BL6U

Photoelectron Momentum Microscopy Study of Termination-Dependent Electronic Structure in PtBi$_2$

Y. Morita[1], K. Nakayama[1], T. Kato[2], S. Souma[2,3], S. Masaki[4], T. Ikushima[4], Y. Moriyasu[4],
K. Hagiwara[5], F. Matsui[5], T. Takahashi[1], K. Kudo[4] and T. Sato[1,2,3,6,7]
[1]*Department of Physics, Tohoku University, Sendai 980-8578, Japan*
[2]*Advanced Institute for Materials Research (WPI-AIMR), Tohoku University, Sendai 980-8577, Japan*
[3]*Center for Science and Innovation in Spintronics (CSIS), Tohoku University, Sendai 980-8577, Japan*
[4]*Department of Physics, Graduate School of Science, Osaka University, Toyonaka 560-0043, Japan*
[5]*UVSOR Synchrotron Facility, Institute for Molecular Science, Okazaki 444-8585, Japan*
[6]*International Center for Synchrotron Radiation Innov1ation Smart (SRIS), Tohoku University,*
Sendai 980-8577, Japan
[7]*Mathematical Science Center for Co-creative Society (MathCCS), Tohoku University, Sendai 980-8578, Japan*

The discovery of exotic quantum phenomena, such as the half-integer quantum Hall effect in graphene and surface Dirac states in topological insulators, has sparked significant interest in condensed matter physics. These effects originate from novel quasiparticles associated with band degeneracies. For instance, graphene hosts two-dimensional Dirac fermions with linear band dispersion that intersect at a single point, because of the chiral symmetry of its honeycomb lattice. In topological insulators, surface conduction is driven by spin-polarized Dirac fermions, which are protected by time-reversal symmetry and nontrivial bulk topology. These findings stimulate research in exploring quasiparticles beyond Dirac fermions. Among these, Weyl fermions, 3D spin-polarized counterparts of Dirac fermions, are notable for their topological stability and unconventional phenomena such as the chiral anomaly and Fermi arc surface states. Weyl fermions can emerge when either spatial inversion or time-reversal symmetry is broken.

Among candidate Weyl semimetals, PtBi$_2$ is particularly intriguing. It consists of Bi-Pt-Bi trilayer sheets which stack along the c axis. One Bi layer is flat and the other is buckled, resulting in an A-B-C stacking sequence that naturally breaks inversion symmetry. This symmetry breaking combined with strong spin-orbit coupling from the heavy atomic masses lifts spin degeneracy in the band structure. DFT calculations predict that PtBi$_2$ hosts twelve Weyl fermions near $k_z = \pm 0.5\ \pi/c$. Moreover, this material exhibits bulk superconductivity at 0.6 K, and recent studies have suggested the existence of surface superconductivity at a significantly higher temperature (~10 K). This makes PtBi$_2$ a rare platform for exploring the interplay between Weyl fermions and superconductivity at relatively high temperatures. Such coupling could trigger the emergence of topological superconductivity with Majorana fermions, which are their own antiparticles.

In this study, we aimed to gain a comprehensive understanding of the surface-termination-dependent fermiology of PtBi$_2$. We performed photoelectron momentum microscopy measurements at BL6U and mapped the band structure over a wide momentum space. The Fermi surfaces observed for different terminations [Figs. 1(a) and 1(b)] show complex features. Spectral components common to both terminations are attributed to bulk states, while the different features are interpreted as surface states. By comparing our data with DFT-based Fermi surface calculations, we identify signatures of Fermi arc surface states, supporting the Weyl semimetal character of PtBi$_2$.

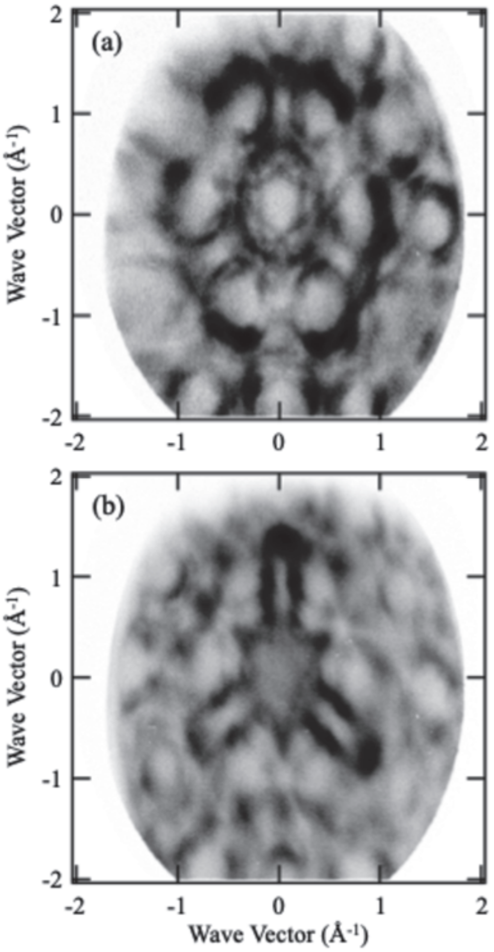

Fig. 1. (a) and (b) Two-dimensional ARPES intensity maps at a constant energy measured on different surface terminations in PtBi$_2$.

BL7U&5U

Changes in the Electronic Structure during the Charge-Density-Wave Transition Via the Well-Defined Temperature-Dependent Angle-Resolved Photoelectron Spectroscopy

S. Tanaka[1], K. Ueno[2] and K. Tanaka[3]
[1]*SANKEN, The University of Osaka, Mihogaoka 8-1, Ibaraki 567-0047, Japan*
[2]*Department of Chemistry, Graduate School of Science and Engineering, Saitama University, Saitama 338-8570, Japan*
[3]*UVSOR Synchrotron Facility, Institute for Molecular Science, Okazaki 444-8585, Japan*

The charge-density-wave (CDW) transition in titanium diselenide ($TiSe_2$) has attracted substantial interest due to its intriguing interplay between structural and electronic properties. Historically, X-ray diffraction studies have established a prominent structural transition near 202K [1], characterized predominantly by displacement of Ti atoms. More recently, advanced diffraction experiments revealed additional diffraction spots emerging at a lower temperature of approximately 165K, attributed primarily to the displacement of Se atoms which coincides with the peak-temperature observed in the resistivity change during the CDW transition [2]. Despite extensive structural investigations, detailed knowledge of how these distinct atomic rearrangements influence the electronic structure across the CDW transition remains incomplete.

In this study, we employ temperature-dependent angle-resolved photoelectron spectroscopy (ARPES) to investigate the electronic structure evolution of $TiSe_2$ across the CDW transition. The left panel of Fig. 1 presents ARPES spectra measured near the Γ point (top panel) and the L point (bottom panel) of $TiSe_2$, both below (left-hand side) and above (right-hand side) the CDW transition temperature. In the non-CDW phase (right-hand side), distinct features in the electronic states in $TiSe_2$ are Se4p-derived valence band and Ti3d conduction band located at the Γ and L points, respectively. The right panel of Fig. 1 displays the photoelectron intensity maps obtained along the momentum-space cuts indicated in the ARPES spectra, as a function of temperature. Our ARPES measurements reveal notable electronic signatures associated with the CDW transition including: (1) the folding of the Ti3d band from the Brillouin zone boundary (L point) toward near the zone center (Γ point), (2) the complementary folding of the Se4p band from near Γ toward the vicinity of the L point, and (3) a distinct binding energy shift of the Se4p band near the Fermi level.

Figure 2 illustrates the temperature dependence of the observed electronic signatures—specifically, the band folding intensity and energy shift—normalized such that values are set to 1 at 25 K and 0 at 200 K. The transition temperature for all the changes in the electronic structure is 165K, not the 202K. These observations indicate that the fundamental electronic reorganization in $TiSe_2$ is closely correlated with the lower-temperature structural transition involving Se atom displacement, rather than the higher-temperature transition predominantly involving Ti atom movements. Our findings clarify the relationship between electronic and structural transformations in $TiSe_2$ and underscore the critical role of Se atoms in driving the electronic properties of the CDW phase.

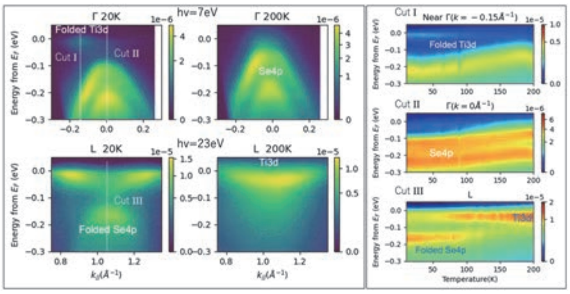

Fig. 1.
Left: the ARPES spectra near the Γ point (upper part) and L point (lower part) of $TiSe_2$ below the CDW temperature (left) and above (right).
Right: The photoelectron intensity map along the cut indicated in the ARPES spectra shown in the left panel as functions of the temperature.

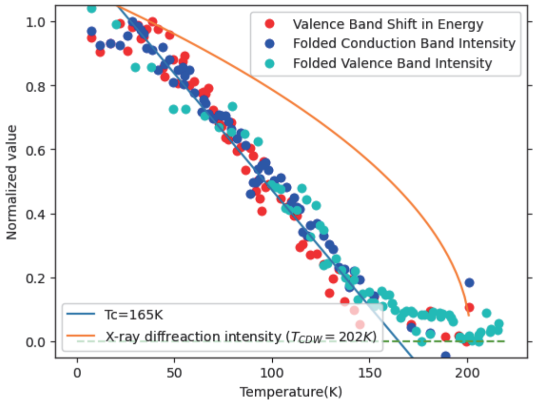

Fig. 2. Temperature dependence of the observed electronic signatures in $TiSe_2$, specifically the band folding intensity and binding energy shift, normalized to unity at 25 K and to zero at 200 K.

[1] F. J. Di Salvo, D. E. Moncton, and J. V. Waszczak, Phys. Rev. B **14** (1976) 4321.
[2] H. Ueda *et al.*, Phys. Rev. Res. **3** (2021) L022003.

BL6U

Momentum-Resolved Resonant Photoelectron Spectroscopy of Au(111) Toward Distinguishing p and d Orbital Contributions

K. Hagiwara[1], R. Sagehashi[1], Y. Sato[1,2], S. Tanaka[3], S. Suga[3] and F. Matsui[1,2]
[1]*UVSOR Synchrotron Facility, Institute for Molecular Science, Okazaki 444-8585, Japan*
[2]*The Graduate University for Advanced Studies (SOKENDAI), Okazaki 444-8585, Japan*
[3]*SANKEN, The University of Osaka, Mihogaoka 8-1, Ibaraki 567-0047, Japan*

Dual-beamline photoelectron momentum microscope (PMM) developed at UVSOR is a powerful tool for comprehensive characterization of orbital contribution to the electronic structure [1, 2]. Normal-incident VUV light from BL7U can be used to analyze atomic orbital symmetry [2]. Resonant photoelectron spectroscopy, utilizing photon-energy (*hν*) tunable soft X-ray from BL6U at specific core absorption edges, can provide element- and/or orbital-selective information [3]. We have determined 6p orbital arrangement in the Fermi surface of Au(111) by using horizontally and vertically polarized light from BL7U [2]. However, 5d orbital contribution to the Fermi surface was reported [4]. Therefore, light polarization dependent measurement distinguishing the p and d orbitals is challenging. Here, we have investigated the 6p and 5d orbital contributions to the Fermi surface of Au(111) by resonant photoelectron spectroscopy. Whether the 5d signal selectively enhanced when excited with the photon energy corresponding to transition from 4f to 5d was our question.

Figure 1 shows the photoemission intensity in the valence band region integrated over all momentum as a function of photon energy. One can find noticeable intensity peaks indicated by two dotted lines. These peak lines originate from the Au $4f_{7/2}$ and $4f_{5/2}$ core levels excited by the second order light. Figures 2(a) and 2(b) show the momentum map at E=E_F-0.2eV excited under the resonant (*hν* = 83.9 eV, corresponding to the transition from 4f to 5d) and off-resonant (*hν* = 85 eV) condition, respectively. One can see the bulk state corresponding to the cross section of the Fermi sphere of the bulk Au crystal: the nearly hexagonal contour centered at the $\bar{\Gamma}$ point. The Shockley surface state is centered at the $\bar{\Gamma}$ point as a small circular contour. The corresponding band dispersions are shown in Fig. 2 (d) and 2(e). For comparison, we chose the data taken at these photon energies and the binding energy to avoid influence of the core-level peaks excited by the second order light. As seen from their subtraction in Fig. 2(c) and 2(f), the intensity enhancement under the resonant condition was estimated to be less than 5%. We were not able to find the momentum dependence and different behavior of bulk and surface states for the intensity enhancement. From these results, we cannot conclude the 5d orbital contribution to the Fermi surface of Au(111).

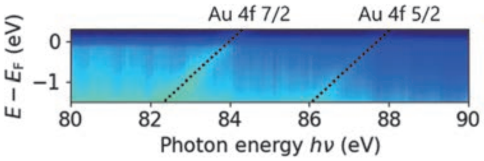

Fig. 1. Photoemission intensity of Au(111) in the valence band region integrated over all momentum as a function of photon energy. Dotted lines indicate the position of for Au $4f_{7/2}$ and $4f_{5/2}$ core levels excited by the second order light.

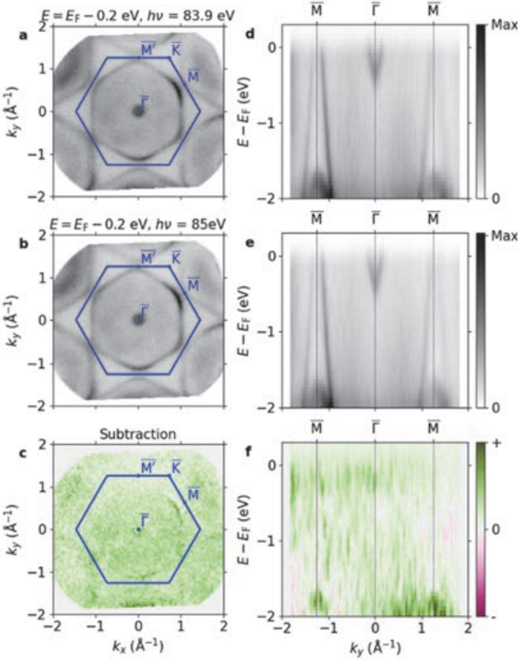

Fig. 2. Momentum-resolved resonant photoelectron spectroscopy of Au(111). (a, b) Momentum distribution at E=E_F-0.2eV excited under the resonant (*hν* = 83.9 eV, corresponding to transition from 4f to 5d) (a) and off-resonant (*hν* = 85 eV) conditions(b). (c) Subtraction between (a) and (b). (d-f) Same as (a-c), but the corresponding band dispersion.

[1] F. Matsui *et al.*, Rev. Sci. Instrum. **94** (2023) 083701.
[2] K. Hagiwara *et al.*, J. Synchrotron Rad. **31** (2024) 540.
[3] F. Matsui *et al.*, J. Phys. Soc. Jpn. **90** (2021) 124710.
[4] A. Sekiyama *et al.*, New J. Phys. **12** (2010) 043045.

BL6B

Infrared Absorption Measurements on Single Crystals and Amorphous Thin-Films of Rubrene

Y. Nakayama[1,2], R. Sakata[1] and Y. Baba[1]
[1]*Department of Pure and Applied Chemistry, Tokyo University of Science, Noda 278-8510, Japan*
[2]*Institute for Molecular Science, Okazaki 444-8585, Japan*

Rubrene (Fig. 1 inset) is a representative p-type organic semiconductor molecule exhibiting considerable charge carrier mobility over 10 cm^2/Vs [1] and widely dispersing intermolecular electronic bands [2] in its single-crystal (SC) phase. One peculiar character of this material is that charge carrier mobilities, crystallographic structures, and ionization energies of its vacuum-deposited thin-films (TFs) differ greatly from those of its SCs [3]. Such changes in structural and electronic properties may lead to changes in vibronic characteristics in its solid-state phases via inequivalent intermolecular interactions. In this work, infrared absorption measurements were performed on SCs and amorphous TFs of rubrene trying to compare intra-molecular vibrations depending on inter-molecular aggregation manners.

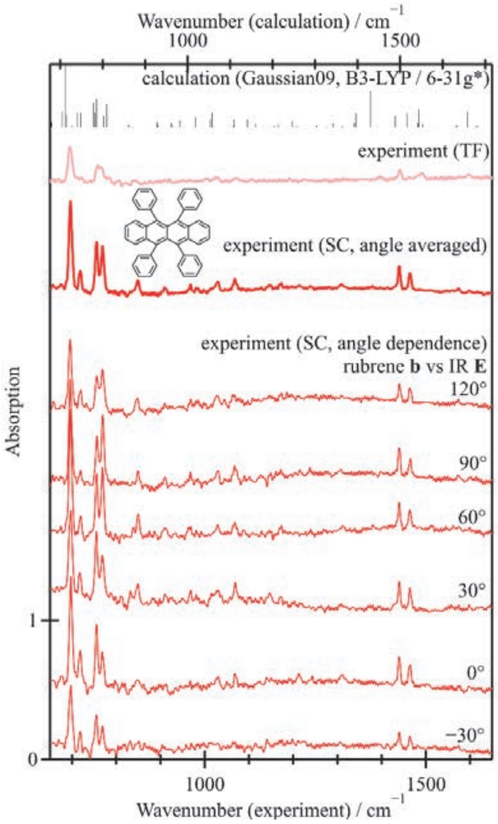

Fig. 1. Quantum chemical calculation results (black) and IR absorption spectra of an amorphous TF (pink) and SC (red) of rubrene. The bottom six curves are spectra of SC depending on orientations of the crystal principal axis **b** of rubrene to the IR **E**. The calculated wavenumber is scaled by a factor 0.9613 [5].

Rubrene SCs were produced by a horizontal physical vapor transport technique and were electrostatically fixed on polycrystalline diamond substrates. TFs of rubrene were prepared by vacuum deposition of thicknesses up to 5 μm on the polycrystalline diamond plates and were afterward taken out of the vacuum. FT-IR measurements were performed at BL6B, UVSOR. Experimental details were described previously [4].

Figure 1 shows IR absorption spectra of a TF and SC of rubrene with quantum chemical calculation results on a single rubrene molecule. While the former was much weaker than the latter due to insufficient film thickness, the peak positions were overall consistent with each other. The peak intensities of SC, especially in a low wavenumber range, clearly exhibited dependence on the in-plane orientation of the sample presumably by variations in relations between transition dipoles **μ** and the IR electric field **E** [4]. Closed-up spectra (Fig. 2) revealed that the IR absorption wavenumbers are mostly unchanged independent of the solid-state phases. Peak broadening for TFs may be caused by diverse inter-molecular conditions, whereas the emergence of peaks derived by **μ**·**E** ≈ 0 modes for SC (#66 and #73) cannot be ruled out as possible causes of the broadening at this stage.

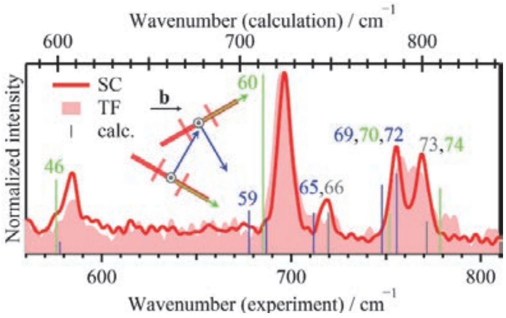

Fig. 2. Experimental and calculation results shown in extended wavenumber scales. The latter are displayed with different colors by its **μ** directions (see inset).

[1] J. Takeya, *et al.*, Appl. Phys. Lett. **90** (2007) 102120.
[2] S. Machida *et al.*, Phys. Rev. Lett. **104** (2010) 156401.
[3] Y. Nakayama, *et al.*, Appl. Phys. Lett. **93** (2008) 173305.
[4] Y. Nakayama, *et al.*, Vib. Spectrosc. **132** (2024) 103681; *idem*, Jpn. J. Appl. Phys. **63** (2024) 09SP07.
[5] J. P. Merrick, *et al.*, J. Phys. Chem. A **111** (2007) 116803.

BL7U

High-Resolution ARPES Study of Pure Electronic Nematicity in FeSe Thin Films on $LaAlO_3$

K. Nakayama[1], T. Kobayashi[2], F. Nabeshima[2], S. Souma[3,4], T. Takahashi[1],
A. Maeda[2] and T. Sato[1,3,4,5,6]
[1]Department of Physics, Tohoku University, Sendai 980-8578, Japan
[2]Department of Basic Science, the University of Tokyo, 3-8-1 Komaba, Meguro, Tokyo 153-8902, Japan
[3]Center for Spintronics Research Network, Tohoku University, Sendai 980-8577, Japan
[4]Advanced Institute for Materials Research (WPI-AIMR), Tohoku University, Sendai 980-8577, Japan
[5]International Center for Synchrotron Radiation Innovation Smart (SRIS), Tohoku University,
Sendai 980-8577, Japan
[6]Mathematical Science Center for Co-creative Society (MathCCS), Tohoku University, Sendai 980-8578, Japan

The iron-based superconductor FeSe is attracting considerable attention because it exhibits unique physical properties distinct from other iron-based superconductors, such as very strong coupling superconductivity in bulk samples and high-temperature superconductivity in monolayers. A particularly intriguing property is its electronic nematic state [Fig. 1(a)], in which the rotational symmetry of the electronic state is reduced from four-fold (C_4) to two-fold (C_2) [1]. While the electronic nematic state in other iron-based superconductors typically develops concurrently with antiferromagnetic order and a tetragonal-to-orthorhombic structural transition, the nematic state in FeSe is markedly different as it is not accompanied by antiferromagnetic ordering. In nearly all high-temperature superconductors discovered thus far, an antiferromagnetic phase exists adjacent to the superconducting phase, leading to the consideration of antiferromagnetic interactions as a primary candidate mechanism for high-temperature superconductivity. In this context, the results for FeSe are puzzling. Understanding the origin of the electronic nematic state is considered a crucial step towards the full understanding of the high-temperature superconductivity mechanism in iron-based superconductors.

As described above, the electronic nematic state in bulk FeSe is not accompanied by antiferromagnetic order. On the other hand, similar to other iron-based superconductors, it is known to undergo a tetragonal-to-orthorhombic structural transition. Therefore, the lattice also possesses C_2 symmetry. In a strict sense, this means the electronic state itself does not break the rotational symmetry independently of the lattice distortion. By contrast, we recently discovered that FeSe thin films grown on $LaAlO_3$ substrates exhibit a “pure” nematic state that emerges without accompanying antiferromagnetic order or even a structural phase transition [2]. Moreover, this pure nematic state coexists with superconductivity. Elucidating the complete picture of this novel electronic nematic state and its relationship to superconductivity is a critical research task.

In this work, we utilized high energy- and momentum-resolution capabilities at low-energy beamline BL7U to perform angle-resolved photoemission spectroscopy (ARPES) measurements on FeSe/$LaAlO_3$. High-quality FeSe/$LaAlO_3$ samples, prepared by pulsed laser deposition, were cleaved *in-situ* under ultrahigh vacuum to obtain clean surfaces suitable for ARPES. As shown in Fig. 1(b), we observed two hole-like branches around the M point of the Brillouin zone. This observation indicates the lifting of band degeneracy between the Fe 3d *xz* and *yz* orbitals, a hallmark of the electronic nematic state. We carefully investigated the evolution of these bands across the nematic transition. Furthermore, high-resolution measurements were performed at very low temperatures. From these comprehensive measurements, we obtained a detailed understanding of the pure nematic state.

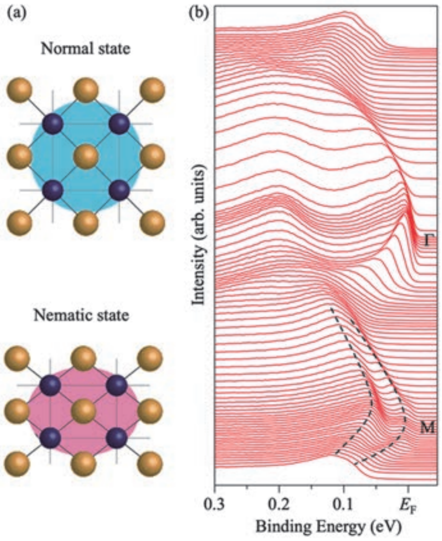

Fig. 1. (a) Schematic of crystal structure and electronic states in the normal state (top) and nematic state (bottom) in bulk FeSe [2]. (b) ARPES spectra along the ΓM high-symmetry line measured in the pure electronic nematic state of FeSe/$LaAlO_3$.

[1] K. Nakayama *et al*., Phys. Rev. Lett. **113** (2014) 237001.
[2] Y. Kubota *et al*., Phys. Rev. B **108** (2023) L100501.

BL7U

Band Dispersion of the Topological Nodal-Line Semimetal KAlGe

T. Ishida[1], S. Huh[1], T. Ikenobe[1], T. Yamada[2], J. Junhyeok[1], A. Mine[1], S. Makita[3], K. Tanaka[3],
Z. Hiroi[1] and T. Kondo[1]
[1]Institute for Solid State Physics, The University of Tokyo, Kashiwa, Chiba 277-8581, Japan
[2]IMRAM, Tohoku University, Sendai 980-0812, Japan
[3]UVSOR Facility, Institute for Molecular Science, Okazaki, Aichi 444-8585, Japan

The compounds NaAlSi, NaAlGe, and KAlGe are part of a family of topological nodal-line semimetals. These materials share nearly identical crystal and electronic structures according to first-principles calculations [1]. However, they display strikingly different physical properties: NaAlSi becomes superconducting below ~7 K, NaAlGe exhibits a pseudogap-like behavior near 100 K, while KAlGe undergoes a metal-to-metal transition at 89 K. This divergence in physical phenomena, despite similar electronic band topology, raises important questions about the underlying mechanisms. In NaAlSi, recent studies suggest that many-body interactions significantly enhance the effective mass of the Fermi surface, contributing to its superconductivity [2]. ARPES measurements have confirmed the existence of a flat band near or just below the Fermi level, which is interpreted as a manifestation of mass enhancement [3]. Furthermore, two topological nodal lines are clearly resolved. To understand the unique behavior of KAlGe, we aim to clarify its band dispersion, especially the position of the flat band, through angle-resolved photoemission spectroscopy (ARPES). Despite theoretical predictions, no experimental band structures for KAlGe have been reported to date, making our study the first direct observation. Single crystals of KAlGe were synthesized using a potassium–indium flux method. Owing to their air sensitivity, all handling and sample preparation were conducted in an argon-filled glovebox. The samples were cleaved *in-situ* under ultrahigh vacuum conditions (4.0×10^{-9} Pa) immediately prior to measurement to expose pristine surfaces. ARPES experiments were performed at 120 K using 17 eV photons at the UVSOR BL7U beamline. Both linear horizontal (LH) and vertical (LV) polarizations were used to probe orbital character.

Figure. 1 consents constant-energy mappings of KAlGe measured with 17 eV LH-polarized light. The overall shape and symmetry closely resemble those of NaAlSi, indicating that the bulk electronic structure is largely conserved within this family. Figure 2 shows the band dispersions along the Γ–X direction. The left and right panels correspond to LH and LV polarization, respectively. Under LH light, we observe features dominated by the Ge $4p_x$ orbital (highlighted in yellow), whereas LV polarization enhances the Ge $4p_\gamma$ orbital (blue). The Al 3s orbital is not clearly observed under either polarization, likely due to matrix element suppression. Most notably, unlike NaAlSi, the flat band is absent below the Fermi energy in KAlGe. This suggests a crucial difference in many-body renormalization or hybridization strength. We propose that the elevated position of the flat band in KAlGe may suppress the density of states at the Fermi level, thereby inhibiting superconductivity while allowing alternative phenomena such as the observed metal-to-metal transition. The polarization dependence also supports orbital selectivity in KAlGe, possibly tied to the directionality of nodal-line dispersion and spin-orbit coupling. Further photon energy-dependent measurements are planned to confirm the three-dimensional character of the observed bands.

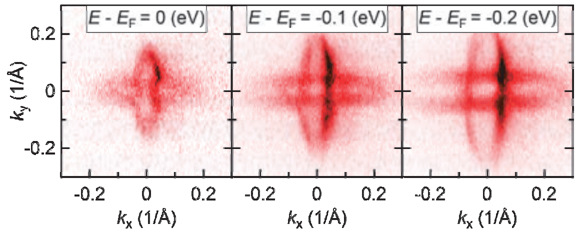

Fig. 1. Constant energy mapping of KAlGe at 120 K with 17 eV LH polarized light.

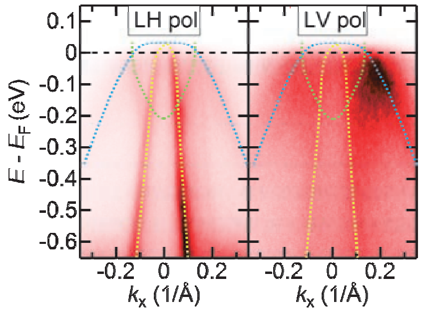

Fig. 2. Electronic structure of KAlGe at 120 K with 17 eV light in Γ-X.

[1] T. Ikenobe, *et al.*, Chem. Mater. **37**(1) (2024) 189.
[2] S. Uji, *et al*, Phys Rev B **105** (2022) 235103.
[3] C. Song, *et al.*, Phys Rev B **105** (2022) L161104.

BL7U

High-Resolution ARPES Study of Topological Superconductor Candidate $PtBi_2$

Y. Morita[1], K. Nakayama[1], T. Kato[2], S. Souma[2,3], S. Masaki[4], T. Ikushima[4], Y. Moriyasu[4], K. Hagiwara[5], F. Matsui[5], K. Tanaka[5,6], T. Takahashi[1], K. Kudo[4] and T. Sato[1,2,3,7,8]
[1]*Department of Physics, Tohoku University, Sendai 980-8578, Japan*
[2]*Advanced Institute for Materials Research (WPI-AIMR), Tohoku University, Sendai 980-8577, Japan*
[3]*Center for Science and Innovation in Spintronics (CSIS), Tohoku University, Sendai 980-8577, Japan*
[4]*Department of Physics, Graduate School of Science, The University of Osaka, Toyonaka 560-0043, Japan*
[5]*UVSOR Synchrotron Facility, Institute for Molecular Science, Okazaki 444-8585, Japan*
[6]*School of Physical Sciences, The Graduate University for Advanced Studies (SOKENDAI), Okazaki 444-8585, Japan*
[7]*International Center for Synchrotron Radiation Innov1ation Smart (SRIS), Tohoku University, Sendai 980-8577, Japan*
[8]*Mathematical Science Center for Co-creative Society (MathCCS), Tohoku University, Sendai 980-8578, Japan*

Following the discovery of topological insulators, the exploration for new topological materials is actively progressing. A prime example is the Dirac semimetal, which features a Dirac-cone-type band dispersion where the bulk conduction and valence bands touch at discrete points in three-dimensional Brillouin zone. These materials hold promise for applications in next-generation ultra-high-speed electronics and spintronics. Furthermore, among topological semimetals, Weyl semimetals host spin-polarized Dirac cones (Weyl cones) in their bulk band structure. Weyl semimetals are realized in systems where spatial inversion or time-reversal symmetry is broken. Numerous quantum phenomena, such as the anomalous Hall effect and the chiral anomaly, are predicted for Weyl semimetals, and their experimental verification is actively underway. In recent years, aiming to realize even more exotic topological phases, the exploration of materials that integrate superconductivity with Dirac or Weyl semimetal states has become a key research objective. Introducing superconductivity is anticipated to facilitate the formation of unconventional Cooper pairs, potentially leading to topological superconductivity and Majorana fermions.

Here, we focus on $PtBi_2$ [Fig. 1(a)], a transition metal dichalcogenide with broken spatial inversion symmetry. This material is a Weyl semimetal candidate and exhibits bulk superconductivity below 0.6 K. Moreover, a recent report suggests potential surface superconductivity with a significantly higher transition temperature above 10 K [1]. These combined Weyl semimetallic and superconducting characteristics make $PtBi_2$ a promising platform for exploring topological superconductivity. However, key aspects of its electronic structure relevant to topological superconductivity, such as bulk Weyl cones, require further investigation.

Using bulk-sensitive low-energy photons at BL7U, we mapped the three-dimensional bulk electronic structure of $PtBi_2$. Our results shown in Fig. 1(b) reveal signatures of spin-split bulk bands, recognized from Rasha-like band dispersion observed around the M point. Such spin splitting, likely originating from the broken inversion symmetry, is a prerequisite for the predicted Weyl semimetal phase. To further investigate this phase, we performed high-resolution measurements to directly observe the Weyl cones near the Fermi level.

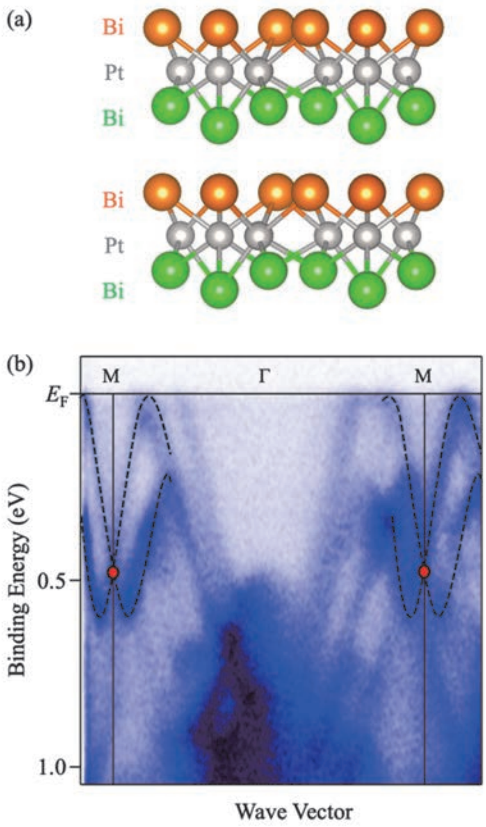

Fig. 1. (a) Crystal structure of $PtBi_2$. (b) Plot of ARPES intensity measured in the normal state along the ΓM high-symmetry line.

[1] A. Kuibarov *et al.*, Nature **626** (2024) 294.

BL7U

Probing Hole Doping Effects in Ti-Substituted Ta_2NiSe_5 Investigated by Angle-Resolved Photoemission Spectroscopy

J. Han[1], K. Aido[1], S. Tsuchida[2], Y. Hirose[2], R. Settai[2], S. Makita[3], K. Tanaka[3] and T. Kondo[1]
[1]*ISSP, University of Tokyo, Kashiwa, Chiba 277-8581, Japan*
[2]*Department of Physics, Niigata University, Niigata 950-2181, Japan*
[3]*UVSOR Facility, Institute for Molecular Science, Okazaki, Aichi 444-8585, Japan*

Ta_2NiSe_5 has emerged as one of the most prominent candidates for excitonic insulator systems. With a direct band gap, it undergoes an insulating transition accompanied solely by a $q = 0$ structural distortion at $T_s = 329$ K, without charge density wave (CDW) formation [1]. A central issue in this field is whether the transition is primarily driven by excitonic condensation or by lattice instability. Since exciton formation originates from the Coulomb attraction between electrons and holes, tuning the screening strength through carrier doping could facilitate a disentangled investigation of the respective roles played by electronic and structural degrees of freedom.

To systematically explore the effects of carrier doping, we investigated the electronic structure of Ti-substituted Ta_2NiSe_5, where Ti atoms replace Ta sites, introducing effective hole doping due to the difference in their valence electron configurations. Single crystals of pristine and Ti-substituted Ta_2NiSe_5 were synthesized by the chemical vapor transport method. The samples were cleaved *in-situ* to obtain clean surfaces for measurements. Angle-resolved photoemission spectroscopy (ARPES) measurements were performed at BL7U of UVSOR with a photon energy of 18 eV. All data were collected at a sample temperature of 83 K (below T_s). To distinguish the orbital characters associated with Ta, Ni, and Se atoms, both linear vertical (LV) and linear horizontal (LH) polarizations were employed during the measurements [2].

Figure 1 compares the band structures along the Γ-X direction for pristine and Ti-substituted Ta_2NiSe_5. Under LV polarization [Figs. 1(a) and 1(b)], bands primarily derived from Ta 5*d* orbitals are selectively enhanced, while LH polarization emphasizes the Ni 3*d*-derived bands [Figs. 1(c) and 1(d)]. In the pristine sample [Figs. 1(a) and 1(c)], the characteristic flat top of the valence band, associated with the excitonic insulating state, appears near a binding energy of approximately 170 meV. Upon Ti substitution [Figs. 1(b) and 1(d)], the overall band structure, which includes the characteristic flat band, shifts toward lower binding energies without significant deformation compared to the pristine one. This implies that the level of Ti substitution may not yet be sufficient to induce a complete insulator-to-semimetal transition.

Assuming that carrier doping suppresses exciton condensation, the upward shift of the flat-top valence band to approximately 60 meV can be regarded as an indication of gap narrowing. As highlighted by the black arrows in Figs. 1(b) and 1(d), only the spectral weight near the Fermi level (E_F) is depleted, which may suggest the emergence of a pseudogap. With a slightly higher level of Ti substitution, the bands may begin to overlap, potentially leading to a semimetallic transition. Unlike previous approaches based on potassium deposition [3], our substitution-based strategy avoids interpretational ambiguities arising from the Stark effect, thereby offering a cleaner platform to disentangle the respective roles of electronic and lattice degrees of freedom in the excitonic insulating state.

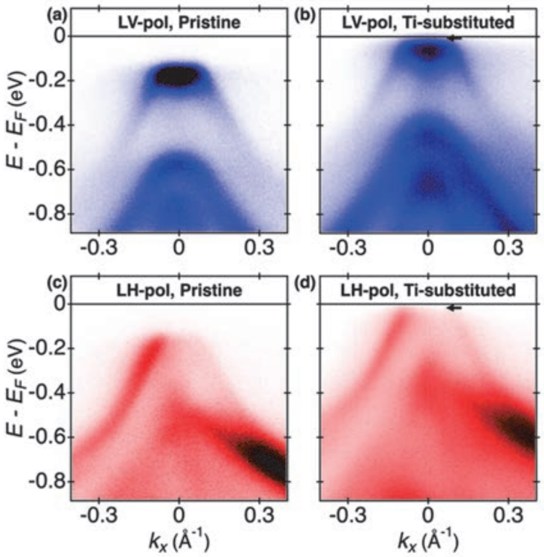

Fig. 1. Polarization-dependent ARPES spectra of pristine (a,c) and Ti-substituted (b,d) Ta_2NiSe_5 along the Γ-X direction, measured with LV (a,b) and LH (c,d) polarizations. Black arrows indicate spectral weight suppression near E_F .

[1] Y. Wakisaka *et al.*, Phys. Rev. Lett. **103** (2009) 026402.
[2] T. Kaneko *et al.*, Phys. Rev. B **87** (2013) 035121.
[3] X. Chen *et al.*, Phys. Rev. Res. **5**,(2023) 043089.

BL7U

Observation of Electronic Structure of Organic Mott Insulator β'-(BEDT-TTF)$_2$ICl$_2$ by Angle-Resolved Photoelectron Spectroscopy

R. Nakazawa[1], K. Fukutani[1], Y. Ishida[2], S. Makita[3], K. Tanaka[3],
T. Kobayashi[4], H. Taniguchi[4] and S. Kera[1,2,3]
[1]*Department of Photo-Molecular Science, Institute for Molecular Science, Okazaki 444-8585, Japan*
[2]*Faculty of Engineering, Chiba University, Chiba 263-8522, Japan*
[3]*UVSOR Synchrotron Facility, Institute for Molecular Science, Okazaki 444-8585, Japan*
[4]*Faculty of Science, Saitama University, Saitama 338-8570, Japan*

Organic materials have the potential to promote the sustainable development of science and technology due to their flexibility and high environmental compatibility. Among them, strongly correlated organic molecular crystals exhibit a variety of quantum phases, such as superconductivity, spin liquid state, Mott insulating phase, and topological phase [1, 2].

(BEDT-TTF)$_2$X belongs to the strongly correlated organic molecular crystals and is a charge-transfer complex. Here, X means anion. Due to the electron transfer of the BEDT-TTF molecule to X, the valence band described from the highest occupied molecular orbital (HOMO) offers a half-filled or 1/4 filled. Whether the system is a metallic phase or an insulating phase depends on the microscopic electronic structure with Coulomb interaction energy. In the case of the half-filled band for a dimer state and large Coulomb interaction energy, the valence band from the anti-bonding HOMO state splits into upper and lower Hubbard bands, leading to an insulating phase which is called Mott insulator.

While the origins of the Mott insulator phase are largely encoded in the electronic structures as mentioned above, direct experimental data on the momentum-resolved electronic structure is missing. In the case of a Mott insulator, β'-(BEDT-TTF)$_2$ICl$_2$ [3, 4], electrical measurements confirm that it is an insulating phase at ambient pressure [1]. On the other hand, the band obtained by theoretical calculations crosses the Fermi level because they do not correctly account for the Coulomb interaction [5], and the true picture of electronic structure of this material is not unclear. To understand the many-body nature of β'-(BEDT-TTF)$_2$ICl$_2$, such as whether this material has the electronic states as a metallic phase or an insulating phase, first it is important to directly observe the momentum-resolved electronic structures which previous studies lack.

In this study, we observed the valence band electronic structure of β'-(BEDT-TTF)$_2$ICl$_2$ using angle-resolved photoelectron spectroscopy (ARPES) at BL7U in UVSOR.

Figure 1 shows the valence band structure observed using excitation energy of $h\nu$ = 40 eV at T = 150 K. Fig.1(a) shows the photoemission intensity plot along the short crystal axis (c-axis), and Fig. 1(b) is the corresponding second derivative plot. A dispersive band with the width of ~0.14 eV is observed at the binding energy (E_b) of ~0.7 eV. Since the observed band periodicity corresponds to the periodicity of Brillouin zone, we judged that we have successfully observed itinerant electrons in this material. In addition, the band with almost no dispersion was observed at the E_b of ~0.4 eV. These bands at the E_b of ~0.4 and ~0.7 eV are ascribed to the lower Hubbard and the bonding band, respectively. Moreover, we have successfully observed the photoelectrons along other high-symmetric momentum directions to reveal the details of the electronic structures.

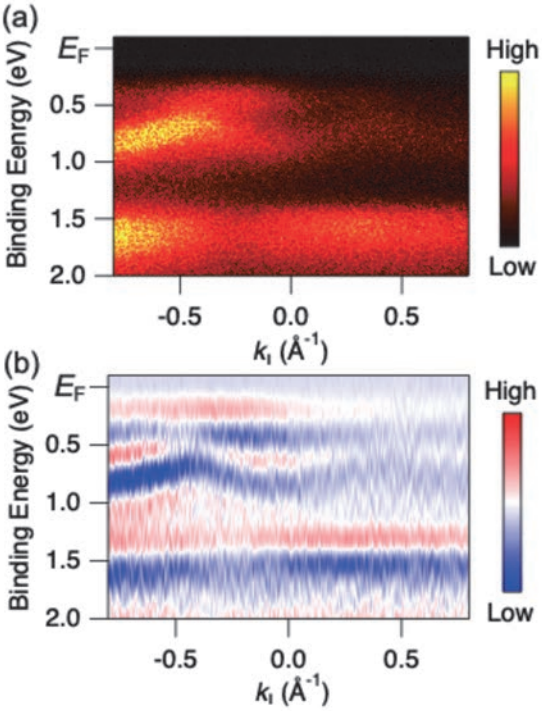

Fig. 1. (a) Photoemission intensity plot, and (b) the corresponding second derivative plot of β'-(BEDT-TTF)$_2$ICl$_2$ crystal observed at $h\nu$= 40 eV, T = 150 K.

[1] K. Kanoda, J. Phys. Soc. Jpn. **75** (2006) 051007.
[2] T. Nomoto *et al.*, Nat. Commun. **14** (2023) 2130.
[3] T. J. Emge, *et al.*, J. Am. Chem. Soc. **108** (1986) 695.
[4] H. Kobayashi, *et al.*, Chem. Lett. **15** (1986) 89.
[5] T. Koretsune, C. Hotta, Phys. Rev. B **89** (2014) 045102.

BL7U

Angle-Resolved Photoemission Study of Layered MAB Phase Compounds MoAlB

T. Ito[1,2], K. Kawano[1], N. Yuanzhi[1], M. Nakatake[3], K. Tanaka[4,5],
A. Sharma[6], H. Pazniak[6] and T. Ouisse[6]
[1]*Graduate School of Engineering, Nagoya University, Nagoya 464-8603, Japan*
[2]*Synchrotron radiation Research center, Nagoya University, Nagoya 464-8603, Japan*
[3]*Aichi Synchrotron Radiation Center, Seto 489-0965, Japan*
[4]*UVSOR Facility, Institute for Molecular Science, Okazaki 444-8585, Japan*
[5]*The Graduate University for Advanced Studies, Okazaki 444-8585, Japan*
[6]*Grenoble Alpes, CNRS, Grenoble INP, LMGP, F-38000 Grenoble, France*

MAB phase compounds are layered compounds formed by combining transition metals M and III-A (IV-A) group elements A and B, and have a layered crystal structure in which a strong MB layer and two A layers are stacked in the b-axis direction [1]. In this system, it is expected that the atomic layer system MBenes formed only from MX layers will be obtained by removing the A atoms by HF treatment or exfoliation. Therefore, this system has attracted attention in recent years as a new atomic layer system that can replace graphene [2]. Among boron compounds, MoAlB is known to be an excellent system, especially in terms of applications, due to its relatively good processability, high temperature oxidation resistance, high thermal conductivity, and high electrical conductivity. Furthermore, the results of DFT calculations [3] predict a three-dimensional Dirac semimetal nature of MoAlB. In this study, we have performed angle-resolved photoemission spectroscopy (ARPES) on MAB phase compound MoAlB to directly investigate the electronic structure of this system.

ARPES measurements were performed at the UVSOR-III BL7U. Inter-plane ARPES data were acquired with using $h\nu = 11 - 30$ eV at T = 30 K. Single crystals were cleaved in situ along (010) plane.

Figure 1(a) shows the obtained Fermi surface (FS) image on the ΓYZT plane . It has been found that the electronic structure around ΓZ line formed by two hole-like FSs with quasi-two-dimensional character, which are qualitatively reproduced by density functional theory (DFT) calculations (not shown). On the other hand, we have found three dimensional FS around Z point and $k_y \sim -0.5$ Å^{-1} around ΓY line. To elucidate three-dimensional electronic structure of MoAlB, we indicate inter-plane ARPES image along ΓZ line in Fig. 1(b). The inner potential V_0 is estimated to be 27 eV based on the symmetry of the dispersive features. From the comparison between ARPES and DFT calculation, narrow parabolic dispersions around 0.5 and 2.7 eV seem to show qualitative agreement. However, a sharp, flat pocket symmetrically observed around the Z point on the present ARPES is not predicted by the DFT calculations. Although the origin of this discrepancy remains unclear, it is plausible that the formation of the heavy electron surface is associated with a chemical potential shift of approximately 100 meV. To pursue the relation between anomalous FS and the thermodynamic properties of MoAlB, further studies are intended.

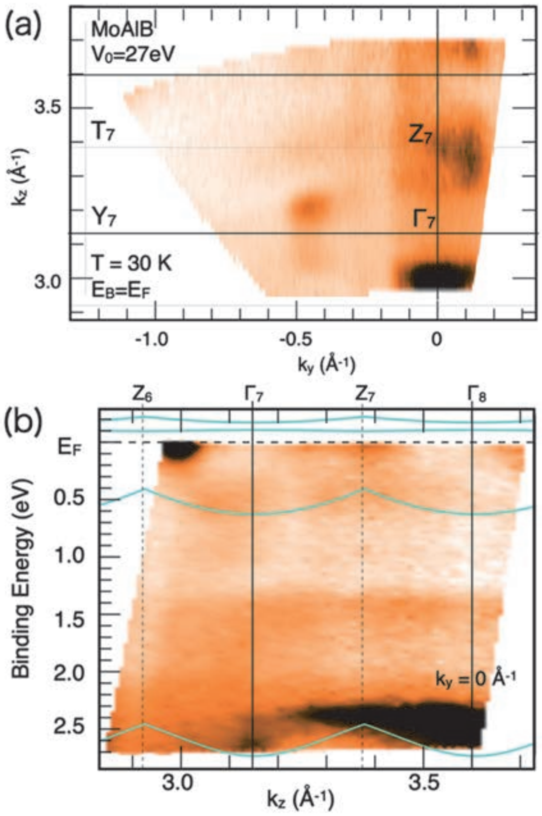

Fig. 1. (a) Fermi surface along ΓYZT plane of MoAlB obtained by inter-plane ARPES measurements. (b) Inter-plane ARPES image along ΓZ line. Solid lines are DFT calculation along ΓZ line.

[1] Y. Huang *et al.*, Small **18** (2022) 2104460.
[2] X. Zhu *et al.*, Nature Commun. **12** (2021) 4080.
[3] Y. Huang *et al.*, Materials Today Physics **33**(2023) 101060.

BL7U

Exploration of Electronic Band Structure and Topological Surface States in Ni-Doped PdSeTe

Y. Kumar[2], S. Ideta[1,2] and K. Shimada[1,2]
[1]*Graduate School of Advanced Science and Engineering, Hiroshima University, Hiroshima 739-0046, Japan.*
[2]*Hiroshima Research Institute for Synchrotron Radiation Science (HiSOR), Hiroshima University, Hiroshima 739-0046, Japan.*

In recent years, exploring the electronic structures of topological insulators and topological semimetals has become a central focus in condensed matter physics. Among these, Dirac and Weyl semimetals have attracted significant attention, particularly in the realm of spintronics, due to their unique and enhanced physical properties [1, 2]. Layered transition-metal dichalcogenides (TMDCs) with the chemical formula AB_2 (where A is a transition metal and B is a chalcogen) have been the subject of extensive research due to their diverse range of physical properties, including superconductivity and the emergence of charge density waves (CDWs).

Recently, we have reported the existence of topological surface states and enhancement of superconducting transition temperature in 1T-PdSeTe [3], which is the sister compound of $PdTe_2$ by replacing 50% of Te atoms with Se, trying to break the inversion symmetry to create a Weyl semimetal. We explored the surface and bulk electronic structures of the superconducting type-II Dirac semimetal 1T-PdSeTe, which exhibits a superconducting transition temperature (T_C = 3.2 K) nearly twice that of its counterpart 1T-$PdTe_2$ (T_C = 1.6 K). Angle-resolved photoemission spectroscopy (ARPES) and density functional theory (DFT) analyses revealed topological surface states and electronic band structures closely resembling those of 1T-$PdTe_2$. These findings suggest that the CdI_2-type lattice symmetry plays a dominant role in dictating the band dispersion, largely unaffected by atomic-scale disorder in the chalcogen layers. To the best of our knowledge, we were the first to demonstrate that the PdSeTe superconductor hosts topological surface states.

In order to break the time reversal symmetry in this material, we have tried to dope a magnetic impurity (Ni) at the Pd-site. We have successfully grown the $Ni_xPd_{1-x}SeTe$ single crystals. We have measured the electronic band structure using ARPES at BL7U at UVSOR. The objective of this study was to carry out ARPES measurements on Ni-doped PdSeTe samples to elucidate their electronic band structure. Particular emphasis was placed on analyzing the band dispersion and Fermi surface with the goal of identifying signatures of topological surface states and Fermi arcs. We have prepared $Ni_xPd_{1-x}SeTe$ samples and aligned them in a high-symmetry direction using the Laue diffraction (XRD) available at the UVSOR-III synchrotron facility to accurately measure the band dispersion in the high-symmetry direction.

We have cleaved three samples of $Ni_xPd_{1-x}SeTe$ to obtain a clean surface; the cleave was very good, resulting in the sharp band dispersion. We have performed the ARPES experiment and mapped the Fermi surface at photon energy 25 eV as shown in Fig. 1. Also, I have measured high symmetry cuts in the Γ-M direction to investigate the electronic band structure with both *s*- and *p*-polarizations. I have performed the photon energy-dependent measurement from 9 eV to 25 eV to observe the k_z dependence. We have also optimized the beam slit to improve the data quality and resolution. Detailed records of experimental procedures, sample characteristics, and measurement results were maintained during the experiment. We have to do further measurements to complete the data set.

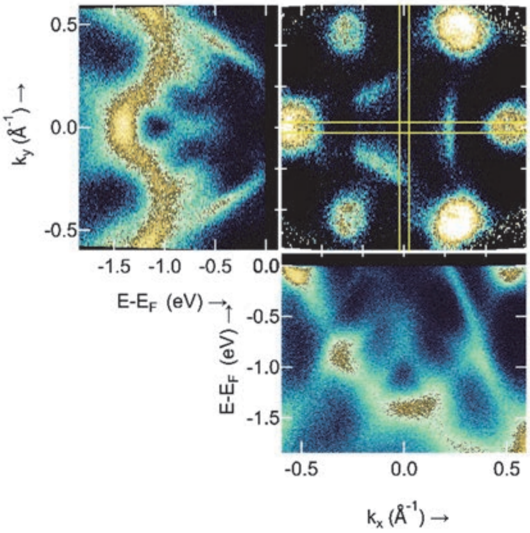

Fig. 1. Fermi Surface of $Ni_xPd_{1-x}SeTe$ single crystal at 25 eV alongside band dispersion in the K-Γ-K and M-Γ-M directions.

[1] N. P. Armitage, E. J. Mele, A. Vishwanath, Rev. Mod. Phys. **90** (2018) 015001.
[2] A. A. Burkov, Nat. Mater. **15** (2016) 1145.
[3] Y. Kumar, K. Shimada *et al*, Phys. Rev. Res. **7** (2025) 013174.

BL7U

Role of Orbital-Selective Mott Phase on Topological Properties in Iron Chalcogenide Superconductors

Y. Kim[1], J. Yoo[1], S. Kim[1] and C. Kim[1]

[1]*Department of Physics and Astronomy, Seoul National University, Seoul 08826, South Korea*

Orbital-selective Mott phase (OSMP), where one band becomes effectively localized while other bands remain metallic, emerges in correlated multiorbital systems. In electronic structures, the OSMP is characterized by a loss of spectral weight and broadening of the associated band at high temperatures [1]. This phenomenon has attracted much attention since its ubiquity; many strongly correlated multiorbital systems exhibit OSMP. Despite such interests to OSMP, research on its relation to practical physical properties remains elusive.

Here, we investigate the relationship between OSMP and non-trivial topology in FeTe$_{1-x}$Se$_x$ (FTS), iron chalcogenide superconductors. FTS exhibit non-trivial topology as well as unconventional superconductivity. The non-trivial topology arises from the band inversion of the odd-parity p_z and d_{xz} bands along the $\Gamma - Z$ line [2]. This in turn suggest that to study the impact of the OSMP on the topological properties of FTS, it is necessary to investigate the electronic structures of FTS along the $\Gamma - Z$ line.

In ARPES measurements, two aspects should be considered for the measurements; i) as the band of interest is pz band, photon energy should be lower than 20 eV considering photoionization cross section ii) photon energy should be tunable for the k_z-dependent measurements. UVSOR Beamline 7U satisfies the aforementioned conditions [3]. Here, we report successful measurement results of the electronic structures of FTS along the $\Gamma - Z$ line as a function of Se/Te ratio and temperature in BL 7U.

Shown in Figs. 1**a-d** are electronic structures of FTS along the $\Gamma - Z$ line with selenium contents of x = 0.04, 0.09, 0.19, and 0.31, respectively. They all show a dispersive band, which can be attributed to the odd-parity p_z band. To track the evolution of the p_z band as a function of doping, the top and bottom positions of the band at the Γ and Z points, respectively, are extracted from a two-dimensional fitting as shown in Fig. 1**e**. The p_z band overall moves towards lower energy for lower Se contents. The notable point of the doping-dependent evolution is that the band at the top of the p_z band at the Γ point goes below the Fermi level at x = 0.04. If the p_z band goes below the d_{xz} band which is near the Fermi level, this makes the inversion parities of the Γ and Z both odd, resulting in trivial topology. This suggests that topological phase transition occurs between x = 0.04 and 0.09, resulting in trivial topology at x = 0.04.

Figures 1**f–i** show temperature-dependent ARPES results for the sample with x=0.19 measured at temperatures of 30 K, 50 K, 90 K, and 175 K, respectively. Unlike the doping-dependent behavior, the position of the odd-parity band does not change with temperature.

In summary, we have successfully measured the odd-parity band in FTS, providing insights into its topology. These results may shed light on the role of OSMP in determining the system's topological properties.

[1] M. Yi *et al.*, npj Quantum Mater. **2** (2017) 57.
[2] P. Zhang *et al.*, Science **360** (2018) 6385.
[3] Y. Kim *et al.*, Nat. Commun. **14** (2023) 4145.

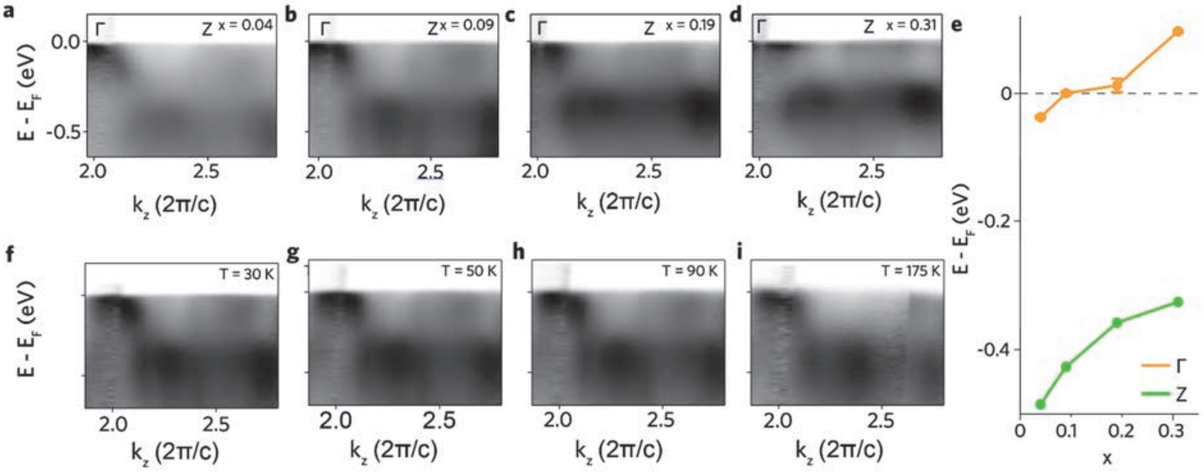

Fig. 1. **a-d** Band dispersion along $\Gamma - Z$, with selenium contents of x = 0.04, 0.09, 0.19, and 0.31, respectively. e Position of the p_z band at the Γ and Z points. **f-i** Band dispersion along $\Gamma - Z$, with temperatures of 30 K, 50 K, 90 K and 175 K, respectively.

BL7B

Evaluation of Fluorescence Lifetimes of UV-Cured Scintillators for the Next K_L^0 Rare Decay Experiment at J-PARC

Y. Tajima[1], R. Abe[1], T. Naito[1], Y. Honma[1], N. Izawa[1], S. Yamamoto[1] and H. Y. Yoshida[1]
[1]*Department of Science, Yamagata University, Yamagata 990-8560, Japan*

J-PARC E14 KOTO [1] is the current running experiment of searching for the direct CP violating decay $K_L \rightarrow \pi^0 \nu \bar{\nu}$ decay. This decay mode is considered to be sensitive to new physics beyond the Standard Model (SM), and its branching ratio is predicted to be 3.0×10^{-11} in the SM with about 2% theoretical uncertainly. The upper limit currently obtained on the branching fraction of $K_L \rightarrow \pi^0 \nu \bar{\nu}$ decay is 2.2×10^{-9} at the 90% confidence level [2].

We are planning the next generation $K_L \rightarrow \pi^0 \nu \bar{\nu}$ experiment, called KOTO-II [3]. KOTO-II experiment uses a beam intensity about three times higher and a decay volume about five times longer than that of KOTO. The operation of the detectors in KOTO-II are required higher counting rates. To satisfy this requirement, the scintillators need to have a short fluorescence lifetime, which enables fast time response.

Recently, a new UV-cured scintillator with high light yield has been developed [4]. The scintillators are expected to be easy to fabricate and low cost.

We are currently evaluating its various characteristics for use in KOTO-II experiment. For this purpose, the fluorescence spectrum and decay curve of a newly developed high light yield UV-cured plastic scintillator were measured in this experiment.

The fluorescence decay curves were measured by using light pulses from visible to near ultraviolet under single bunch operation, which enables a time-correlated single-photon counting.

In this experiment, ethoxylated bisphenol A diacrylate (EBECRYL 150 supplied from Daicel Allnex) was used as the host polymer, Irgacure TPO as the photoinitiator, DPO and POPOP as wavelength shifters.

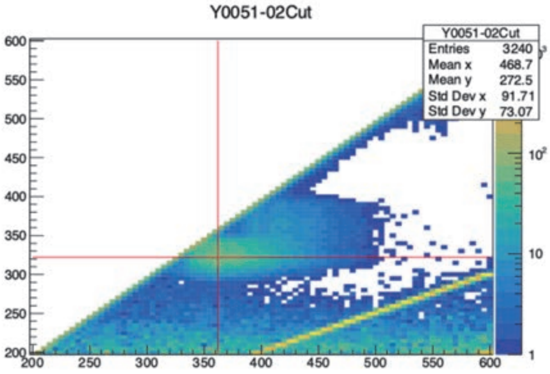

Fig. 1. 2D fluorescence spectra of the UV-cured host polymer. Y-axis is excitation wave length (nm) and X-axis is emission wave length (nm).

Figure 1 shows the 2D fluorescence spectra of the UV-cured host polymers and Fig. 2 shows of the UV-cured scintillator. Figure 3 shows the decay curves. The blue line is the data of the host polymer for the 392 nm band under excitation at 240 nm, the red line is the data of the scintillator data for the 450 nm band under excitation at 322 nm.

Now that we have established a basic evaluation method for UV-cured scintillators, we plan to evaluate other UV-cured scintillators.

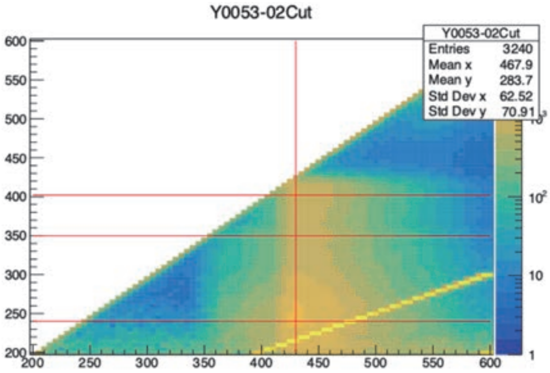

Fig. 2. 2D fluorescence spectra of the UV-cured host polymer with DPO and POPOP.

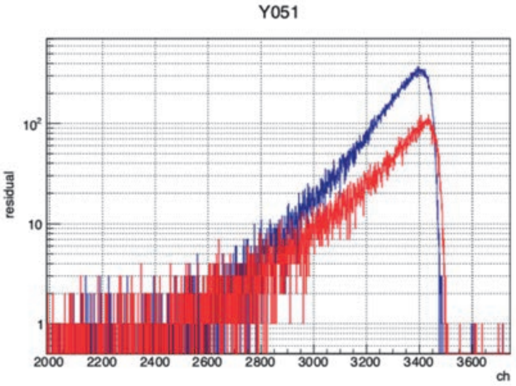

Fig. 3. Decay curve of the UV-cured host polymer (blue) and UV-cured scintillator (red). (946ch/ns)

[1] J. Comfort *et al.*, Proposal for $K_L \rightarrow \pi^0 \nu \bar{\nu}$ Experiment at J-PARC (2006).
[2] J.K. Ahn *et.al.*, Phys. Rev. Lett. **134** (2025) 081802.
[3] J.K. Ahn *et.al.*, J-PARC PAC (arXiv 2501.14827).
[4] N. Hayashi and M.Koshimizu, J. Lumin. **277** (2025) 120993.

BL7B

Excitation Spectra of Plastic Scintillators Based on PVK Containing Different Organic Fluorescent Molecules

M. Koshimizu[1]

[1]*Research Institute of Electronics, Shizuoka University, 3-5-1 Johoku, Chuo-ku, Hamamatsu 432-8011, Japan*

Scintillators are a kind of phosphors that can be used for radiation detection in combination with photon detectors (e.g. photomultiplier tubes) to form scintillation detectors, where scintillation photons upon impinge of ionizing radiation are converted and amplified into electric pulsed signals. Because the response speed of the photon detectors is faster than the decay of the scintillation of scintillators in most cases, scintillators exhibiting fast scintillation decay is necessary to achieve excellent timing resolutions or detection capability at high counting rate with short dead time. From the viewpoint of fast response, plastic scintillators are favorable owing to their fast scintillation decay with typically < 10 ns, which is much faster than those of inorganic scintillators [1, 2]. In addition, scalability and low production cost of the plastic scintillators are favorable to large-scale detectors used in high-energy and particle physics. A significant drawback of the plastic scintillators is low scintillation light yield of typically ~10,000 photons/MeV or less, which is significantly smaller than those of inorganic scintillators. A cause of this low scintillation yield is the formation of triplet excited states in the host polymer, which is formed upon recombination of electron–cation pairs after ionization. The use of the triplet states is the key to enhance the scintillation light yield of plastic scintillators.

Recently, triplet excited states have been efficiently used for photon emission in organic light-emitting diodes via efficient phosphorescence or thermally activated delayed fluorescence. If such utilization of triplet excited states is possible in plastic scintillators, one can enhance scintillation light yield in plastic scintillators. To achieve the scintillation light yield in this approach, it is necessary to develop appropriate fluorescent molecules that can convert the energy of triplet excited states into photons via delayed fluorescence or phosphorescence and a technique to analyze the contribution of photon emission originated from triplet excited states. Recently, we found that the contribution of emission originating from singlet and triplet excited states can be analyzed based on excitation spectra in VUV region [3] and difference in the decay behavior at different excitation wavelengths in VUV—UV region [4]. In the previous study, we have analyzed the properties of plastic scintillators based on polystyrene. In this study, the emission properties of plastic scintillators based on polyvinyl carbazole (PVK) were analyzed.

The samples were plastic scintillators based on PVK containing POPOP, bis-MSB, TPB, or DPA as the fluorescent molecules. The photoluminescence spectra of the samples under VUV irradiation at different wavelengths were obtained at BL7B of UVSOR, Institute for Molecular Science, Japan. Based on the photoluminescence spectra and the excitation light intensity as functions of excitation wavelength, we obtained excitation spectra in VUV region.

Excitation spectra of the samples containing bis-MSB and DPA are presented in Figs. 1 and 2, respectively. The spectra were similar regardless of the contained organic fluorescent molecules. The spectra were also similar to those of polystyrene-based plastic scintillators [3].

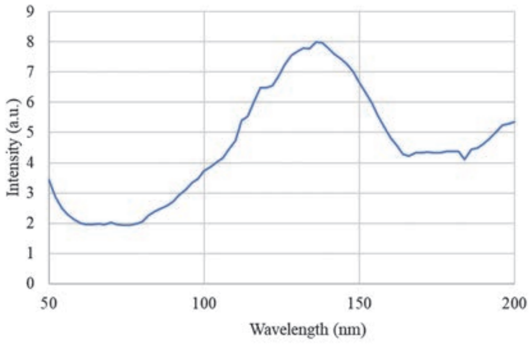

Fig. 1. Excitation spectra of PVK-based plastic scintillators containing bis-MSB.

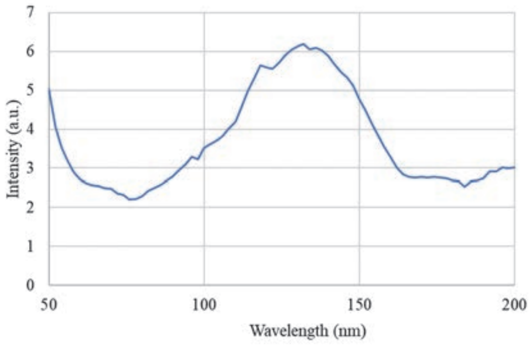

Fig. 2. Excitation spectra of PVK-based plastic scintillators containing DPA.

[1] M. Koshimizu, Jpn. J. Appl. Phys. **62** (2023) 010503.

[2] M. Koshimizu, J. Lumin. **278** (2025) 121008.

[3] M. Koshimizu, Y. Fujimoto, and K. Asai, UVSOR Activity Report **50** (2022) 111.

[4] M. Koshimizu, UVSOR Activity Report **51** (2023) 118.

BL7B

Vacuum Ultraviolet Characterization of Li-Glass as a Potential Neutron Scintillator

T. Shimizu[1], K. Shinohara[1], K. Yamanoi[1] and N. Sarukura[1]
[1]*Institute of Laser Engineering, The University of Osaka, 2-6 Yamadaoka Suita, Osaka 565-0875 Japan*

In nuclear fusion experiments, neutron detection plays a vital role in monitoring both operational efficiency and radiation safety. Primary neutrons, being high in flux, are typically detected using conventional plastic scintillators. However, scattered neutrons, generated through secondary nuclear reactions and arriving with a time delay, are present in much smaller quantities. Their reliable detection demands scintillators with high neutron sensitivity and fast optical response to distinguish their signals from primary neutrons and associated X-rays.

Scattered neutrons generally possess energies in the range of 0.2 to 0.6 MeV. ^{6}Li is known to have a high neutron absorption cross-section within this energy range, and ^{6}Li-containing glass scintillators doped with Ce^{3+} have long been employed for thermal neutron detection. Commercial products such as GS2, GS20, and KS20 are based on Ce^{3+}-doped Li_2O–SiO_2 glass matrices. However, these materials exhibit luminescence decay times of 50–70 ns, insufficient for the 25 ns time resolution required in time-of-flight (TOF) neutron measurements.

To address this issue, a new type of scintillator based on a $20Al(PO_3)_3$–80LiF (APLF) glass matrix was developed. This material offers superior UV transparency and minimal self-absorption, making it ideal for shorter-wavelength luminescence. By replacing Ce^{3+} with Pr^{3+}, the emission wavelength was shifted from 300–350 nm to 250–300 nm, effectively shortening the luminescence decay time.

Previously, We have compiled the analysis and discussion of the X-ray absorption near edge structure (XANES) spectroscopy for the presence of Pr ions in the glasses with a oxidation state.[1] .

In addition to APLF, we investigated alternative lithium glass matrices for scintillator use. Collaborative efforts led to the development and evaluation of various Pr-doped lithium glasses: $20Li_2O$–20CaO–$60SiO_2$+ $0.3Pr_2O_3$(LCSO+0.3Pr), $30Li_2O$–$70B_2O_3$+$0.3Pr_2O_3$ (LBO+ 0.3Pr), $30Li_2O$–$60P_2O_5$–$10Al_2O_3$ + $0.3Pr_2O_3$ (LPA+ 0.3Pr).[2]

In FY2024, we will focus on LPA-type glasses with varied Pr concentrations, as they have shown promise in luminescence control. The samples under evaluation include: LPA10+0.1Pr, LPA10+0.3Pr, LPA10+0.5Pr, LPA10+1Pr, LPA10+2Pr. All samples are solid, non-volatile, and pose no safety concerns.

Spectral measurements were conducted at the UVSOR synchrotron facility using the VUV beamline. A combination of spectrometers, cooled CCD cameras, and photomultiplier tubes (PMTs) was used to measure transmission, absorption, and emission spectra. The samples were placed in a vacuum chamber (pressure < 1.0×10^{-5} Pa) and irradiated with 100–180 nm synchrotron radiation. Si photodiodes were used for transmission measurements, while luminescence was detected using PMTs and CCD cameras. Temperature-controlled experiments were performed from liquid helium temperature up to room temperature, and emission was recorded in the 200–800 nm range. The excitation wavelengths were selected based on prior photoluminescence excitation spectra.

The transmission spectra for the LPA samples showed a systematic shift in the absorption edge corresponding to varying Pr concentrations, indicating successful doping (Fig.1). However, attempts to measure luminescence spectra were hindered by reduced system sensitivity. The resulting emission signals were too weak for reliable detection under the current measurement setup.

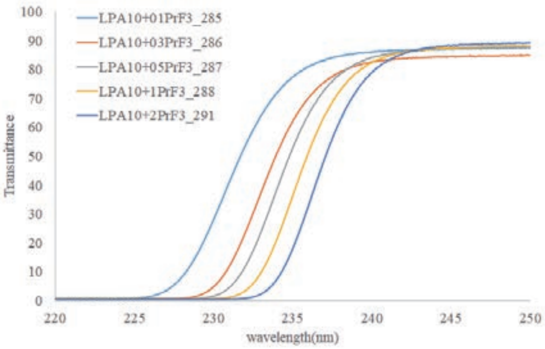

Fig. 1. Transmission spectrum for the LPA.

Although the absorption behavior of the Pr-doped LPA glasses was clearly characterized, luminescence measurements remain inconclusive due to instrumentation limitations. Future experiments will focus on improving measurement conditions and signal screening methods to enable effective evaluation of emission and excitation spectra. Once optimized, these measurements will guide the assessment of scintillator performance and help identify the most suitable material composition for scattered neutron detection.

[1] K. Shinohara *et al.*, the 9th International Symposium on Optical Materials (IS-OM’9), Tarragona (Spain), from June 26 to 30, 2023.
[2] T. Shimizu *et al.*, UVSOR Activity Report **51** (2023) 119.

Optical Properties of Rare-Earth Doped $La(BO_2)_3$ Phosphor for Radiation Detection

J.Y. Cho[1], E.J. Choi[1], D.W. Jeong[1], N.D. Ton[1] and H.J. Kim[1]

[1]Department of Physics, Kyungpook National University, Daegu 41566, Republic of Korea

Borate-based materials are of considerable interest due to their optical transparency, wide bandgap, and thermal and chemical stability, making them ideal hosts for rare-earth dopants in luminescent applications. In particular, lanthanum borates such as $La(BO_2)_3$ offer a stable crystal environment that supports efficient energy transfer and emission. When doped with rare-earth ions like Nd^{3+}, Eu^{3+}, and Pr^{3+}, these materials exhibit promising luminescence properties suitable for lasers, phototherapy, and radiation detection [1–3].

However, studies on $La(BO_2)_3$ phosphors doped with Ce^{3+} and Tb^{3+} remain limited. This work focuses on investigating the luminescence behavior of Ce, Tb co-doped $La(BO_2)_3$ using PL, PLE, and VUV excitation (BL7B beamline), aiming to elucidate their emission mechanisms and assess their potential for optical applications.

In addition, since $La(BO_2)_3$ can be fabricated both as glass and as a crystalline phosphor, we aim to investigate the differences in their luminescence properties through VUV spectroscopy.

The samples were prepared via solid-state reaction at 900 °C for 10 hours from La_2O_3 and H_3BO_3 powder as starting materials and $CeBr_3/Tb_4O_7$ activator. After the mixing process,the mixtures were loaded in alumina crucibles and placed in a high-temperature round furnace where the solid-state reactions occurred. Finally, the products were ground in an agate mortar then introduced to XRD measurement to confirm the crystallization structures before pelletized with a hydraulic press.

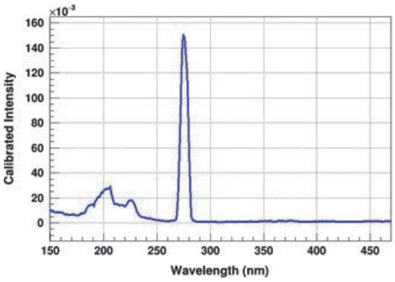

Fig. 1. Calibrated excitation spectrum of $La(BO_2)_3$:Tb phosphor.

Under the excitation measurement of 545 nm emission on $La(BO_2)_3$:Tb phosphor, broad bands from 180-240 and an intense peak of 270-285 nm were observed as shown in Fig.1. The broad band at 180-240 nm could be explained by the transitions from low energy levels to 4f levels of Tb^{3+} while the prominent peak appears at 270–280 nm, indicating the most efficient excitation wavelength for terbium (Tb^{3+}) emissions at 545 nm is characteristic of 4f → 5d transitions for Tb^{3+}. The PL excitation spectrum of $La(BO_2)_3$:Tb confirms that the material can be efficiently excited at 270–285 nm to produce the 545 nm emission then making it the potential choice for applications like phosphors in lighting or display technologies where Tb^{3+}'s green emission is desired.

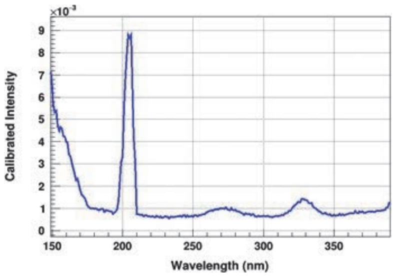

Fig. 2. Calibrated excitation spectrum of $La(BO_2)_3$:Ce phosphor.

Meanwhile, the excitation spectrum of $La(BO_2)_3$: Ce corresponding to 400 nm emission as shown in Fig. 2 is primarily dominated by a strong transition near 200 nm, making it effective for deep-UV-excited blue emission applications. Besides, weak bands from 260 - 290 nm and 320-350 nm were observed. The weak response at higher wavelengths limits its efficiency under near-UV excitation sources but could still contribute to broad-spectrum phosphor applications.

[1] X. Wang *et al.*, Mater. Res. Bull. **52** (2014) 112.
[2] J. Guohua *et al.*, Crystal Opt. Commun. **242** (2004) 79.
[3] T. Dogan *et al.*, Ceram. Int. **45** (2019) 4918.

UVSOR User 9

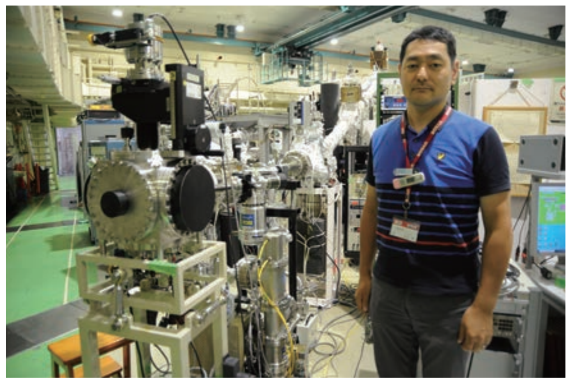

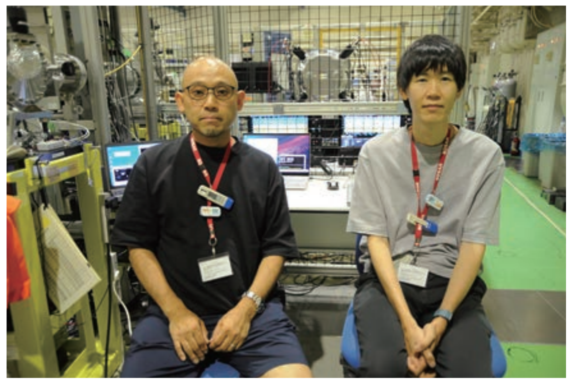

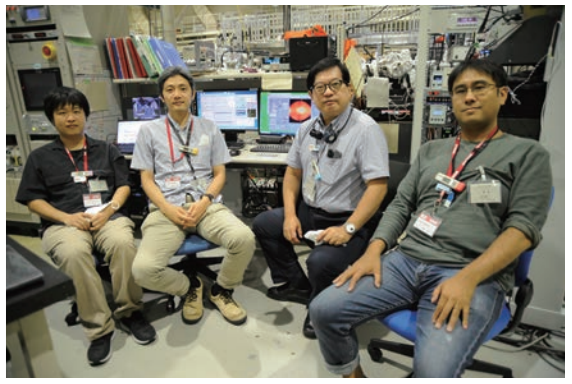

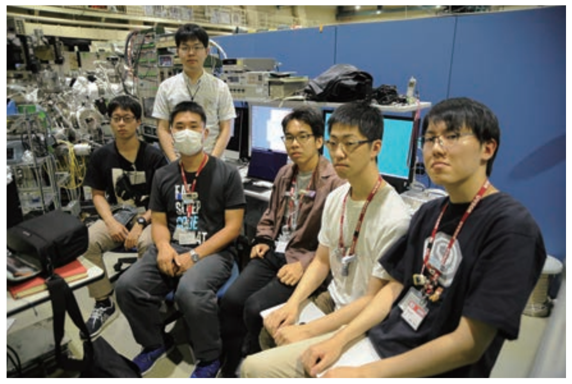

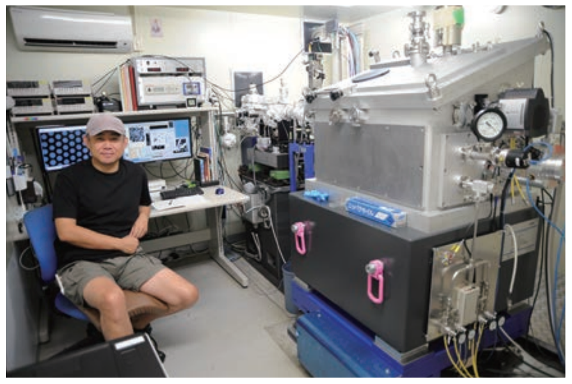

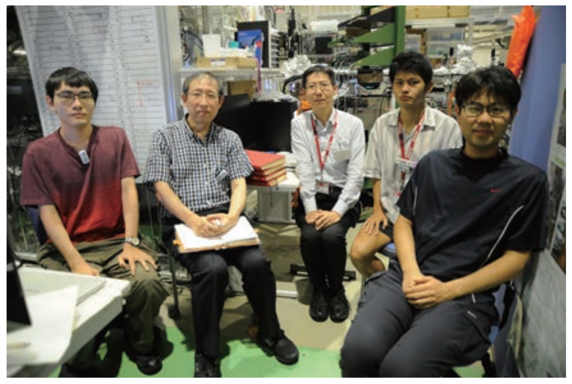

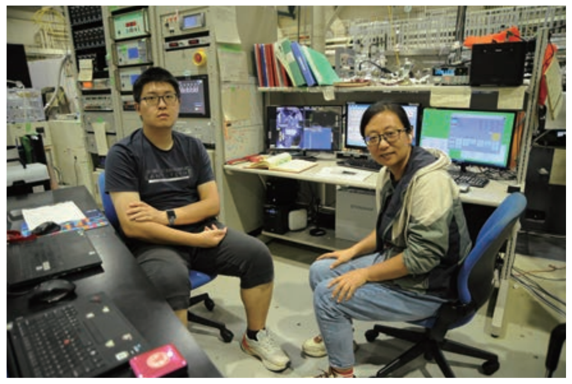

UVSOR User 10